Université de Poitiers

École doctorale Sciences et Ingénierie des Systèmes, Mathématiques, Informatique
Secteur disciplinaire Traitement du Signal et des Images

Thèse de doctorat

Graph-based registration for biomedical images

Présentée par :
Hong Nhung PHAM
XLIM, UMR CNRS n°7252

Sous la direction de :
Philippe CARRÉ, David HELBERT et Pascal BOURDON

Devant le jury composé de :

Directeur de thèse:
Philippe CARRÉ, Professeur, Université de Poitiers
Co-directeurs de thèse:
David HELBERT, Maître de Conférences, Université de Poitiers
Pascal BOURDON, Maître de Conférences, Université de Poitiers
Rapporteurs:
Jean-Christophe BURIE, Professeur, Université de La Rochelle
Jean-Pierre DA COSTA, Maître de Conférences, HDR, Bordeaux Sciences Agro
Examinateurs:
Ludovic MACAIRE, Professeur, Université de Lille 1
Sylvie TREUILLET, Maître de Conférences, Polytech'Orléans
Frédéric LOURADOUR, Professeur, Université de Limoges

11 février 2019

Acknowledgment

This research was carried out at ASALI department of XLIM Laboratory, France. During the time of my research, I was given marvelous support and assistance by those who contributed to this research.

First of all, I would like to express my profound gratitude to my supervisor Prof. Philippe Carré, my co-supervisors David Helbert and Pascal Bourdon for giving me the opportunity to do PhD at XLIM laboratory. I was provided much guidance by them throughout my time of research. I am thankful for all of their ideas, encouragements and supports. I appreciate that they guided me in the right research direction, but still prioritized my ideas and allowed this research to be my own work. My sincere acknowledgment is given to my thesis supervisor Prof. Philippe Carré for his motivation and immense knowledge. His ideas were always the helpful in solving many problems that I encountered during my research and helped my writing to be well organized. I give special thanks to David Helbert for always keeping me motivated and inspiring me during the most difficult times of my research. He always believed in me and looked at the bright side of things. Whenever the going was tough and I got stuck, I sought him for help, and his optimism relieved my stress. He was always patient to give me suggestions as well as to fix all of my mistakes. I would also like to give appreciation to Pascal Bourdon for his advice and counseling. He was always able to point out different aspects of each problem as well. That helped me have new ideas to solve the problem.

Special thanks to the reviewers Prof. Jean-Christophe BURIE and Jean-Pierre DA COSTA for reviewing my thesis and providing interesting feedbacks and insightful comments. The feedback helped me better prepare for the defense and improve the manuscript as well. I am also grateful to all of the jury members for giving me different questions and ideas which made me look at my research from different perspectives. I am thankful to those who attended my thesis defense and those who contributed to the celebration. You all made my day a memorable one.

Special thanks to my colleagues at the lab for the stimulating discussions and contributing in one way or another to my PhD research. I am thankful to the

Photonique team of the XLIM laboratory for providing the biomedical images and supporting me in understanding the operating principle of the device.

Finally, I must especially express my gratitude to my parents for their consistent supports and always being there for me at all times. Thanks to all my family members, friends and loved ones for their moral support.

Hong Nhung PHAM
Chasseneuil du Poitou
February 2019

Abstract

Multiphoton microscopy has become a powerful tool in biomedical research to visualize the information of cell and tissue biology. The reasons why it has gained popularity are the ability to obtain high resolution optical sectioning, high contrast, and minimal phototoxicity within thick samples. This technology can be applied to applications on living organisms using optical fibers, thus, limits surgical biopsies. The working principle of the fiber scanner in the microendoscope device imposes an outgoing spiral scanning from the center to the periphery of the region to be captured, giving raw data on irregular grids. The term "irregular grid" refers to the spatial coordinate system of the images. Classically, images are processed on integer pixel coordinates, so called "regular grid". In contrast, the images obtained by a spiral scanning have floating coordinates and different point distributions between the center region and the border. Ultimately, the microendoscope using optical fiber should allow *in vivo* applications for assessment of dangers (such as cancers). However, such kind of images produced by microendoscope introduces several limitations and challenges: narrow field of view, noise, distortions due to movement of the organisms and the device itself, irregularly sampled data by the spiral acquisition.

This research moves beyond the weaknesses and challenges of the imaging device by introducing novel approaches to image registration and mosaics. In particular, this thesis is formulated under the goal to enhance the field of view of the specialists. This targeted application is considered as a procedure that consists of several steps. It includes providing an appropriate image registration technique that accounts noise, distortions and the irregular sampling before constructing the mosaics.

Firstly, a novel Spectral Graph Wavelet based nonrigid registration approach is proposed to register images on regular grid. The optimization is under the well known Log-Demons framework. The success of this method is proven by its improvements compared to the existing methods that use the similar framework on noisy and non-noisy images on regular grid. This is a stepping stone towards building a registration method of images on irregular grids.

Secondly, motivated by the previous step, an innovative image registration method

of images on irregular grids is introduced. Here, the floating coordinates of the points and the difference in point distributions at different regions of the images can be easily taken into account thanks to the Spectral Graph Wavelet decomposition and the Log-Demons framework. Both of these existing researches are fast and simple to implement on different types of data.

Lastly, we construct the mosaics from the image sequence on irregular grids. The registration of images on irregular grids is used to compensate for the motion distortions as well as the local deformation within the images.

Keywords: Confocal microscopy, microendoscope, image registration, image stitching, image mosaics, nonrigid image registration, Spectral Graph Wavelets, Demons, Log-Demons.

Résumé

La microscopie multiphotonique est devenue un outil puissant dans la recherche biomédicale pour visualiser les informations de la biologie cellulaire et tissulaire. Les raisons pour lesquelles il a gagné en popularité sont la capacité à obtenir un sectionnement optique à haute résolution, un contraste élevé et une phototoxicité minimale dans des échantillons épais. Cette technologie peut être appliquée à des applications sur des organismes vivants utilisant des fibres optiques. Le principe de fonctionnement du scanner à fibres optiques dans le microendoscope impose un balayage en spirale sortant du centre vers la périphérie de la région à capturer, fournissant des données brutes sur des réseaux irréguliers. Le terme "grille irréguliére" fait référence au système de coordonnées spatiales des images. Classiquement, les images sont traitées en coordonnées entières de pixels, appelées "grille régulière". En revanche, les images obtenues par balayage en spirale ont des coordonnées flottantes et des distributions de points différentes entre la région centrale et la bordure. En fin de compte, le microendoscope utilisant la fibre optique devrait permettre des applications in vivo pour évaluer les dangers (tels que les cancers). Cependant, ce type d'images produites par le microendoscope présente plusieurs limitations et défis: champ de vision étroit, bruit, distorsions dues au mouvement des organismes et du dispositif lui-même, données échantillonnées de manière irrégulière par acquisition en spirale.

Cette recherche va au-delà des faiblesses et des défis du dispositif d'imagerie en introduisant de nouvelles approches d'enregistrement des images et de mosaïques. En particulier, cette thèse est formulée dans le but d'améliorer le champ de vision des spécialistes. Cette application ciblée est considérée comme une procédure comportant plusieurs étapes. Cela inclut la fourniture d'une technique appropriée d'enregistrement d'image prenant en compte le bruit, les distorsions et l'échantillonnage irrégulier avant la construction des mosaïques.

Premièrement, une nouvelle approche d'enregistrement non rigide basée sur Spectral Graph Wavelet est proposée pour enregistrer des images sur une grille régulière. L'optimisation se fait dans le cadre bien connu de Log-Demons. Le succès de cette

méthode est prouvé par ses améliorations par rapport aux méthodes existantes qui utilisent le même cadre pour les images bruitées et non bruitées sur une grille régulière. Il s'agit d'un tremplin vers la construction d'une méthode d'enregistrement des images sur des grilles irrégulières.

Deuxièmement, motivé par l'étape précédente, une méthode innovante d'enregistrement d'images sur des grilles irrégulières est introduite. Ici, les coordonnées flottantes des points et la différence de distribution des points au niveau des différentes régions des images peuvent être facilement prises en compte grâce à la décomposition Spectral Graph Wavelet et au cadre Log-Demons. Ces deux recherches existantes sont rapides et simples à mettre en œuvre sur différents types de données.

Enfin, nous construisons les mosaïques à partir de la séquence d'images sur des grilles irrégulières. L'enregistrement des images sur des grilles irrégulières est utilisé pour compenser les déformations de mouvement ainsi que la déformation locale au sein des images.

Mots-clés: Microscopie confocale, microendoscope, enregistrement d'image, couture d'image, mosaïques d'images, enregistrement d'image non rigide, Spectral Graph Wavelets, Demons, Log-Demons.

Contents

1 Introduction **1**
- 1.1 Scientific objectives . . . 2
- 1.2 Thesis Organization . . . 4

2 Image Acquisition **5**
- 2.1 Two photon microendoscope . . . 5
  - 2.1.1 Double-clad air-silica microstructured endoscopic fiber . . . 6
  - 2.1.2 Scanning trajectory . . . 9
- 2.2 The microendoscopic images . . . 12
- 2.3 Conclusion . . . 15

3 Overview of Image Registration Concepts **17**
- 3.1 Image Registration . . . 18
  - 3.1.1 Non-rigid Image Registration . . . 19
  - 3.1.2 Demons Framework and the Variants . . . 27
- 3.2 Summary and Discussion . . . 30

4 Graph-based Image Registration on a Regular Grid **33**
- 4.1 Introduction . . . 34
- 4.2 Graph Theory . . . 35
  - 4.2.1 Review on Graph Theory . . . 35
  - 4.2.2 Graph definition . . . 37
  - 4.2.3 Spectral Graph Theory . . . 40
- 4.3 From Demons Framework to Spectral Demons . . . 45
  - 4.3.1 Demons Framework . . . 45
  - 4.3.2 Spectral Demons . . . 49
  - 4.3.3 Application of the process to microscopic images . . . 53
- 4.4 Spectral Bspline . . . 57
  - 4.4.1 Bspline Registration . . . 57

4.4.2 Spectral Bspline Image Registration 61
4.4.3 Results 62
4.5 Spectral Graph Wavelet (SGW) based Image Registration 66
4.5.1 Objective function 67
4.5.2 Results 69
4.6 Conclusion 77

5 Image Registration and Mosaicing of Images on Irregular Grids 79
5.1 Introduction 79
5.2 Problem Formulation 80
5.3 Graph construction for image on irregular grid 84
5.4 Registration for Images on Irregular Grids 87
5.4.1 Experimental Results 90
5.5 Mosaics of images on irregular grids 94
5.5.1 The workflow of mosaics construction 95
5.5.2 Results 97
5.6 Conclusions 103

6 Conclusion and Perspectives 105
6.1 Future works 107

List of Tables

4.1 Mean Square Error (MSE) between the fixed image and restored image of Bspline and Spectral Bspline methods. 63
4.2 MSE between the restored image and the fixed image 70

List of Figures

2.1 TPME system 7
2.2 Custom-design air-silica DC-PCF 8
2.3 Different scanning trajectories 8
2.4 System axes 9
2.5 Scanning performed by the optical fiber during excitation on a single axis (a) in using a real axis. (b) using a virtual axis. 10
2.6 Circular scan 11
2.7 Spiral image acquisition 12
2.8 Label-free microendoscopy images 13
2.9 Label-free in vivo experiment 14
2.10 Biological images taken by microendoscope 15

3.1 Image registration 18
3.2 Image registration classification 20

4.1 Graph representation of digital image 38
4.2 Graph representation of signal 41
4.3 Feature matching 50
4.4 Spectral Demons method on Microscopic images 55
4.5 Spectral Demons method on microendoscopic images 56
4.6 Comparison between Bspline registration and Spectral Bspline registration of microscopic images 65
4.7 Spectral Graph Wavelet coefficients 66
4.8 Lena image with a random deformed image used in this experiment . 70
4.9 Mean Square Error (MSE) with respect to Gaussian noise, registration of Lena image 72
4.10 Registration of Lena images with random deformations and increasing Gaussian noise added. 73

4.11 Pairs of T1 brain images and endomicroscopic images are used in this experiment 75
4.12 Comparison between our proposal and the existing methods on T1 brain images and endomicroscopic images when no noise is added . . 76
4.13 MSE of Log-Demons, Spectral Log-Demons methods, and our method with respect to Gaussian noise (standard deviation σ_{noise}) 77

5.1 Panorama construction from a sequence of frames on irregular grids without nonrigid deformation correction. 82
5.2 Two images cropped from an overlapping region of two frames, and the representation of points on spiral acquisition of 20 turns, 80 points/-turn (the red points belong to the first image and the blue points belong to the second image 83
5.3 Graph topology of images cropped at different regions of a frame with spiral acquisition of 20 turns, 80 points/turn 86
5.4 Spectral Graph Wavelet Transform of image on irregular grid 87
5.5 Spectral Graph Wavelets decomposition of a microendoscopic image on an irregular grid , at 4 scales with respectively 1, 2, 4, 8, 16 of graph connectivities from the top to the bottom. 88
5.6 Comparison between the registered images of our method and the existing methods for two pairs of images($\alpha_g = 2, \alpha_s = 1, \alpha_i = 6$ for registration on irregular grid) 91
5.7 SNR with respect to the number of iterations 92
5.8 Registration with $\alpha_g = 10, \alpha_s = 5, \alpha_i = 20$ 92
5.9 Registration result of the first pair of microendoscopic images on irregular grids 93
5.10 MSE values after registrations of the first pair of microendoscopic images with respect to the values of graph connectivity with two sets of weighting parameters ($\alpha_g = 1, \alpha_s = 5, \alpha_i = 20$ and $\alpha_g = 1, \alpha_s = 1, \alpha_i = 4$) 94
5.11 The pipeline to construct mosaic. 96
5.12 Two pair of random frames from the image sequence (First row: 9 frame difference, Second row: two consecutive frames) 98
5.13 Panorama created from two frames from the image sequence (9 frame difference). (Red channel: First image, Green channel: Second image) 99
5.14 Panorama created from two frames from the image sequence (consecutive frames). (Red channel: First image, Green channel: Second image) 100

5.15 Panorama created from three frames from the image sequence. 101
5.16 Panorama constructed from a sequence of 12 frames 102

List of Abbreviations

2PEF Two Photon Excited Fluorescence.

AC Auto Correlation.

BFGS Broyden-Fletcher-Goldfarb-Shanno.

CM Cut Mirror.

CT Computed Tomography.

DC-PCF Double-clad air-silica microstructured endoscopic fiber.

DM Dichroic Mirror.

FFD Free Form Deformation.

fps frame per second.

HDR High Dynamic Range.

IR Energetic Infrared.

LBFGS Limited-memory Broyden-Fletcher-Goldfarb-Shanno.

MI Mutual Information.

MO Micro-optics.

MRI Magnetic Resonance Imaging.

MSE Mean Square Error.

NA Numerical Aperture.

OD Outer Diameter.

PET Positron Emission Tomography.

PZT Piezoelectric Tube.

SEM Scanning Electron Microscopy.

SGW Spectral Graph Wavelet.

SHG Second Harmonic Generation.

SSD Sum of Square Difference.

TPME Two Photon Microendoscope.

TPS Thin-Plate Spline.

Chapter 1

Introduction

Contents

1.1 Scientific objectives 2

1.2 Thesis Organization 4

The context of this thesis is under the development of the multiphoton microendoscope which is developed by the Photonics department at XLIM laboratory. The images taken by the novel acquisition system have a narrow field of view. The main aim of this thesis is to construct a mosaic from the image sequence to have a full view panorama.

The development of medical imaging has revolutionized the way physicians, biologists, scientists and patients observe organisms to assess health and diseases. The medical equipments allow users to view inside living objects with or without cutting them open. While some machines such as X-ray machines, MRI machines, CT and PET scanners provide macroscopic views of body parts and organs, the microscope technology is designed to magnify the image of cells and objects that are too small to view with naked eyes. Thus, the microscope technology is one of the most innovative inventions and has always been an essential tool for assessment of cell and tissue biology. However, a traditional microscope requires a surgical biopsy, meaning samples of tissues must be taken out from the patient to be examined. This process, however, is costly, takes a long time and is sometimes impossible to take samples from all the suspect parts.

The multiphoton microscope used in conjunction with optical fibers can obtain histological examination of living tissues in real time. Such a multiphoton microscope can be referred to as multiphoton microendoscope. This technology overcomes the limitations of classical microscopes in the way it removes or limits surgical biopsies.

In additions, it carries out the advantages of the multiphoton microscope technology that could produce high resolution optical sectioning, high contrast and least phototoxicity within a thick sample. The optical fiber of the microendoscope scans over time on living objects. Each scan has a spiral path starting from the center to the periphery of the region to be captured, covering a disc-shape. Consequently, the important information, usually located at the center of the region, is emphasized. Despite all the advantages of the multiphoton microendoscopic, processing of the images acquired by this machine suffers from several aspects. The spiral sampling takes place temporally along the spiral path. This process produces a list of points on an irregular grid. The measurements are more at the center than at the borders of the image. The absences of some pixels and information redundancies disrupt the reconstruction of the image. Such images reveal features which introduce additional complexities to process. In addition, the movements of the probe and of the living tissue often cause motion distortions and local displacements.

Furthermore, although the multiphoton microendoscope can provide high resolution images, it can not capture a full region of a large area at once. The clinician needs to move the probe around the region to capture several images. It is difficult for physicians to look at several images with a narrow field of view and give an accurate assessment. Thus, it is important to construct an accurate panorama from the image sequence in order to enhance the field of view. This will in turn help physician have a good interpretation of the images, especially when it may relate to human lives.

This thesis is set out towards the goal of providing an accurate wide field of view in optical biopsy to the clinicians. There are several important building blocks in the pipeline to construct a mosaic. Also, it is indisputable that an appropriate nonrigid registration is necessary to compensate for the soft deformations and distortions of the images in the sequence. This is not only true for microendoscopic images but also for other kinds of medical images.

1.1 Scientific objectives

As mentioned earlier, the aim of this thesis is to construct a mosaic from the microendoscopic image sequence. This also consists of finding a supportive non-rigid image registration technique that accounts for noise, local deformations and is adapted with the data on irregular grids. Before providing an appropriate approach, these questions should be answered:

- The first question is how to find a framework that is adaptable with irregu-

larly sampled data, while to the best of our knowledge, most of the existing applications process the images on a regular grid?

- The second question is how to account for the noise and distortions that are unavoidable during the capture?

For such kind of irregularly sampled data, it is important to find an appropriate data representation that helps the mathematical study of the data. In recent years, the signal processing on graphs has been exposed to different types of data, and has been broadened to the computer vision field. The advantage of graph representation is that it is simple and flexible to represent data regardless of the data structure. Recently, the graph spectrum was successfully used in spectral matching and image registration that motivates our research on graph signal processing. This partially answers to the first question that the data are represented by graphs and our registration problem is cast into the graph matching problem.

However, the graph representation is normally computationally expensive and time consuming. This pops up an additional question, which is to find a suitable registration framework that can be adapted to the expensive computation of graphs. A survey of the literature reveals a numerous number of innovative image registration techniques. The Demons approach is one of the most powerful nonrigid registration frameworks. It was found to be computationally efficient and easy to implement. These desirable features of the Demons approach have motivated an extensive number of research to extend from the classical one. The research of Lombaert *et al* [70], that uses graph spectrum under the Log-Demons framework to successfully register images with large and complex deformations, has gained much attention in the literature. But it was proven to be sensitive to noise [70].

The first contribution of this thesis is inspired by the success of the Spectral Log-Demons method. The role of graph spectrum was replaced by the Spectral Graph Wavelets while keeping the use of the Log-Demons framework. The Spectral Graph Wavelets decomposition was recently provided by Hammond *et al* [48]. It is defined through the graph spectral domains, thus, carries out the advantages of the graph spectrum and represents the data at different scales. Our contribution outperforms the existing methods under the Log-Demons framework when noise exists. This answers to our second question of finding a technique that is adaptable to noise.

The second contribution of this thesis is motivated by the previous contribution. The Log-Demons framework is cast to match points of images on irregular grids. While the same framework fails to register the microendoscopic images on regular grid, the method on irregular grids successfully registers the raw data without any projection on a regular grid. Consequently, the mosaic construction with a motion

compensation by the image registration on irregular grids can remove a part of the shearing and misalignments appealing on the mosaic.

In conclusion, this thesis proposes a Spectral Graph Wavelet based image registration method that can be adapted to noisy images. While existing registration methods either use the classical wavelets or the spectral constraint, our registration method uses the Spectral Graph Wavelets decomposition. This method not only provides an efficient tool to find correspondence between images but also gives new perspectives in using the Graph Wavelets for registration. In addition, our registration method of images on irregular grids gives a new point of view of the way we treat the input images in the continuous domain of the raw data instead of the discrete domain. Ultimately, the mosaic construction from the raw data on irregular grids captured by microendoscope with nonlinear deformation correction can provide an accurate full view of the object to the experts to help their assessment of health.

1.2 Thesis Organization

The remainder of this manuscript is organized as follows:

- Chapter 2 introduces the image acquisition process as well as describes the multiphoton microendoscope used to capture images. We here also describe the scanning trajectory of the probe and later point out the properties of the images taken by multiphoton microendoscope.

- Chapter 3 provides an exhaustive review of existing non-rigid image registration methods. The analysis of the state-of-the-art of nonrigid image registration and how it is classified is covered in this chapter.

- Chapter 4 gives an introduction to our methods on a regular grid. It begins with a review of the spectral graph theory and later describes the registration methods using graph spectrum under the Bspline framework and the Log-Demons framework. We then introduce our contribution using Spectral Graph Wavelets under the Log-Demons framework in the last section of this chapter.

- The registration on irregular grids is depicted in Chapter 5. We finally construct the mosaic from the image sequence on irregular grids with the motion compensation by the registration on irregular grids.

- Chapter 6 highlights the global conclusion on all the presented results and gives future research directions.

Chapter 2

Image Acquisition

Contents

2.1 Two photon microendoscope 5

2.1.1 Double-clad air-silica microstructured endoscopic fiber . . 6

2.1.2 Scanning trajectory 9

2.2 The microendoscopic images 12

2.3 Conclusion 15

This chapter provides a description of the image acquisition process. Subsection 2.1 describes the multiphoton microendoscope used for capturing images. It provides the different scanning trajectory and highlights the advantages of the scanning trajectory considered in this work. The working principle of the fiber-scanner is presented briefly. Next, a description of how the camera produces different scanning path is given. Finally, the subsection 2.1.2 introduces how a spiral scanning trajectory is obtained. The subsection 2.2 illustrates comprehensive properties of the biomedical images used in this research work. For a more extensive understanding of the acquisition system, we refer the interested readers to the research of Ducourthial *et al* [31, 30]. The following sections are constructed and partially translated from [31, 30].

2.1 Two photon microendoscope

Multiphoton microscopy has gained popularity in different fields of biological research such as embryology and neurobiology. This is because it has the ability to provide

high-resolution optical sectioning within thick tissue samples, high constrast, with low level of phototoxicity. It has been reported that multiphoton microscopy enables 3D imaging with significantly high penetration depth. As an example, a penetration depth ranging from 500 and 600 microns at 800nm is reported for given samples [51]. In addition, they have been shown to provide reduced image photobleaching. Photobleaching is the phenomenon of signal loss happening when the fluorophore loses the ability to fluoresce. The numerous advantages of multiphoton microscopy contribute to its attractiveness for use in living organisms, using an optical fiber.

Figure 2.1 describes the structure of a two photon microendoscope (TPME). As shown in Figure 2.1, the TPME system is fed by a standard MIRA 900 Ti:Sapphire oscillator (150fs, 76MHz, 810nm, 10nm, 2W). In order to control polarization, three different half-wave plates are used where it is necessary in the setup. A micro-optics (MO) is used to focus the beam at the endoscopic fiber output.

2.1.1 Double-clad air-silica microstructured endoscopic fiber

The Double-clad air-silica microstructured endoscopic fiber (DC-PCF) is designed using smaller core size in order to improve special resolution and TPME excitation efficiency [31]. Figure 2.2 shows the cross-section of a custom air-silica DC-PCF. It is made of a small single-mode inner core in order to ensure high spatial resolution while preserving the desired temporal confinement of excitation pulses. The inner core is made of pure silica that delivers energetic infrared (IR) ultrashort pulses. The ultrashort pulses are essential for efficient multiphoton excitation, at the output of a several meters long optical fiber, which is required in a clinical environment. It has a diameter of around $3.5\mu m$, a numerical aperture (NA) of 0.13 at 800nm and free from autofluorescence since it is made of pure silica. Light is guided in the core using a surrounding air-silica microstructured cladding. The cladding is in turn surrounded by a second cladding acting just like a second large area collecting core. The second cladding allows for collecting the visible light that is useful during deep tissues in vivo imaging. Light guidance is multimode and allowed by an air-clad i.e. outer ring of air holes. The multimode second core has a diameter of $188\mu m$. This outer air hole ring has a high air-filling fraction providing a NA of 0.3 at 400nm. It is used to guide all the light collected by the imaging micro-lens located after the endoscopic fiber.

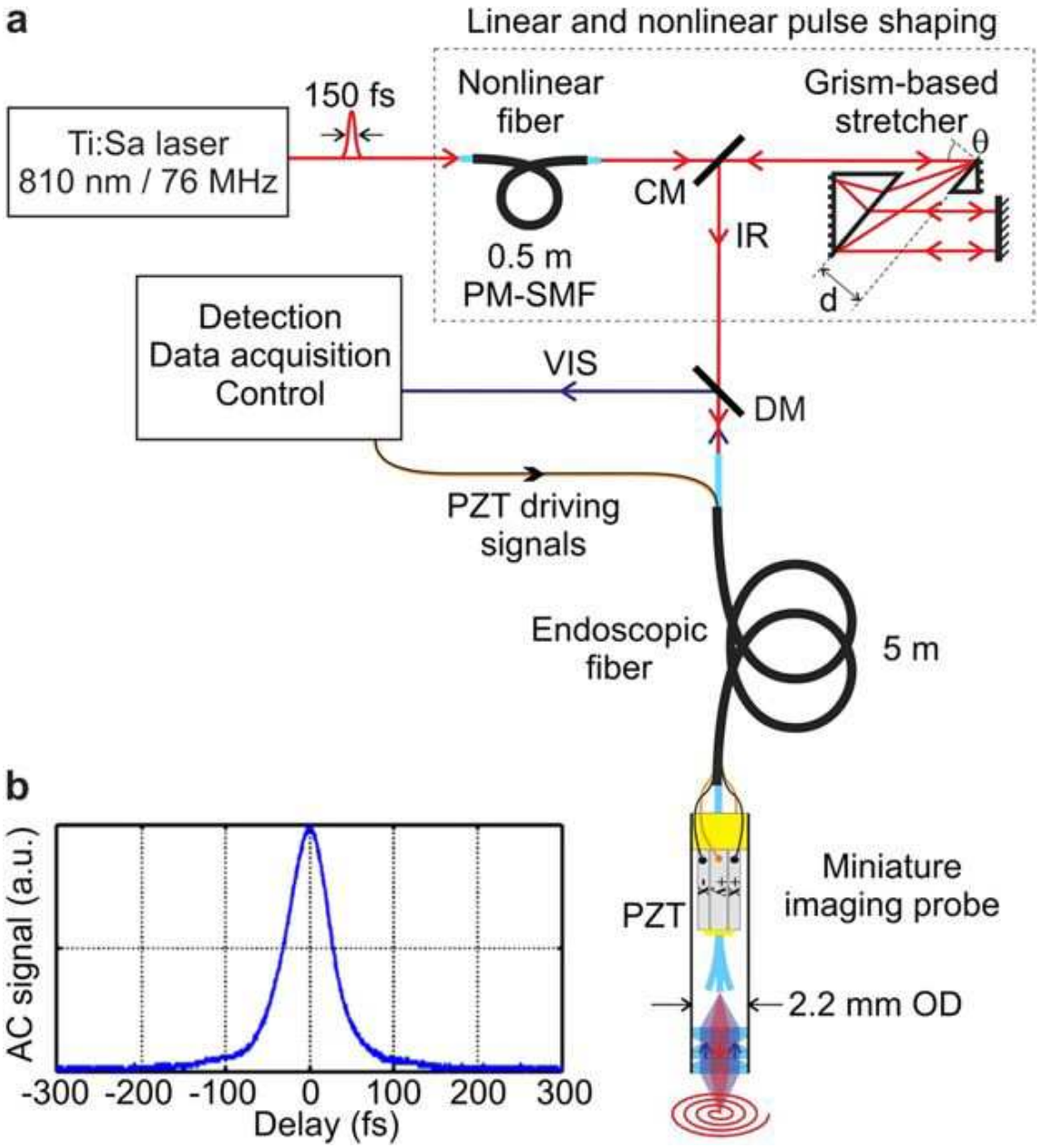

Figure 2.1 – TPME system with linear and nonlinear pulse shaping [31] (a) Scheme of the experimental setup; CM: cut mirror; DM: dichroic mirror; PZT: piezoelectric tube. The miniature fiber-scanning imaging probe is embedded inside a $2.2mm$ outer diameter (OD) stainless steel biocompatible tube. (b) Second order auto correlation (AC) of the IR excitation pulse at the exit of the $5m$ long endoscopic fiber for a delivered power of $20mW$. The corresponding pulse duration is 39fs (FWHM), assuming a deconvolution factor of 1.54.

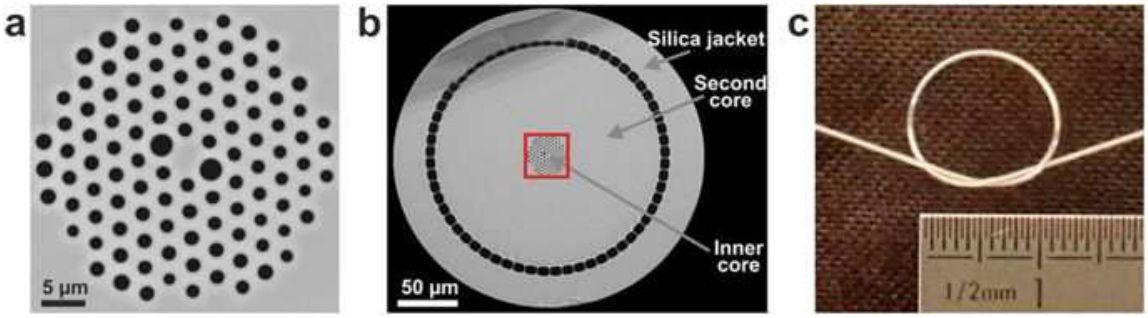

Figure 2.2 – Custom-design air-silica DC-PCF used as the endoscopic fiber within the TPME [31] (a) Close view of the inner core of the fiber through scanning electron microscopy (SEM). Pure silica is in grey and air in black. (b) SEM image of the fiber cross-section without its outer polymer mechanical cladding. The silica jacket and the second core diameters are respectively equal to $266\mu m$ and $188\mu m$. The red square denotes the inner core and its microstructured cladding which are depicted in (a). (c) DC-PCF flexibility.

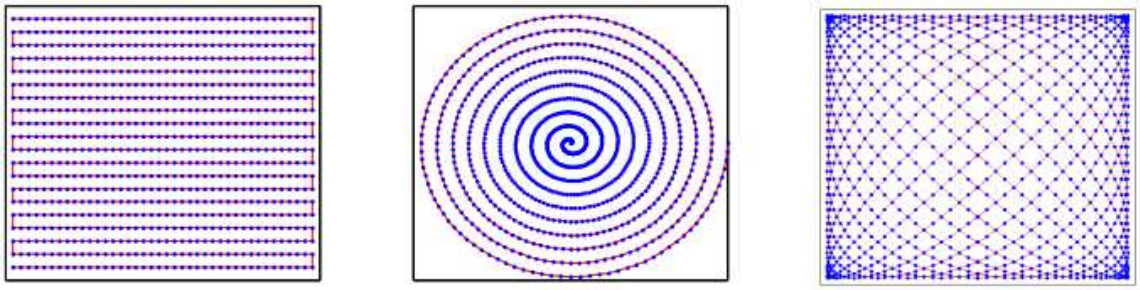

Figure 2.3 – Different scanning trajectories

2.1.2 Scanning trajectory

There exist several possibilities of scanning trajectory by the laser spot. Figure 2.3 (left) shows a classical scanning method, where the scanning path involves rows and columns. This allows for a homogeneous sampling of the field, but requires a massive difference between the frequencies of the two axes of movement, with a significantly high frequency ratio (about frequency values of hundreds). Another sampling method, shown in Figure 2.3 (middle), follows a spiral path. This scanning method produces a dense sampling of the center field. This scanning is useful in cases where in-depth observation of thick sample in the center field of view and end at the edges such as an embryo are required. Another possibility, shown in Figure 2.3 (right), is to use a Lissajous scan by sending two sinusoidal signals of different frequencies on the two mirrors. A major disadvantage of this approach is that it leads to under-sampling at the center of the field and over-sample at the image periphery.

Spiral scanning method is chosen because it is the most adequate and suitable solution for cases where the most important information is usually located at the center of the observed field. This helps to avoid under-sampling of vital information in the observed field. Next, the working principle of the fiber-scanner is presented briefly. A piezoelectric ceramic tube (PZT) revolves around the fiber, allowing for imposing the trajectory of the last few millimetres of the fiber forming a resonating cantilever. Thus, creating an outgoing spiral scanning pattern in two dimensions. After optimization, it is possible to work with a large field of view without image distortion at a rate of 8 frames per second (fps).

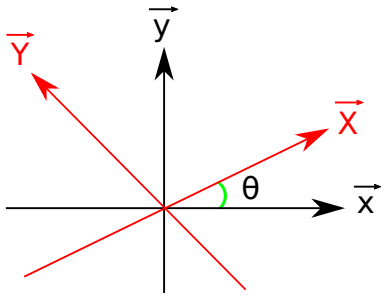

Figure 2.4 – System axes. $\overrightarrow{x}$, $\overrightarrow{y}$: axes defined by the actual electrodes; $\overrightarrow{X}$ and $\overrightarrow{Y}$: defined axes by the virtual electrodes corresponding to the resonator's own axes.

The optical fiber micro-scanner is excited on its own mechanical axes using virtual electrodes (V_x, V_y). The virtual electrodes themselves correspond to a linear combination of two actual electrodes in the system. Figure 2.4 shows the virtual electrodes

(X, Y) which correspond to a linear combination of the two actual electrodes (x, y) defined by the equations 2.1 and 2.2.

$$\overrightarrow{X} = \cos(\theta)\overrightarrow{x} + \sin(\theta)\overrightarrow{y} \tag{2.1}$$

$$\overrightarrow{Y} = -\sin(\theta)\overrightarrow{x} + \cos(\theta)\overrightarrow{y} \tag{2.2}$$

Here, (V_x, V_y) and (V_X, V_Y) represents voltages applied on the real and virtual electrodes respectively. In Figure 2.4, the value of angle θ is determined by applying a sinusoidal voltage solely on the axis $\overrightarrow{X}$ such as:

$$V_X(t) = \cos(\omega t) \tag{2.3}$$

$$V_Y(t) = 0 \tag{2.4}$$

This is achieved when real voltages are applied:

$$\text{On} \quad x \quad : V_x(t) = \cos(\omega t)\cos(\theta) \tag{2.5}$$

$$\text{On} \quad y \quad : V_y(t) = \cos(\omega t)\sin(\theta) \tag{2.6}$$

The value of θ is varied while the shape of the trajectory obtained by the camera is observed. If θ is zero, an elliptical trajectory is produced, serving as the starting point from which a rectilinear trajectory can be produced. Figure 2.5 shows the path of the fiber before and after optimization of the value of θ ($\theta = 0.5585$ rad $= 32$ degree). As displayed in Figure 2.5 (b), the angle between axis $\overrightarrow{x}$ and $\overrightarrow{X}$ is 31.75 degree and corresponds to the value of θ used to synthesize the control signals.

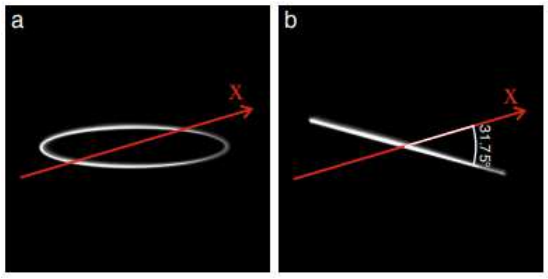

Figure 2.5 – Scanning performed by the optical fiber during excitation on a single axis (a) in using a real axis. (b) using a virtual axis.

Spiral scanning trajectory is obtained by drawing a circular path from the object center with increasing radius. The equations below give the definitions of the voltage applied on the axis for circular scan:

$$V_X(t) = \cos(\omega t) \tag{2.7}$$

$$V_Y(t) = \sin(\omega t + \phi_0) \tag{2.8}$$

Figure 2.6 (a) shows an ellipse oriented according to the axis. The weight of each axis is adjusted using a simple coefficient of amplitude in order to obtain an improved result. This is shown in Figure 2.6 (b).

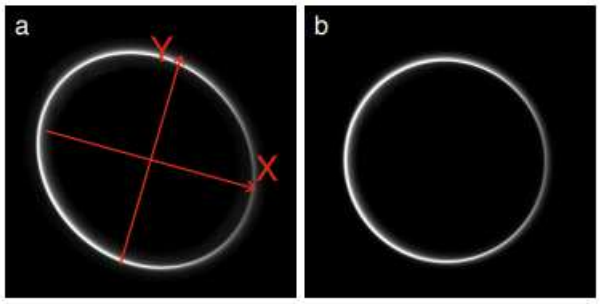

Figure 2.6 – Circular scan (a) before, (b) after adjusting the weights of the two axes.

In brief, the working principle of the fiber-scanner is that a piezoelectric ceramic tube goes around the fiber. By this, the trajectory of the last few millimetres of the fiber forming a resonation cantilever is imposed. Thus creating an outgoing spiral scanning pattern in two dimensions. Once the circular trajectory is obtained in a controlled manner, it is necessary to do amplitude modulation. This is carried out in order to obtain a spiral path starting from the center to the periphery, covering a disc-shaped image field (Figure 2.7). The example is a scan of ten rounds. Considering the horizontal axis, we can see twenty samples along the axis and a twofold number of turns. In a real case, the trajectory scans 125 turns, taking 500 samples each turn, giving 500 x 125 = 62500 pixels in total. The next section describes the characteristics of the biological images taken by microendoscope.

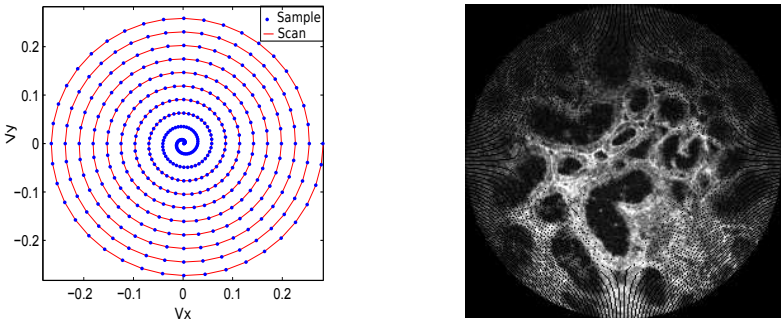

(a) Spiral scanning

(b) Microendoscopic image projected on a regular grid

Figure 2.7 – Spiral image acquisition

2.2 The microendoscopic images

Until now the acquisition system of the microendoscope has been described. It plays an important role in forming the distinct features of the microendoscopic images. In this section, the microendoscopic images and their characteristics in the image processing field are depicted. Figure 2.8 shows the outcomes of the TPME tested *ex vivo* on various unstained biological tissue samples.

Figure 2.8(a) and Figure 2.8(b) show the SHG images of the collagen fiber network of a thick unstained intact and flesh rat tail tendon. In order to prove that TPME provides high sensitivity, the images were obtained without averaging at 8fps and with 5mW of power on the samples. The red arrows indicate the rectilinear polarization impinging the sample. The SHG signal is stronger when the excitation polarization is parallel to the collagen fibers, proving the ability of the TPME to perform nonlinear polarization anisotropy probing. Figure 2.8(c) shows a bimodal image of a label-free section of a mouse ear. The most paramount parts of the ear have been identified on the figure D: dermis; E: epidermis; IC: internal cartilage. Figure 2.8(d) shows a sample of a healthy human lung taken in the alveolar area (i.e. alveolar wall and alveolar entrances). This sample was recorded at a depth of $100\mu m$ below the sample surface. The extracellular matrix elastic fibers appear in red through intrinsic 2PEF while some amount of SHG in green from collagen is detected entangled in the main elastin fiber. The pulmonary alveolar duct and alveolar entrances can be seen in the left part of the figure. Figure 2.8(e) shows a perspective view of a collagen-rich tissue of a mouse aorta, while (f) to (h) shows three perspective views of the extracellular matrix network at 3 different locations

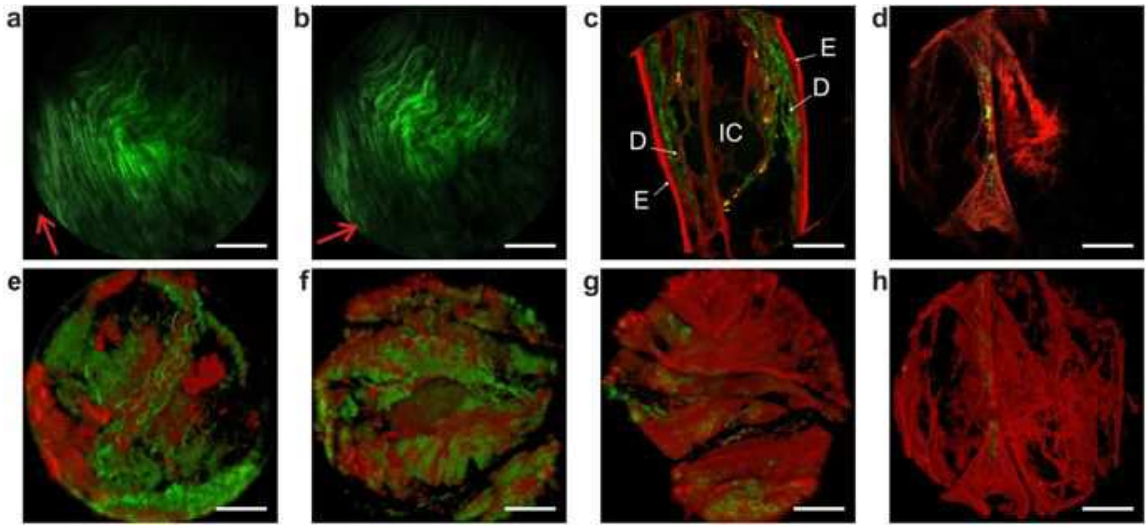

Figure 2.8 – Label-free microendoscopy images of fixed tissue samples ex vivo [31]. Intrinsic 2PEF in red (elastin) and SHG in green (collagen). (a) to (d): raw optical sections. (e) to (h): perspective view from Image 3D software from a set of sixty optical sections each one corresponding to a given depth below the tissue surface, from depth $0\mu m$ to $300\mu m$.

within a healthy human distal lung sample. In vivo experiment, Authors [31] observed the kidney of a living anaesthetized mouse using the TPME. Figure 2.9 shows the label-free captured images in the *in vivo* experiment.

As mentioned earlier, spiral sampling is preferred here because it is the most suitable solution for cases where the most important information is usually located at the center of the observed field. However, such images (produced by spiral scanning) exhibit features which introduce additional complexities in processing. In order to study the features of such images and their related problems, let us consider the images in Figure 2.10. The images are the ones used in this work and they were taken by the microendoscope in grayscale.

The spiral sampling may introduce a number of problems such as:

- *Inaccuracy in comparing two image parts*: since the point density is more at the center and lower at the edge regions, the center of an image corresponds to the edge region of another image. Hence, comparing the two parts may not be accurate.

- *Complexity in spiral image acquisition*: this is mainly due to data complexity and variety (or additional steps) for acquiring the images.

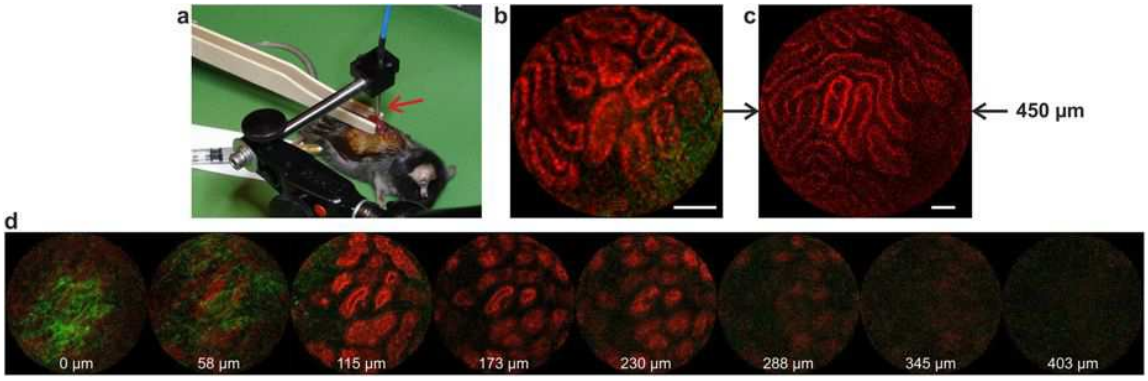

Figure 2.9 – Label-free in vivo experiment [31] (a) Anaesthetized mouse with one kidney being elevated from the body and clamped between two tongue depressors, beneath the 2.2 mm TPME probe (red arrow). A constant power of $30mw$ was launched onto the tissues. (b) SHG (in green) and 2PEF (in red) raw image of respectively the collagen of the capsule and the intracellular flavins of epithelial cells of the kidney tubules. (c) same as in (b) but with a larger FOV of $450\mu m$ (d) successive optical sections of a fibrosis kidney, 6 days after fibrosis induction, taken just after mouse death; the imaging depth below the organ surface is indicated in the bottom in white; in (d), FOVs are $250\mu m$ wide.

- *Difficulty in finding appropriate shape feature approach*: this is due to deformation such as stretching, compression due to heart rate, breathing or distortions that occurs while recording.
- *Difficulty in image texture feature analysis*: this is due to uneven illumination caused by moving or spinning motion of tiny tissues.

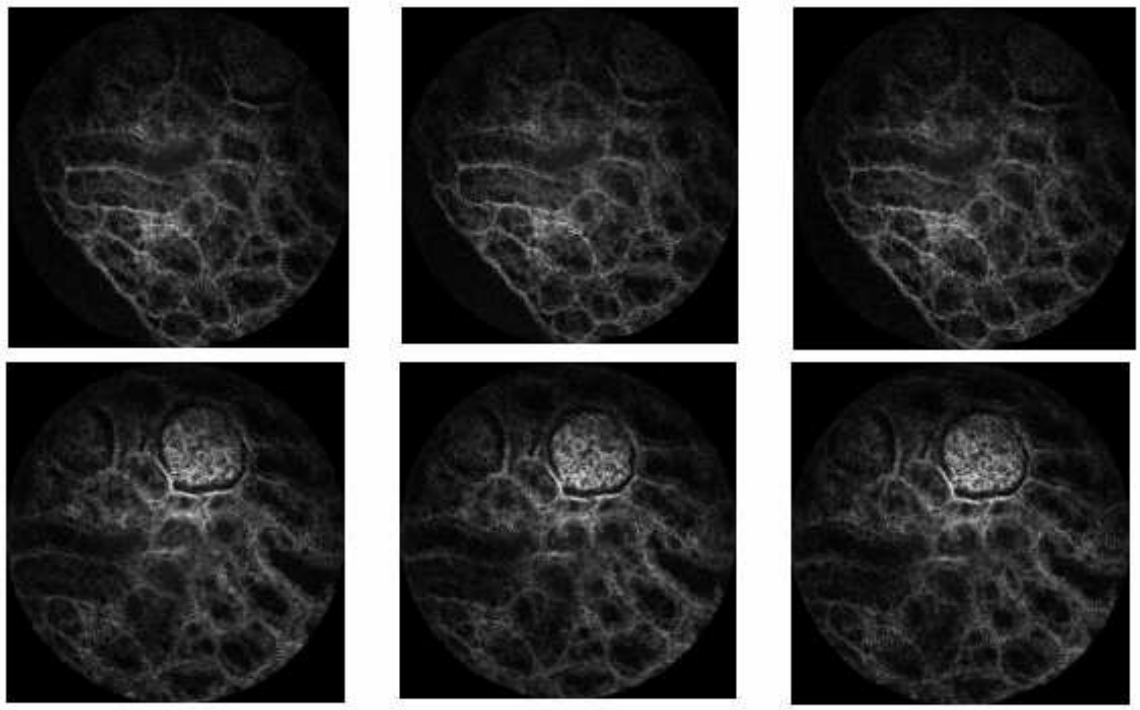

Figure 2.10 – Biological images taken by microendoscope

2.3 Conclusion

In this chapter, the principle of the multiphoton microendoscope with the new technology, as well as the spiral scanning trajectory of the fiber optic were briefly reviewed. Such scanning is preferable when important information is placed at the center of the region to be captured. The images obtained after vivo test on living object have disc-shape. The measurement are more at the center while there are missing points at the regions close to the edges. Therefore, processing on microendoscopic images may introduce several challenges. Firstly, the difference in point distributions of the center and the outer regions of the images makes it difficult to find an appropriate similarity measurement between two images. Secondly, the complexity of the spiral image acquisition makes the processing on this kind of data more complicated. Thirdly, the images taken on soft tissues do not likely have shape features. This is because of the deformations due to the stretching of the tissues, movement and distortions due to heart rate and the effect of the device, making it difficult to find an appropriate shape matching technique. Lastly, the uneven illumi-

nation changes and the complex texture of the images are also challenging problems to overcome.

Although the images taken by microendoscope have great resolution, and important information is captured, the images are still limited to the narrow field of view due to the size of the probe. The images suffer from distortions and noise due to the movement of the sensor, breathing and heart rate of the object. The small field of view makes it difficult for the image readers (such as doctors) to give an accurate assessment of the patients' diseases. A good way to enhance the image field of view is to do image mosaics. To do that, it is important to find a supportive image registration method that can adapt to the properties of the images. Ideally, the method should be able to register the images with a spiral acquisition.

This work proposes to develop image registration and stitching method on regular and irregular grid. In particular, the next chapter provides an overview of different image registration methods. After that, our contribution in image registration for biomedical images on regular grids is described. Motivated by this contribution, an image registration approach on irregular grids to adapt with the spiral acquisition is then proposed. The registration on irregular grids is then used to compensate the local distortion in our last contribution in image mosaics from the images on irregular grids.

Chapter 3

Overview of Image Registration Concepts

Contents

3.1 Image Registration 18

3.1.1 Non-rigid Image Registration 19

3.1.2 Demons Framework and the Variants 27

3.2 Summary and Discussion 30

Nowadays, medical image processing is indispensable in many critical medical equipments such as microscope and endoscope, PET and CT scanners, ultrasound and MRI machines, and X-ray machines. Medical imaging is required to be highly accurate as it is one of the keys related to human life. The applications can help doctors evaluate patients' health, assist surgeries and assess dangers appearing on the sample. The development of these equipments requires the improvements of the image processing part as well. Image registration is a key block in any medical image processing application and is consequently required to meet higher demands. This chapter provides a review of different image registration methods in the literature. Hence, showing the development of image registration in the past decades.

3.1 Image Registration

Image registration is a fundamental block that spatially determines the correspondence between points or regions of two images of the same scene but obtained from different viewpoints and at different times or with different sensors (Figure 3.1). It is considered as a valuable assistant in many applications in computer vision such as atlas construction, image recognition and mosaicing, especially in medical imaging. Comprehensive review can be found in previous surveys [139, 133, 132, 108, 85].

In general, image registration is recognized as rigid/affine and non-rigid depending

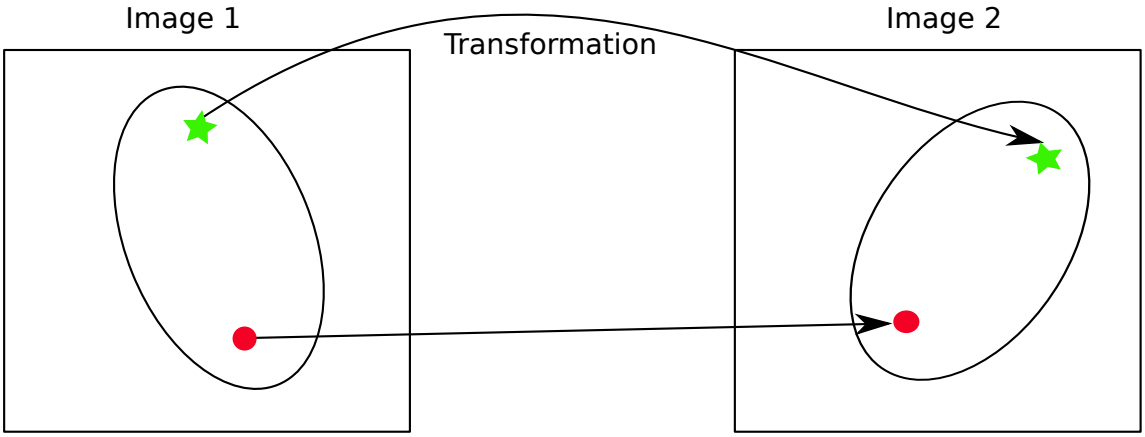

Figure 3.1 – Image registration

on the nature of the transformation of objects in the images. The rigid/affine image registration accounts for the rotational and translational transformation globally on the entire image and the more sophisticated method is called affine registration. In contrast, the non-rigid image registration locally measures small displacements and finds non-uniform mappings between the images. In medical imaging, most of the transformations are complex (e.g. deformations of body cells due to the sensor movement and heart rate, anatomical variations in brain structures of different individuals) and recognized as non-rigid so that the rigid/affine registration is no longer adequate. Non-rigid image registration satisfies the problem of different local geometric changes. It overcomes the limitations of the rigid image registration strategy.

This research focuses on the non-rigid image registration approach that account for the local movements of image elements.

3.1.1 Non-rigid Image Registration

Nonrigid image registration that finds the optimal deformable mapping between two images plays an important role in medical imaging. To explain the definition of this task more technically, the first image is referred to as the fixed image F and the other is called the moving image M. The application finds the optimal correspondence map ϕ from F to M that maximizes the similarity between F and $M \circ \phi$. In the literature, the objective function is usually defined as a combination of two components, one is the image similarity E_{Sim} between the fixed image and the moving image influenced by the transformation map ϕ, while the other term is a regularization term E_{Reg} that smooths the transformation. The transformation is then achieved by:

$$\phi_{\text{opt}} = \text{argmin}_{\phi}(E_{\text{Sim}}(F, M \circ \phi) + E_{\text{Reg}}(\phi)), \tag{3.1}$$

where the composition operator $M \circ \phi$ expresses the transformation of M according to the transformation map ϕ.

According to Sotiras *et al* [109], nonrigid image registration can be divided into three stages: transformation model, similarity measurement, and optimization method. Registration methodologies can be classified with respect to the divergence of each stage according to [109]. For instance, based on the transformation model criterion, registration methodologies can be roughly categorized into different categories such as elastic model, optical flow, spline model and diffusion model. Similarly, according to the similarity measurement criterion, the registration can be classified as geometric based method, intensity based method and hybrid method. The classification based on the optimization stage divides the existing methods into different groups as Gradient descents, Gaussian Newton, Markov random fields and random walk. This can be seen graphically in Figure 3.2

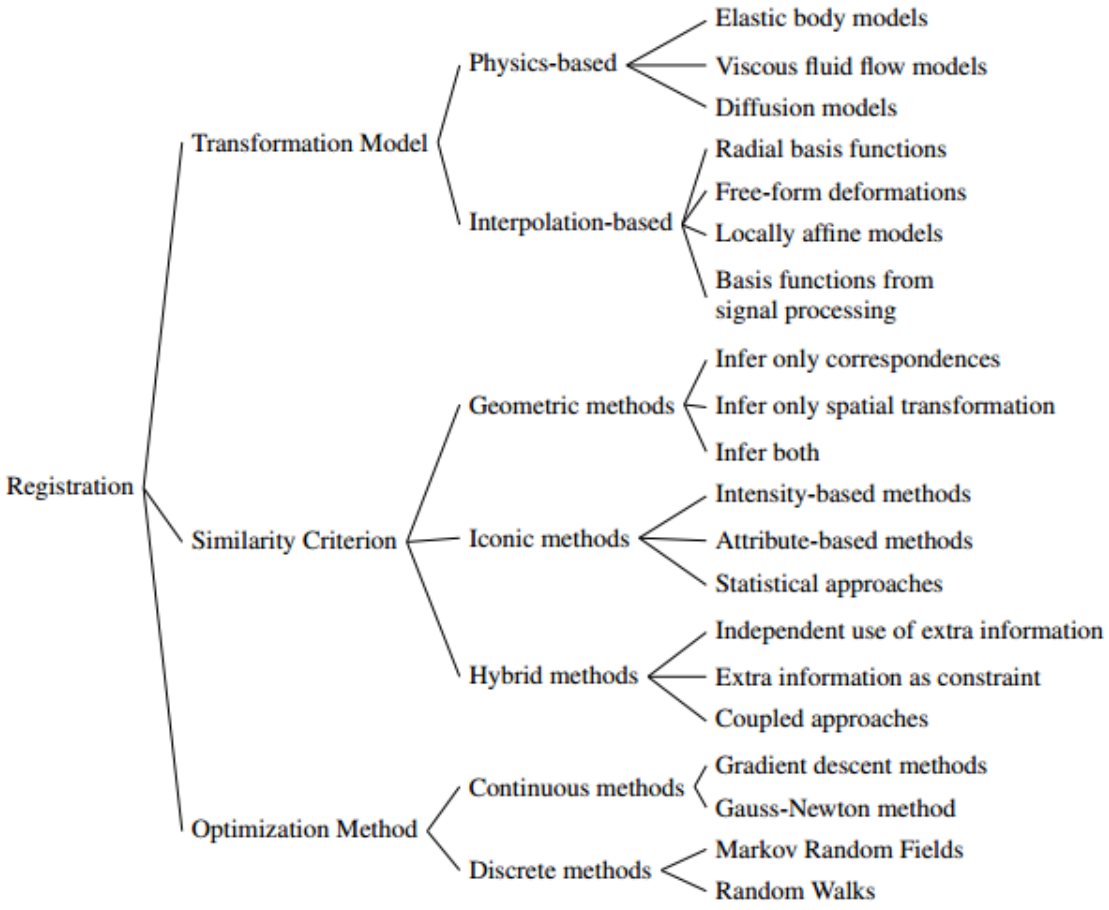

Figure 3.2 – Image registration classification (Sotiras *et al* [109])

3.1.1.1 Transformation Model

The first research on optical flow motion estimation was proposed by Lucas and Kanade in 1981 [77]. This research has since motivated a tremendous quantity of research in image registration and alignment with different models. The simple definition of motion is that one point is assumed to keep the same intensity value over time, such that:

$$I(x, y, t) = I(x + \Delta x, y + \Delta y, t + \Delta t) \tag{3.2}$$

Lucas-Kanade algorithm supposes that the flow is constant in a local neighborhood and proposed a technique that uses image intensity gradient to iteratively compute the optical flow of a patch. On the other hand, Horn and Schunk [56] minimize the mean error with an additional smoothness constraint that rather relies on the velocity of image pixel than on computing the differences in intensity. Another method that can work in case of fast movement was introduced by Bouguet in 2000 [13] that computes optical flows at different scale levels and passes the result from a higher level to a lower level.
A numerous number of other methods have been proposed over the past decades to handle the non-rigid image registration problem with different models and more sophisticated schemes. The choice of the transformation model is an important key that decides the robustness of the optimization.

The first model we can mention is the elastic deformation model. The idea of elastic based registration methodologies is that the moving image is deformed until it matches the fixed image. There exist an extensive number of researches based on this model [9, 103, 42]. Terzopoulos *et al* [112] introduced an approach for shape and non-rigid body motion reconstruction using external forces as energy constraints. Baicscy *et al* [9] and Shen *et al* [104] extended the previous works on elastic model to hierarchical schemes. More recently, in 2007, Ashburner [3] proposed a fast diffeomorphic registration based on elastic energy, in which the flow field is considered as a member of Lie algebra [72] through the exponential map. Deformations with larger magnitudes can be captured by viscous fluid models [27, 28, 20].

Since Thirion's research [114], the diffusion model has become popular and motivated other researches on the problem of deformable image registration, especially medical images. The registration consists of two main steps, namely the demons force search which is similar to optical flow and the regularization by a Gaussian kernel. Depending on how the demon forces are determined and how regularization is operated, different alternative versions of the Demons approach can be acquired.

Pennec *et al* [89] provided an insight of the Demons algorithm that the energy minimization can be considered as a second order gradient descent scheme. Cachier

et al [14] introduced a hidden auxiliary correspondence variable to put the similarity optimization and regularization in a well-posed optimization problem. The optimization on Demons framework with stationary velocity field was combined with the exponential map on the Lie group [72] to introduce a diffeomorphic registration [121], and symmetric log-domains registration [122]. Lorenzi *et al* [73] developed a registration method based on the similar stationary velocity fields. It is built upon the Log-Demons framework to parameterize the transformation. The method is adapted with the similarity metric that implements a symmetric local correlation coefficient. More recently, Hadj *et al* [47], motivated by [73], incorporated the similarity metric with a confidence mask to improve the robustness of the algorithm. Fischer *et al* [36] proposed a fast diffusion based registration that exploits the underlying PDE for the regularization. Wang *et al* [125] recommended adaptive force strength adjustment iteratively in the iteration process . That improves the performance of the algorithm. The Demons framework was extended to spherical image registration in the work of Yeo *et al* [135]. Locally adaptive regularization was proposed in [15, 86]. Mansi *et al* [81] introduced a mathematical justification of the demons Gaussian regularization, in which the Gaussian smoothing is replaced by an elastic-like regularization.

The common point of those methods is that, the motion estimation is inspired by a physical model and the transformation must be consistent with some physical properties. On the other hand, a vast number of methods are derived by some interpolation schemes where deformations are known for some given sample points of the image. In this case, the rest of the image is interpolated through an interpolation function.

One of the important models is the Thin-Plate Spline (TPS), which was early used in registration problems by Bookstein *et al* [12]. Rohr *et al* [94] take into account the localization error of each landmark for deformation field approximation based on TPS. Rohr *et al*'s research [93] is an extension of [94]. They showed that the estimation can tackle isotropic and anisotropic errors of the landmarks. Li *et al* [67] proposed a Compact Support TPS method and the support is restricted locally. Recently, the TPS can also be coupled with rigid/affine models to estimate dense matching for 3D ultrasound images [78], or is used to define the transformation while

training the images with convolutional neural networks in 3D image registration [33].

The Spline based motion model [111] takes over the majority in the class of registrations based on an interpolation strategy. The displacement field is modulated by a set of coefficients or a basis function and a set of control points. In other word, the displacement vector at each pixel is a linear combination of the displacements estimated at the control points.

The Free Form Deformation (FFD) is one of the most popular and successful models among the existing Spline based models in medical imaging. It was early proposed by [101]. The Bspline is the most successful among the spline based methods because it is smooth, fast and can handle hierarchical schemes [21, 64]. For example, Rueckert *et al* [96] first applied Bspline into 3D MRI image registration with a steepest gradient descent optimization, and later in [95]. The authors showed how the deformation field can be constrained with different penalty functions, and tested on different biomedical images. Motion estimation is sometimes performed only on some region of interest while most of the Bspline based methods use a regular grid of control points, [126] extended the problem to a method that uses an irregular grid of control points. The advantage of this model is that diffeomorphism and smoothness might be guaranteed.

From a theoretical point of view, the spline based approach, especially the FFD model allows to find smooth transformations. However, these methods suffer from performance and complexity drawbacks because of the gradient search optimization. In comparison, the Demons model originally does not guarantee smoothness, but it is fast in performance and is a strong theoretical framework that can be efficiently decoupled with a diffeomorphic transformation. Our research includes the examination of these two models to find the most appropriate framework to our resources.

3.1.1.2 Similarity Measurement

Concerning the similarity measurement, it can be referred as voxel intensity similarity or image structure similarity. Therefore, with respect to the similarity measurement, image registration can be classified as intensity based, geometric based and hybrid

method that combines the two types of measurement.

Intensity based algorithms measure image similarity directly on the image grey values. They can be referred to as template matching technique. The most popular similarity measurements that can be used are cross-correlation, intensity difference and mutual information. Intensity cross-correlation based methods estimate how two images are linearly related. The larger the value of correlation, the better the two images match with each other. Fonseca *et al* [39] measure the spatial resolution, rotation and translation for remote sensing images. Andrew Simper [107] proposed a more sophisticated system to correct more complex mis-registration rather than just translation such as perspective changes and transformations caused by lens imperfections. Rikard Berthilsson [11] were able to formulate the correlation between two images when there is an affine transformation. Although most cross intensity correlation based methods are suitable for images of same modality, Van *et al* [118, 32] showed that this method can also be applicable to match CT and MR images. Later, [110] applied a multi-resolutional scheme using cross correlation to adapt with MR-PET registration. Avants *et al* [6] maximize the cross correlation between image pairs while the moving image is iteratively warped toward the fixed image. Until now, the work still continues to gain attraction in the field of image processing [34, 5, 127].

In contrast to the Cross-Correlation based methods that maximize the image similarity, the intensity difference supposes two images that have the same structures should have the least difference, thus the optimization minimizes the difference between two images. It is usually based on the sum of square difference (SSD) [4, 41, 131, 115, 129, 7, 61, 29]. For example, [128] employs SSD as an objective function to infer the perspective transformation. [29] minimizes SSD to align HDR images with fast translation and rotation. This is the most important and widely used similarity measurement in the field of non-rigid image registration.

While most of the mono-modal image registration researches use the intensity similarity/difference, the mutual information (MI) methods are present in most of registration methods for images of different modalities [139]. In this method, images are supposed to have the maximal statistical dependence when they are best

aligned. For example, Collignon *et al* [25] measure the entropy of the joint probability distribution of the intensities of matched points in the two images. [123] presents an approach to MR and CT image registration. Maes *et al* and Collignon *et al* [79, 24] compute the entropy of the joint histogram. In [113], mutual information optimization is adapted to multi-resolution image pyramids.

In contrast to the intensity based method, the geometric based method is also known as feature based method that takes into account the geometrical structures or landmark information (e.g. edges, shapes, contours, graphs, surfaces,...) of the images. The feature based technique is divided into two stages: feature extraction and feature matching. Different key point detectors to extract features were proposed in the literature such as Harris [49], SIFT [74] and the variants, SURF [10] and the variants. Region, edge, corner, point or shape can also be seen considered as features. For example, the region feature is usually applied to nature images that focus on image with region of interest such as forests, lakes, fields, urban areas [40, 46, 50, 57, 102]. The edge feature based approach is efficient for images where edge information is well preserved. For instance, Li *et al* [66] proposed a contour-based approach to multisensor images. Li *et al* [68] proposed a matching method of aerial road network. Vujovic *et al* [124] identified the potential control points via detection of elongated vertical structures of mammographic images and established the correspondence between these points. Lastly, feature extracted by wavelets is also widely used because of its ability to support multi-resolution scheme and image representation in both time and frequency domains, as well as its ability to characterize texture images. In this case, the image features are extracted via wavelet decomposition. The registration step then becomes a feature matching problem [53, 38, 134, 88]. Once the features are determined, they are put into the feature matching problem.

In the irregular sampling context, the points have floating coordinates and the images have different point densities at different regions of the images. It is difficult to perform a feature matching based on a keypoint detector (e.g. SURF, SIFT) approach. In addition, the images contain much noise and complex texture, a shape based approach such as wavelets that can characterize the shape and texture of the

images is more appropriate in this context. Furthermore, as stated earlier, the study of irregular data needs a good representation that can mathematically characterize the data structure.

Recently, graph matching became popular to formulate a feature matching problem, in which structural constraints are formulated as an attribute of graph matching problem. Graph is a flexible and powerful tool to characterize different kinds of data regardless of whether the data is regular or irregular. A review on graph theory and matching is proposed in the following chapter of this thesis.

The intensity based technique is usually operated by a least squares optimization. Thus, it has the possibility to fall into local minima of non-convex optimization and it is computationally expensive to optimize the full image parameters. Moreover, intensity information alone does not guarantee the matching of objects with structural changes. In other words, this method lacks geometric invariance and is only suitable for images with small displacements. The geometric based technique is more robust to structural changes and scene movements with global transformation. It is, however, limited in case of local deformation and the parts of the image that are not in the feature selection are not considered during the registration process.

Motivated by the fact that intensity based and geometric based methods complement each other, many recent works have combined the two techniques together for more robust matching. The act of combining both methods is known as the hybrid method. Because of the ability to capitalize the advantages of intensity based and geometric based methods, most of the existing applications use the hybrid method for registering images. For instance, the hybrid method can be operated in a hierarchical scheme [87, 136, 58] that registers images at multiple scales. In [87], landmark based registration is operated at a coarse scale. Then, the result is propagated as initialization for Bspline registration at finer scales. In each scale in [136] the image is registered alternatively with landmark based and intensity based methods. The resulting transformation from intensity based registration is passed to the next landmark based registration of the next scale. Authors [16] obtained non-rigid transformation by incorporating structural registration and grey-level registration. Instead of splitting landmark registration and intensity registration, some methods

utilize structural information as a constraint to optimize an objective function [54, 76, 75, 8, 106, 71].

Recently, the intensity based approach coupled with spectral matching has found great success in terms of medical image registration [71]. This method utilizes the Graph Spectrum to register images under the Log-Demons framework. The success of this approach motivates our research using graph based method and the Log-Demons framework. Let us here provide a brief review of the classical Demons method and its variants.

3.1.2 Demons Framework and the Variants

Biomedical image registration applications are constrained with several aspects. Two of the great important constraints are symmetry and diffeomorphism. The former imposes that the resulting deformation does not depend on the order of the input images while the later constraints the transformation to be smooth under large deformation. However, the elastic model in general is still limited to large deformation and is not invertible while the viscous fluid model is computationally inefficient [108]. The Demons algorithm is famous for being computationally efficient. It has inspired a lot of research in symmetric registration and diffeomorphism [119, 73, 6], although the original one [114] is non-diffeomorphic. Let us here briefly review different methods based on the Demons framework from the classical one to the symmetric diffeomorphic version.

3.1.2.1 Classical Demons

The Demons approach proposed by Thirion [114] performs a non-rigid image-to-image matching as a diffusion process. It is a fast and efficient scheme, simple to implement that provides linear computational complexity [138]. Thus, it has inspired a various number of researches. The demons force was inspired from the concept of Maxwell's demons in the field of thermodynamics and optical flow equation in image processing field. Classically, the goal of optical-flow based image registration is to find the dense motion field s from the fixed image F tothe moving image M that maps

the intensity space I_F of F to the intensity space I_M of M . The transformation is acquired by optimizing the objective function that is defined according to a similarity and a regularity measure:

$$E(F, M, s) = \alpha_i E_{\text{Sim}}(F, M, s) + \alpha_r E_{\text{Reg}}(s), \tag{3.3}$$

where the weighting parameters α_i, and α_r respectively control the intensity similarity and the level of smoothness of the transformation field, and $\alpha_i + \alpha_r = 1$. Classically, the intensity term can be denoted by the sum of square error or mean square error of intensities of the two images, such that the similarity term is defined by $E_{\text{Sim}}(F, M, s) = ||I_F - I_{M \circ s}||^2$, and the regularity term is defined by $E_{\text{Reg}}(s) = ||\nabla s||^2$. The notation $||.||$ defines the L2 norm and the notation ∇s means that a Gaussian filter is applied to s. The optimization is therefore operated in two steps. The first step is to find the demon forces at every point under the optical flow constraint. The second step is regularization acquired by applying a Gaussian filter to the transformation field.

3.1.2.2 Alternative to Classical Demons

The energy function in Equation 3.4 indeed leads to a well-pose problem that the smoothness is guaranteed by the regularization term. However, the mixing of the similarity criterion and the regularization makes it difficult to theoretically justify how the optimization operates and makes the optimization steps computationally intensive, according to [120]. For a more tractable sub-problem optimization, a hidden auxiliary variable c is used to decouple the similarity optimization and the regularization[14]. The global energy function with respect to the current transformation and hidden correspondence is defined by:

$$E(F, M, s, c) = \underbrace{\alpha_i E_{\text{Sim}}(F, M, c) + \alpha_x \text{dist}(s, c)^2}_{\text{Correspondence}} + \underbrace{\alpha_r E_{\text{Reg}}(s)}_{\text{Regularization}}. \tag{3.4}$$

The second term $\text{dist}(s,c)^2 = ||s-c||^2$ helps draw the hidden variable c close to the actual transformation field s, and α_x controls the correspondence uncertainty. The optimization is an iterative scheme. In each iteration, correspondence is obtained through a free form update field u with an optical flow method to minimize the first composition called "Correspondence" as in Equation 3.4. And then the regularization is to minimize the second composition called "Regularization", that is acquired by applying a fluid like Gaussian filter with kernel (K_{fluid} whose standard deviation is σ_{fluid}) to the whole transformation field ($s \leftarrow K_{\text{fluid}} \star (c+u)$).

3.1.2.3 The Log Demons

One of the limitations of the Demons method is that it does not guarantee diffeomorphism. Diffeomorphism maintains the topology of the object and prevent transformation from folding onto itself. The Log-Demons registration proposed by Vercauteren *et al* [121] provides an invertible and diffeomorphic registration. It is parameterized on the Lie algebra [72] through the exponential map of a stationary velocity field v, with $s = \exp(v)$ resulting to a smoother and invertible registration compared to the classical Demons method. The computation of the exponential map of velocity field is estimated with the scaling and squaring method that was well described in [121].

3.1.2.4 Symmetric Log-Demons

The Log-Demons framework is invertible but is not symmetric. The term "symmetric" refers to the transformation that ignores the roles of the input images ($s_{F\to M} = s_{M\to F}^{-1}$) which leads to more consistent registration. The Log-Demons framework is diffeomorphic and invertible, thus, the inverse of the transformation can be obtained with backward computation $s^{-1} = \exp(-v)$. The symmetric registration is acquired by minimizing the cost function combining computations from forward and inverse mappings $s_{\text{sym}} = \text{argmin}_s(E(F,M,s) + E(M,F,s^{-1}))$, that was introduced in [122]. The optimization is achieved by using similar operation as in the previous version except that the velocity field is computed in forward and backward

mappings. Although the Demons approach of the original formulation is not diffeomorphic and symmetric, it is still a strong theoretical and fundamental foundation that broadens more robust methods. The underlying optimization framework allows to easily combine the classical intensity and spatial constraints with additional constraint (such as shape) for robust registrations. It is, in addition, an appropriate framework to incorporate with irregular data since it was originated by the Demons forces of irregularly distributed points.

A more elaborate description of the Demons, the Log-Demons and the Symmetric Log-Demons schemes will be provided in the next chapter of this manuscript.

3.2 Summary and Discussion

In this chapter, a review of the different nonrigid image registration methods is provided. These methods were roughly classified depending on the choices of the transformation model, the similarity measurement and the optimization method. The choice of the transformation model can either be among a physical model or a model derived by an interpolation scheme. The transformation based on physical model must be consistent with some physical properties such as elastic approach and demons approach. The transformation based on interpolation model is interpolated by some known sample points such as the Spline family models, also known as parametric models.

The Demons approach is known to be fast to execute and simple to implement and these properties motivate an extensive number of successful researches in the field of medical imaging. Although the classical one is limited to small deformations, it is still a fundamental framework and a solid theoretical foundation in the literature that allows researchers to propose much more powerful frameworks. A part of our research is also motivated by the Demons approach that will be discussed later in this manuscript.

The choice of similarity measurement was classified as intensity based, geometric based and hybrid based approaches. The intensity based method and the geometric based method alone have their own limitations. In fact, they complement each

other. The hybrid based approach that combines both intensity and geometric based approaches is more preferable in the literature. The graph based image processing has been well studied in the past decades as the graph representation is simple, flexible and efficient to model different types of data.

The graph spectrum is isometric invariant and can be exploited in a spectral matching method, as well as in image registration method as a geometric constraint in combination with an intensity based matching. The Spectral Log-Demons method [70] uses the graph spectrum in combination with the Log-Demons framework. This method can capture fast and complex deformations. However, the robustness to noise is one of the most important aspects in medical imaging, but the Log-Demons method was found to be sensitive to noise [70]. Our work using graph spectrum in combination with classical registration frameworks (e.g. Demons and Bspline) on regular grid will be described in details in the next chapter of this manuscript. We examine the interactions of graph spectrum to registration, and to find an appropriate transformation model as well. The contribution of this research using Spectral Graph Wavelets for registration of noisy images is later described in the last section of the next chapter. This method outperforms the performance of the existing Spectral Log-Demons method.

Chapter 4

Graph-based Image Registration on a Regular Grid

Contents

4.1 Introduction 34

4.2 Graph Theory 35

4.2.1 Review on Graph Theory 35

4.2.2 Graph definition 37

4.2.3 Spectral Graph Theory 40

4.3 From Demons Framework to Spectral Demons 45

4.3.1 Demons Framework 45

4.3.2 Spectral Demons 49

4.3.3 Application of the process to microscopic images 53

4.4 Spectral Bspline 57

4.4.1 Bspline Registration 57

4.4.2 Spectral Bspline Image Registration 61

4.4.3 Results 62

4.5 Spectral Graph Wavelet (SGW) based Image Registration 66

4.5.1 Objective function 67
4.5.2 Results 69
4.6 Conclusion 77

4.1 Introduction

This chapter describes different non-rigid image registration methods on biomedical images on regular grids with the graph approach. Let us consider that we have two images, a fixed image F with its intensity space denoted as I_F and a moving image M with I_M is its intensity space. The intensity spaces I_F, I_M are respectively set on the regular Cartesian coordinate spaces $X_F, X_M \in \mathbb{N}^2$. The goal of registration is to find an appropriate transformation s that maps the intensity spaces of the fixed image and the moving image. In practice, the mapping is not only applied to the intensity space but also to the spatial space, and more generally on the feature space extracted from the images to guarantee the registration problem is well-posed. One of the powerful tools that is recently utilized in the image registration problem is the Spectral Graph theory. In the Spectral Graph theory, the graph spectrum was used as the geometric constraint in the matching as presented in the work of Lombaert *et al* [70] and the registration captures large and complex deformations although it still suffers from noise.

This chapter begins with the introduction to the state of art of the Graph Theory as well as an overview of the Spectral Graph Theory. Then, two well-known frameworks Bspline and Demons in medical imaging are examined to utilize the graph spectrum as geometric constraint for the registration of biomedical images on a regular grid. Motivated by the intuition that the graph spectrum is invariant to isometry but sensitive to noise, this work proposes a registration method using Spectral Graph Wavelets as geometric constraints. The Spectral Graph Wavelet decomposition proposed by Hammond *et al* is defined through the Spectral domain. Thus, the Spectral Graph Wavelets carry out the similar characteristics as the graph spectrum. In addition, similar to the classical wavelets, the Spectral Graph Wavelets also represent

the image hierarchically with different levels of details. The experimental results of the proposed method that uses Spectral Graph Wavelets outperform the existing method that uses graph spectrum, especially when noise exists. Our contribution *"Spectral Graph Wavelet based Nonrigid Image Registration"* [92] was published in the conference **ICIP** *(International Conference on Image Processing)* taking place in Athens, Greece, in October 2018. This method will be described in the last section of this chapter.

4.2 Graph Theory

In the recent years, the signal processing on graphs has emerged in many different fields with different forms of signals (e.g, computer vision, sensor networks, traffic,...) due to the development of technology. This is because a graph is a simple and flexible model to structurally represent different types of data. In addition, graphs do not depend much on the data structure whether it is regular or irregular. The large literature allows us to easily find an appropriate model for our research. This section provides a review on graph theory and signal processing on graphs.

4.2.1 Review on Graph Theory

Graph based methods have been efficiently applied in the fields of networking, social network, transportation, biology, sensor. In graph based methods, data are represented on vertices of weighted or unweighted graphs. The idea of applying graph theory in image processing was known in the early 1970s [137]. Since then, many image processing applications have been deployed thanks to pixel adjacency graphs. Graph based approaches allow minimalistic and flexible representation of different types of images. They provide a discrete and mathematically simple representation to develop more efficient and accurate methods. In addition, graph based methods allow generic representation forms that can describe the geometric structures of voxels, as well as pixels. Common image processing tasks such as filtering, inpainting [18, 80], matching [37] were efficiently solved using graph representation of data.

Signal processing on graphs is an extension of classical discrete signal processing which is more complex and has irregular structure. Approaches to the shift operator of graph signal can be found in [45]. Such approaches build an isometric graph translation operator in spectral domain as a phase shifting, which shows that graph shift shares properties with the time shift. Shuman *et al* [105] gave an introduction of an emerging field of signal processing on graphs that merges algebraic and spectral graph theoretic concepts to process high dimensional data on graph. The discrete Signal Processing on Graphs theory such as frequency analysis can also be found in the research of Sandryhaila *et al* [99].

Graph sampling theory can be found in [17, 90, 2]. Anis et al [2] extended the Nyquist-Shannon theory of sampling to band-limited signals defined on arbitrary graphs. The authors found a condition for a unique recovery of band-limited signal from its samples and provided a method of computing cut-off frequency for a given sampling set. On the contrary, [97] described a method to oversample signals defined on a graph by using an oversampled Laplacian matrix, in which the original graph has to be decomposed into bipartite subgraphs. Chen et al in 2015 [19] studied signal recovery on graphs based on random sampling and experimentally designed sampling. At the same time, the authors proposed a class of smooth bandlimited graph signals, and accordingly proposed a recovery strategy based on a random experimental sampling. Later, they proved the possibility of perfect recovery of previous sampling approaches and studied the qualified sampling operator assigned to those approaches in [17].

[48, 83, 98, 26] introduces different graph based transformations. In particular, Crovella *et al* [26], Narang *et al* 2010 [83] and Hammond *et al* in 2011 [48] provided different approaches for the graph signal wavelet transform. The graph wavelets in Crovella *et al* [26] were defined on unweighted graphs for computer network traffic analysis. The wavelet function is designed using the geodesic distance. In this case, the value of a wavelet centered at one vertex on another depends only on the shortest distance between the two vertices. In the research of Hammond [48], the spectral graph wavelets decomposition is defined on a weighted graph. The spectral graph wavelets can be approximated using Chebyshev polynomial approximation

that avoids heavy computation for diagonalizing the Laplacian matrix.

In image processing, different graph based image denoising methods have been proposed due to the different graph wavelet decomposition methods. For instance, authors [80] proposed a denoising and inpainting application for color and multicomponent images using the graph wavelets defined through the spectral domain. The graph spectrum is also used in spectral matching. Spectral matching has been applied in many fields such as shape registration in images and segmentation of shapes. Spectral matching that uses the graph spectrum to find vertex correspondence was earlier proposed by [117], and later by Scott *et al* [100] Chung *et al* [22], and recently used in image registration [70]. Let us here illustrate the graph definition and the signal processing on graphs.

4.2.2 Graph definition

This section begins with the definition of a graph. Basically, a graph is defined as $G = (\mathcal{V}, \mathcal{E})$. It consists of a finite set of vertices $\mathcal{V} = \{v_0, ..., v_{N-1}\}$ where N is the number of vertices in the graph and a set of edges $\mathcal{E}$ representing the pairwise relationships between vertices [22]. Each edge $e_{ij} \in \mathcal{E}$ connects two vertices v_i and v_j with $i \neq j$.
A finite dataset $f = \{f_0, ..., f_{N-1}\}$ is a graph signal if it is indexed by a graph $G = (\mathcal{V}, \mathcal{E})$ where each coefficient f_i in f is indexed by a vertex $v_i \in \mathcal{V}$. The edge weights represent the relations between coefficients in f. In graph based image processing, each vertex can be a pixel or an image region and an edge depicts the relationships between neighboring pixels or regions.
For a better understanding of how a graph is applied to image processing, suppose we define a graph over a simple discrete image. A graph is defined over the whole image where each pixel is represented as a vertex and each two vertices are connected if they are in the vicinity of Euclidean distance 1 (Figure 4.1). A weighted graph is a graph whose each edge e_{ij} is associated with a weight value w_{ij} defined with a function $w : \mathcal{V} \to \mathbb{R}$. The graph is represented by an adjacency matrix $A \in \mathbb{R}^{N \times N}$,

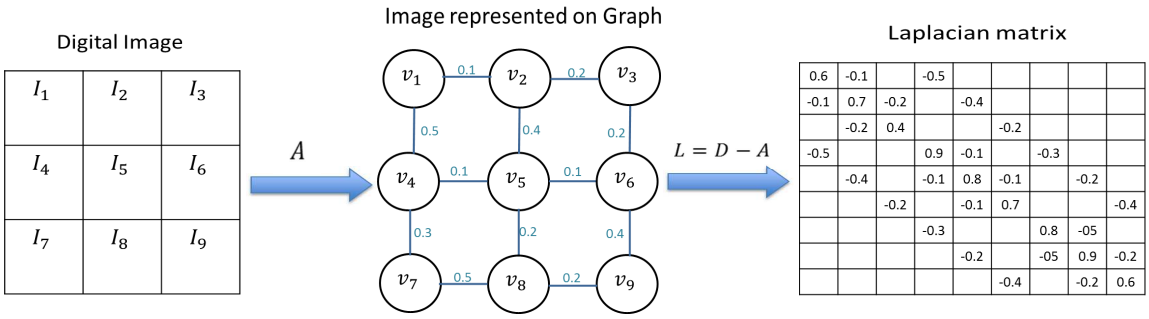

Figure 4.1 – Example of graph representation of digital image and the graph Laplacian matrix associated with the graph.

such that:

$$A_{ij} = \begin{cases} w_{ij}, & \text{if } e_{ij} \in \mathcal{E}, \\ 0, & \text{otherwise.} \end{cases} \tag{4.1}$$

For an undirected graph, the adjacency matrix is a zero-diagonal symmetric matrix.

The construction of the graph mainly focuses on point connectivity and the computation of edge weights. A simpler definition of adjacency matrix can be uniform, in which $A_{ij} = 1$ if v_i, v_j are connected and $A_{ij} = 0$ otherwise. Different metrics can be applied to compute the edge weights. Commonly for digital images, weights can be uniform. Each edge connects two neighboring vertices (pixels) v_i and v_j with a weight $w_{ij} = 1$. In a more sophisticated case, edge weights are defined under the influence of the intensity difference between adjacency pixels by a Gaussian kernel, defined as:

$$w_{ij} = \begin{cases} \exp\left(-\frac{(I_i - I_j)^2}{K^2}\right) & \text{if } (i,j) \in \mathcal{E}\ , \\ 0 & \text{otherwise.} \end{cases} \tag{4.2}$$

Parameter $K > 0$ controls the sensitivity to edges in the images. In other word, the value of K affects the influence of the difference between every two adjacent pixels. When the value of K increases, the influence of pixel difference decreases. In particular, when K is large, the value of the edge weight is closer to 1, and when K is small, the value of the edge weight is closer to 0.

If the value of K is fixed and small enough, the values of edge weights then depend on the intensity difference between adjacency pixels. Edges that connect pixels from different regions are given low weights and edges that connect pixels in the same uniform intensity region are given high weights.

K is chosen depending on the noise and texture characteristics of the image. In some cases, the edge weights also depend on the Euclidean distance between adjacency points in the way that they are inversely proportional. The weight is, thus, given as:

$$w_{ij} = \begin{cases} \frac{\exp\left(-\frac{(I_i - I_j)^2}{K^2}\right)}{||\mathbf{x}_i - \mathbf{x}_j||^2} & \text{if}(i,j) \in \mathcal{E}, \\ 0 & \text{otherwise.} \end{cases} \tag{4.3}$$

Concerning the graph topology, there is no general rule of how points are connected. In general case, one can use the k-nearest neighbor scheme to find adjacent points, or for each point, choose its adjacent points in one circle. In the case of regular data, such as an image, each pixel in the image is considered as one vertex and each vertex can be connected with its four closest neighbors, or with additional diagonal neighbors. In principle, for stronger graph connection, edges can be built on pixels with any larger spatial distance, but the graph communication cost will increase.

Degree d_i of vertex v_i is the sum of the weights of all the edges incident to vertex v_i:

$$d_i = \sum_j A_{i,j}. \tag{4.4}$$

The degree matrix D of a graph is a diagonal matrix where each value D_{ii} on the diagonal is the degree of vertex v_i, therefore $D_{ii} = d_i$.

The Laplacian matrix is given as $L = D - A$, and represents the algebraic connectivity of vertices in the graph as the adjacency matrix. In particular, each element (of the matrix L_{ij} or A_{ij}) of the Laplacian matrix that is not on the diagonal indicates whether the two vertices v_i and v_j are connected or not, and the strength of the connection. But the spectrum of the Laplacian matrix plays an important role in many researches in the literature (segmentation [35, 55], image retrieval ([82]) shape

matching [62]). Next, a brief review of the spectral graph theory will be provided.

4.2.3 Spectral Graph Theory

The sets of eigenvectors and eigenvalues of the Laplacian matrix form the Laplacian spectrum of the graph. For an undirected and non-negative weight graph, the Laplacian matrix L is symmetric, and positive semidefinite. Thus, it can be represented via the spectral theorem:

$$L = \chi \Lambda \chi^{\top}, \tag{4.5}$$

where Λ is a diagonal matrix with the eigenvalues $0 \leq \lambda_1 \leq \lambda_2 \leq ... \leq \lambda_N$ on the diagonal, and X is an orthogonal matrix whose columns are the eigenvectors $\chi_1, \chi_2, ..., \chi_N$. From now on to the following chapters of this manuscript, the term $\chi = \chi_1, \chi_2, ..., \chi_N$ denotes the set of eigenvectors of the Laplacian matrix, also considered as the spectral coordinates of graph signals.

L is symmetric and the sum of each row in the matrix is equal to 0. Therefore, it is positive semi-definite and the first eigenvalue is equal to 0. The eigenvector associated with the second smallest eigenvalue is called Fiedler vector [22], and it is an important tool for image segmentation. Since all the eigenvalues of the Laplacian matrix are non-negative, they can be interpreted as the frequencies existing in the associated graph, and the corresponding eigenvectors represent the frequency components.

Let us here give a sample of data representation on a graph and its graph spectrum. Suppose we have a graph signal $\mathbf{f} = (0.5, 0.8, 1, 0.4)^{\top}$. The edge weights are denoted as the absolute error between neighboring points. The adjacency matrix and the Laplacian matrix are, thus, denoted as follows:

$$A = \begin{pmatrix} 0 & 0.3 & 0 & 0 \\ 0.3 & 0 & 0.2 & 0 \\ 0 & 0.2 & 0 & 0.6 \\ 0 & 0 & 0.6 & 0 \end{pmatrix} \tag{4.6}$$

$$L = \begin{pmatrix} 0.3 & -0.3 & 0 & 0 \\ -0.3 & 0.5 & -0.2 & 0 \\ 0 & -0.2 & 0.8 & -0.6 \\ 0 & 0 & -0.6 & 0.6 \end{pmatrix} \tag{4.7}$$

The graph representation and graph spectrum of the signal $\mathbf{f}$ are respectively given in Figure 4.2a and Figure 4.2b.

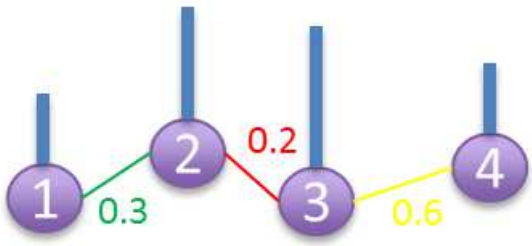

(a) Graph representation

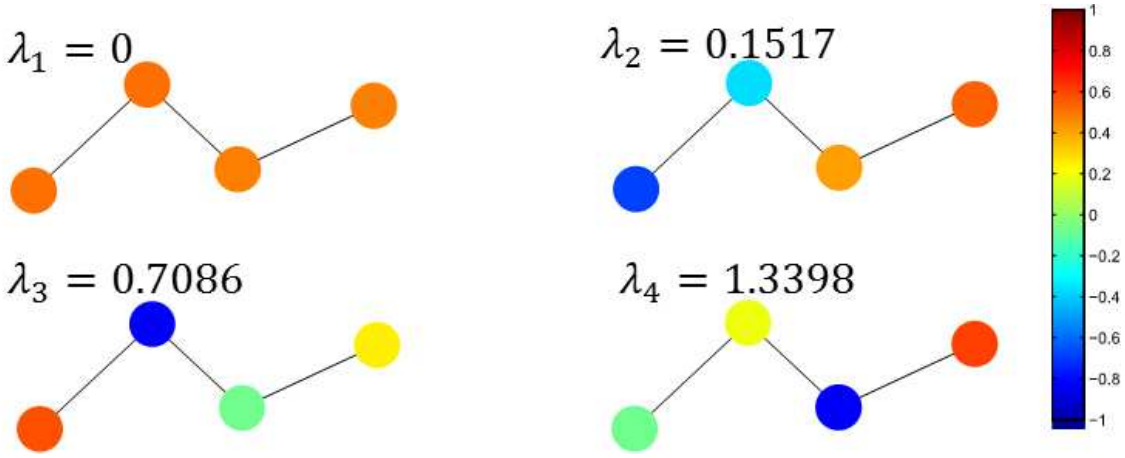

(b) Graph spectrum

Figure 4.2 – Example of graph representation and graph spectrum of signal $\mathbf{f} = (0.5, 0.8, 1, 0.4)^\top$.

The discrete Laplacian operator in the graph domain is in analogy with the standard Laplacian operator of the Euclidean domain. In fact, in the case where the

graph signal is defined on a regular mesh, the graph Laplacian corresponds to the Laplacian in the continuous domain. Looking at the example on Figure 4.2b, showing the eigenvalues and the corresponding eigenvectors presented as the graph signal. It can be seen that, as we go from low eigenvalue to high eigenvalue, we actually move from the low frequency component to the high frequency component. Conceptually, the eigenvectors of the Laplacian matrix are similar to the Fourier basis elements in the Euclidean space. Therefore, they are used to define the graph Fourier transform [65].

4.2.3.1 Graph Fourier Transform

Forward Transform: Given a graph signal $f \in \mathbb{R}^N$, according to [99] the graph Fourier transform of the signal at frequency λ_ℓ is defined through the spectrum of graph Laplacian matrix as:

$$\hat{f}(\ell) =< \chi_\ell, f >= \sum_{n=1}^{N} \chi_\ell(n) f(n). \tag{4.8}$$

The $\hat{f}(\ell)$ is considered as the ℓth graph Fourier coefficient of f.

Inverse Transform: The inverse graph Fourier transform is formulated by:

$$f(n) = \sum_{\ell=1}^{N} \hat{f}(\ell) \chi_\ell(n). \tag{4.9}$$

4.2.3.2 Spectral Graph Wavelet Transform

Unlike Fourier transform which encompasses frequency components of the signal, the wavelet transform allows to simultaneously decompose the signal in both frequency domain and spatial domain. Classically, translating and scaling are simultaneously operated on a mother wavelet ψ in order to define an analysis basis. Wavelet coefficients are computed by taking inner product of the input function with these translated and scaled waveforms. However, it is difficult to directly apply scaling operation on signal defined on an irregular graph. To deal with this problem, Ham-

mond *et al* [48] proposed a spectral graph wavelet transform that is cast into the graph Fourier domain, in terms of the eigensystem of the graph Laplacian matrix. The graph wavelets are modulated by a spectral graph wavelet generating kernel g, which performs as a band-pass filter in the spectral domain. Therefore, g satisfies $g(0) = 0$ and $\lim_{x\to\infty} g(x) = 0$.

Let g be the given wavelet kernel, $T_g^t = g(tL) = \chi g(t\lambda)\chi^\top$ are the wavelet operators at scale t. According to 4.8, the Fourier transform of wavelet operator acting on given signal f is given by:

$$\widehat{T_g^t f}(\ell) = g(t\lambda_\ell)\hat{f}(\ell), \tag{4.10}$$

and the Inverse Fourier transform is written as:

$$(T_g^t f)(n) = \sum_{\ell=1}^{N} g(t\lambda_\ell)\hat{f}(\ell)\chi_\ell(n). \tag{4.11}$$

Apply spectral graph wavelets to an impulse on a single vertex i at scale t, with notice that $\delta_i(\ell) = \chi_i^\top \chi_\ell$ and $\hat{\delta}_i(\ell) = \sum_{n=1}^{N} \chi_\ell(n)\delta_i(n) = \chi_l^\top(i)$, we have:

$$\psi_{t,i}(n) = (T_g^t \delta_i)(n) = \sum_{\ell=1}^{N} g(t\lambda_\ell)\chi_\ell^\top(i)\chi_\ell(n). \tag{4.12}$$

The coarse coefficients of graph signal f at scale t are defined as:

$$\begin{aligned} W_f(t,i) &=< \psi_{t,i}, f >= (T_g^t f)(i) \\ &= \sum_{\ell=1}^{N} g(t\lambda_\ell)\hat{f}(\ell)\chi_\ell(i). \end{aligned} \tag{4.13}$$

Observing the computation of the wavelet coefficients, the mapping of a graph signal f to its wavelet coefficients on a vertex i at scale t is a process of multiplying $\hat{f}$ by the kernel function, and then applying the inverse Fourier transform.

Scaling Function: As mentioned above, the kernel function g represents a band-pass filter in the spectral domain. In order to encode the low frequencies of signal

f, a second class of waveforms h is defined similarly to the low pass filter in classical wavelet transform, such that: $h(0) > 0$ and $\lim_{x\to\infty} h(x) = 0$. The scaling functions are denoted by:

$$\psi_i^s = T_n\delta_i = h(L)\delta_i, \tag{4.14}$$

and the wavelet coefficents of scaling function:

$$W_f^s(i) =< \psi_i^s, f > . \tag{4.15}$$

Given a graph signal $f \in \mathbb{R}^N$, suppose we analyse graph spectral wavelets of f at J scales, the constructed wavelets then compose of $J + 1$ spectral components, each component is a vector of N elements. In this research, the same formulations of cubic spline generating kernel function g and scaling function with [48] is utilized, such that:

$$g(x) = \begin{cases} x^2 & \text{for } x < 1 \\ -5x + 11x - 6x^2 + x^3 & \text{for } 1{\leq}x{\leq}2 \\ 4x^{-2} & \text{for } x > 2. \end{cases} \tag{4.16}$$

The Spectral Graph Wavelet decomposition of a graph signal f at t scales and with a generating kernel function g is summarized in Algorithm 1.

Input: $f, t, g(x)$
Output: W_f
Do:

Compute adjacency A;

$L \leftarrow A - D$;

$\chi, \Lambda \leftarrow eigendecomposition(L)$

$W_f(t, i) \leftarrow \sum_{\ell=1}^{N} g(t\lambda_\ell)\hat{f}(\ell)\chi_\ell(i)$;

Algorithm 1: $computeSGW()$

4.3 From Demons Framework to Spectral Demons

The Demons framework, as mentioned earlier, is a computationally efficient and easy to implement method. The success of Demons based methods on different types of medical images show that it is an important and powerful technique in the field of medical imaging. From the classical Demons which is non-diffeomorphic, different methods were proposed to give symmetry and diffeomorphism. Lately, spectral graph theory was embedded in a feature matching problem under the Log-Demons framework to capture larger and more complex deformations by the work of Lombaert *et al* [71]. This section provides the evolution from the Classical Demons framework to the graph based Demons method called Spectral Demons image registration and experiments of the Spectral Demons method on biomedical images.

4.3.1 Demons Framework

Recall that the classical Demons proposed by Thirion [114], the goal is to find a dense transformation s from fixed image F to moving image M such that $I_F = I_{M \circ s}$, where I_F and I_M are respectively the intensity space of F and M. It optimizes the objective function in an iterative scheme. Firstly, it computes a free form update field at each step with an optical flow method. Secondly, Gaussian filter is applied to the whole field at each step to obtain a smooth displacement field. The objective function consists in two terms. The first term, intensity similarity measure accounts for matching: $E_{\text{Sim}}(F, M, s) = ||I_F - I_{M \circ s}||^2$. The second term is a regularization to ensure that the transformation is smooth and is usually formulated as: $E_{\text{Reg}}(s) = ||\nabla s||^2$. Thus, the transformation is acquired by optimizing the objective function:

$$E(F, M, s) = \alpha_i ||I_F - I_{M \circ s}||^2 + \alpha_r ||\nabla s||^2, \tag{4.17}$$

where the weighting parameters α_i, and α_r respectively control the intensity similarity and the level of smoothness of the transformation field.

As explained in the previous chapter, Cachier *et al* [14] introduced a hidden auxiliary variable c to mathematically clarify the decoupling of intensity correspondence

and regularization in the optimization, as mentioned earlier. The additional term $\text{dist}(s,c)^2 = ||s-c||^2$ accounts for the correspondence uncertainty with the weight of α_x.

The global energy function with respect to the current transformation and hidden correspondence is defined by:

$$E(F,M,s,c) = \alpha_i||I_F - I_{M\circ c}||^2 + \alpha_x||s-c||^2 + \alpha_r||\nabla s||^2. \tag{4.18}$$

The optimization is an alternate optimization over c and s. In each iteration, correspondence is obtained by computing a free form update field (u) with an optical flow method to minimize the first composition $\alpha_i E_{\text{Sim}}(F,M,c) + \alpha_x \text{dist}(s,c)^2$, with respect to c, supposing s is given. The intermediate update field u is computed using the second order of Gauss-Newton algorithm that is based on the image gradient:

$$u = -\frac{I_F - I_{M\circ s}}{||\nabla I_{M\circ s}||^2 + \frac{\alpha_x}{\alpha_i}|I_F - I_{M\circ s}|^2}\nabla I_{M\circ s}, \tag{4.19}$$

where the composition operator $M \circ \phi$ expresses the transformation of M according to the transformation map ϕ. In this context, the transformation of M with respect to s is performed by an interpolation method.

Then, the second composition $\alpha_x \text{dist}(s,c)^2 + \alpha_r||\nabla s||^2$ is minimized, with respect to s, supposing c is given. This is acquired by applying a fluid like Gaussian filter K_{fluid} (with σ_{fluid}) to the whole update field. Then, an additional step of smoothing is applied on the whole transformation field with diffusion Gaussian kernel K_{diff} (with σ_{diff}). The optimization is illustrated in Algorithm 2 (where the notation $\star$ accounts for the convolution operator).

The Log-Demons registration proposed by Vercauteren *et al* [121] is parameterized on the Lie algebra [72] through the exponential map by a stationary velocity field v, with $s = \exp(v)$ and $c = \exp(v_c)$ resulting to a smoother and invertible registration (such that $s^{-1}s = \mathbf{I}$) compared to the classical Demons method. Thus, the

Input: $F, M, \text{maxiter}$
Output: s
Initialize: $s \leftarrow 0$, $i \leftarrow 0$
while $i < maxiter$ **do**
  $u \leftarrow -\frac{I_F - I_{M\circ s}}{||\nabla I_{M\circ s}||^2 + \frac{\alpha_x}{\alpha_i}|I_F - I_{M\circ s}|^2}\nabla I_{M\circ s}$;
  $u \leftarrow K_{\text{fluid}} \star u$;
  $c \leftarrow s + u$;
  $s \leftarrow K_{\text{diff}} \star c$;
  $i \leftarrow i + 1$;
end

Algorithm 2: Classical Demons

energy function is written in the Log-Demons domain as following:

$$E(F, M, \exp(v), \exp(v_c)) = \alpha_i||I_F - I_{M\circ\exp(v_c)}||^2 + \alpha_x||v - v_c||^2 + \alpha_r||\nabla v||^2. \quad (4.20)$$

The transformation update is alternated with an intrinsic update step on the Lie group [72] of diffeomorphisms: $s \leftarrow s \circ \exp(u) = \exp(v) \circ \exp(u)$. This composition can be obtained through the Baker-Campbell-Hausdorff approximation [44]: $\exp(v) \circ \exp(u) \approx \exp(v + u)$.

The exponential map can be efficiently computed as explained in [52]. By that, the exponential map of the velocity field v is approximated through the scaling and squaring method whose approximation starts by: $\exp(v) = (\exp(v/2^N))^{2^N}$. The idea of the approximation method is to choose N such that $v/2^N$ has a norm of order 1. The initial scaling takes place $s \leftarrow v/2^N$ and then the approximation is formed by N repeated squaring $s \leftarrow s \circ s$. Consequently, s is the approximated exponential of v. The computation of the exponential of the velocity field v is described in Algorithm 4. The velocity field and the transformation are then updated $v \leftarrow v + u$, $s \leftarrow \exp(v)$ in each iteration.

Lastly, the regularization is applied, first with a fluid like Gaussian filter (σ_{fluid}) on the intermediate update field (u), and second on the velocity field v with diffusion Gaussian kernel (σ_{diff}) as in Algorithm 3.

Input: $F, M, \text{maxiter}$
Output: $s \leftarrow \exp(v)$
Initialize: $v \leftarrow 0$, $i \leftarrow 0$
while $i < maxiter$ **do**
  $s \leftarrow \exp(v)$;
  $u \leftarrow -\frac{I_F - I_{M\circ s}}{||\nabla I_{M\circ s}||^2 + \frac{\alpha_x}{\alpha_i}|I_F - I_{M\circ s}|^2} \nabla I_{M\circ s}$;
  $u \leftarrow K_{\text{fluid}} \star u$;
  $v_c \leftarrow v + u$;
  $v \leftarrow K_{\text{diff}} \star v_c$;
  $i \leftarrow i + 1$;
end

Algorithm 3: Log-Demons

Input: Velocity field v
Output: $s \leftarrow \exp(v)$
Do:
Choose $N \in \mathbb{N} \mid 2^{-N} v \approx 0$
(e.g. if $\max_p ||2^{-N} v(p)|| \leq 0.5$, $N \leftarrow \max(\log_2(||v||))$;
$s(p) \leftarrow 2^{-N} v(p)$;
$i \leftarrow 0$;
while $i < N$ **do**
  $s \leftarrow s \circ s$;
  $i \leftarrow i + 1$;
end

Algorithm 4: Exponential $s = \exp(v)$. Scaling and Squaring method for computing exponential in the Lie group

The Log-Demons framework allows an inverse computation of the transformation $s^{-1} = \exp(-v)$. Therefore, a symmetric registration framework can be obtained, where the registration does not depend on the order of the input images. This was introduced in [122], such that: $s = \arg\min(E_{\text{Sim}}(F, M, s) + E_{\text{Sim}}(F, M, s^{-1}))$. This symmetric scheme splits the demons force search in each iteration into forward and backward correspondences by minimizing the direct and inverse energy $E_{\text{Sim}}(F, M, s)$ and $E_{\text{Sim}}(F, M, s^{-1})$ resulting in forward and backward update u_{fw} and u_{bw} for each iteration. The overall update field u is now the average u_{fw} and u_{bw} when mapping images from F to $M \circ \exp(s)$ and from M to $F \circ \exp(s^{-1})$. The optimization of the Log-Demons method is summarized in Algorithm 5.

Input: $F, M, \text{maxiter}$
Output: $s \leftarrow \exp(v)$
Initialize: $v \leftarrow 0$, $i \leftarrow 0$
while $i < maxiter$ **do**
  $s \leftarrow \exp(v)$, $(s^{-1} = \exp(-v))$;
  $u_{\text{fw}} \leftarrow -\frac{I_F - I_{M \circ s}}{||\nabla I_{M \circ s}||^2 + \frac{\alpha_x}{\alpha_i}|I_F - I_{M \circ s}|^2} \nabla I_{M \circ s}$;
  $u_{\text{bw}} \leftarrow -\frac{I_M - I_{F \circ s^{-1}}}{||\nabla I_{F \circ s^{-1}}||^2 + \frac{\alpha_x}{\alpha_i}|I_M - I_{F \circ s^{-1}}|^2} \nabla I_{F \circ s^{-1}}$;
  $u \leftarrow \frac{1}{2}(u_{\text{fw}} - u_{\text{bw}})$;
  $u \leftarrow K_{\text{fluid}} \star u$;
  $v_c \leftarrow v + u$;
  $v \leftarrow K_{\text{diff}} \star v_c$;
  $i \leftarrow i + 1$;
end

Algorithm 5: Symmetric Log-Demons

4.3.2 Spectral Demons

The previous image registration based on local iterative gradient is easy to get trapped into local minima. In the research of Lombaert *et al* [71], the authors alternate the step of searching for demon forces using Gauss-Newton optimization with a direct feature matching technique that combines intensity, spatial, and the

graph spectra as geometric constraints in registration. Let us briefly review this image registration technique and provide experiments on our biomedical images.

4.3.2.1 Matching with Intensity Information

Feature matching is a process of finding correspondence between fixed set $F = \{f_1, f_2, ..., f_P\}$ and moving set $M = \{m_1, m_2, ..., m_Q\}$ of feature points. Where each point f_p or m_q is a vector of features (i.e., HOG feature, spatial coordinates $f_p = (x_F(p), y_F(p))$, image intensity, shape feature). The goal of the matching is to find the deformation map s that minimizes the difference between the two sets in feature space, such that $s = \text{argmin}(\text{Sim}(F, M, s))$

$$\text{Sim}(F, M, s) = \sum_p ||f_p - m_{s(p)}||^2 \tag{4.21}$$

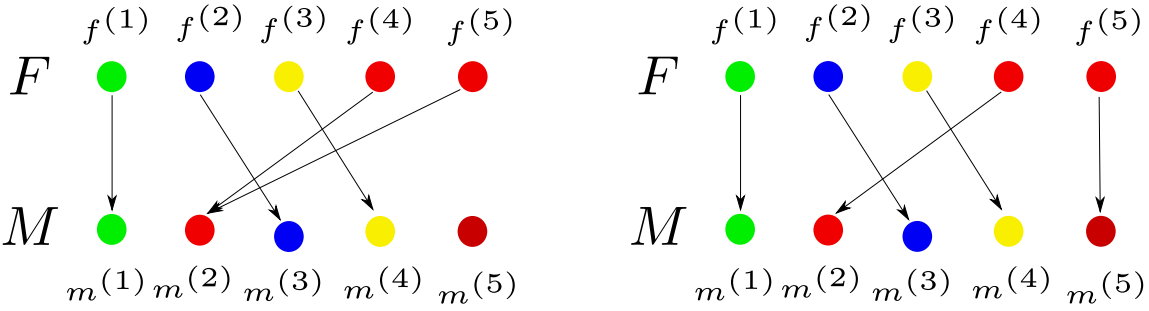

(a) Matching with intensity constraint without spatial constraint

(b) Matching with intensity and spatial constraint

Figure 4.3 – Feature matching

A direct feature matching method finds closest point in the moving set to each point in the fixed set, such that $s(p) = \text{argmin}_q||f_p - m_q||$. To prevent unsmooth transformation, the spatial coordinate of points is used in registration, apart from the intensity information. This is because different points at far apart positions can share similar intensity values. In this case, the registration lacks a spatial regularization and results in an unsmooth displacement field as illustrated on Figure 4.3a. Thus,

the optimization of intensity difference can be combined with a spatial regularity term to prevent the motion vectors from going too far. The objective function can be defined by:

$$\text{Sim}(F, M, s) = \alpha_i(I_F - I_{M \circ s})^2 + \alpha_s ||\mathbf{x}_F - \mathbf{x}_{M \circ s}||^2, \tag{4.22}$$

Where α_i controls the intensity similarity and α_s defines the level of smoothness of the deformation field. $\mathbf{x}_F = (x_F, y_F)$, $\mathbf{x}_M = (x_M, y_M)$ are the set of spatial coordinates of fixed image and moving image. Obviously, we can define the images in feature space that composes the intensity and spatial constraints with mathematical notations, such that for each point p in F and q in M we can define the feature vectors: $f_p = (\alpha_i I_F(p), \alpha_s x_F(p), \alpha_s y_F(p))$ and $m_q = (\alpha_i I_M(q), \alpha_s x_M(q), \alpha_s y_M(q))$. The direct matching finds the closest point q from the moving set $M$to p in F such that:

$$s(p) = \text{argmin}_q(\alpha_i(I_F(p) - I_M(q))^2 + \alpha_s ||\mathbf{x}_F(p) - \mathbf{x}_M(q)||^2), \tag{4.23}$$

In other word, if point $q \in M$ is closest to point $p \in F$ in term of intensity and spatial position, then $s(p) = q$.

4.3.2.2 Matching with Geometric Constraint

The optimization of Equation 4.22 lacks isometric invariance (neighboring points still preserve their relative distances after transformation). The question is, how to preserve object geometry when objects are in different poses? For the Demons and Log-Demons frameworks, different solutions to add a geometric constraint were proposed [69, 23, 106, 71]. For instance, [106] proposed to add a geometric constraint in the space of currents jointly with iconic registration. On the other hand, Lombaert *et al* [71] use additional graph spectral representation of shape as geometric constraint. The matching with geometric constraint finds correspondences between F and M where each point p^{th} in F and q^{th} in M are respectively defined as: $f_p = (\alpha_i I_F(p), \alpha_s x_F(p), \alpha_y y_F(p)), \alpha_g \mathcal{G}_F(p))$ and $m_q = (\alpha_i I_M(q), \alpha_s x_M(q), \alpha_s y_M(q), \alpha_g \mathcal{G}_M(q))$, where $\mathcal{G}_F$ and $\mathcal{G}_M$ account for the geometric constraints of the fixed and moving im-

ages.

The registration with geometric constraint walks toward the optimum of the following function:

$$\mathrm{Sim}(F, M, s) = \alpha_i(I_F - I_{M\circ s})^2 + \alpha_s||\mathbf{x}_F - \mathbf{x}_M \circ s||^2 + \alpha_g||\mathcal{G}_F - \mathcal{G}_{M\circ s}||^2, \quad (4.24)$$

The Spectral Log-Demons approach [71] considers the first k eigenvectors corresponding to the lower eigenvalues of the Laplacian matrix of the graph defined on each image as the spectral coordinates on behalf of the geometric constraint. Thus, the objective function of the Spectral Log-Demons method is denoted as follows:

$$\mathrm{Sim}(F, M, s) = \alpha_i(I_F - I_{M\circ s})^2 + \alpha_s||\mathbf{x}_F - \mathbf{x}_M \circ s||^2 + \alpha_g||\chi_F - \chi_{M\circ s}||^2, \quad (4.25)$$

where χ_F and χ_M stand for the spectral coordinates of the fixed and moving images. The demon forces in forward and backward mappings i.e. u_{fw} and u_{bw} are obtained by applying a direct point matching scheme instead of the gradient update in the classical Demons.

Input: $F, M, \text{maxiter}$
Output: $s \leftarrow \exp(v)$
Initialize: $v \leftarrow 0$, $i \leftarrow 0$
while $i < maxiter$ **do**
  $s \leftarrow \exp(v)$, $(s^{-1} = \exp(-v))$;
  Laplacian $L_{F \circ s^{-1}}, L_{M \circ s}$;
  $\chi_{F \circ s^{-1}} \leftarrow eigendecomposition(L_{F \circ s^{-1}})$;
  $\chi_{M \circ s} \leftarrow eigendecomposition(L_{M \circ s})$;
  u_{fw};
  u_{bw};
  $u \leftarrow \frac{1}{2}(u_{\text{fw}} - u_{\text{bw}})$;
  $u \leftarrow K_{\text{fluid}} \star u$;
  $v_c \leftarrow v + u$;
  $v \leftarrow K_{\text{diff}} \star v_c$;
  $i \leftarrow i + 1$;
end

Algorithm 6: Spectral Log-Demons

4.3.3 Application of the process to microscopic images

This work proposes experiments on randomly deformed microscopic images (Figure 4.4) and microendoscopic images (Figure 4.5) using Spectral Demons method. These experiments are exploited to evaluate the performance of this algorithm on Biomedical images.

In Figure 4.4, a microscope image is randomly deformed and then the deformed image is registered toward the original image. The spectral, spatial and intensity weights are respectively $\alpha_g = 1, \alpha_s = 4, \alpha_i = 20$. The fixed and moving images are respectively shown on Figure 4.4a and Figure 4.4b. The best restored image in term of MSE value is chosen after 50 iterations and is depicted on Figure 4.4c. The MSE value with respect to the number of iterations is illustrated on Figure 4.4d. As it is obvious on the Figure 4.4d, the energy value does not monotonically increase or decrease but fluctuates when the number of iteration increases, and the best solution is obtained at the iteration of 45. This phenomenon is not a surprise because it was somewhat proved in the original article [70] that the algorithm starts to fail when

much noise occurs, and the images used in this experiment are noisy by their nature.

In Figure 4.5, we register 4 random pairs of images in the microendoscope image sequence. Although the energy values seem to converge fast at the early iterations and remain unchanged when it gets to the lowest value, the restored images suffer from smoothing effect, especially in the 3rd and the 4th cases. This phenomenon happens because of the changes in illumination of the images.

In both cases, the Spectral Demons algorithm does not properly converge. This is due to the complex texture of the images , and changes in brightness of microendoscope images. Next, the interaction of the graph spectrum in the registration using the well-known interpolation model method called Bspline approach is examined.

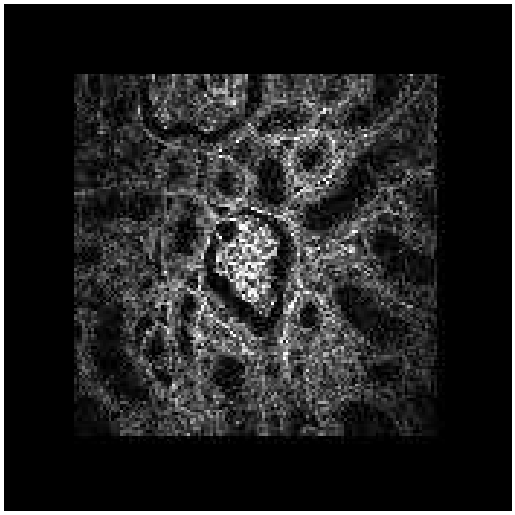

(a) Fixed image

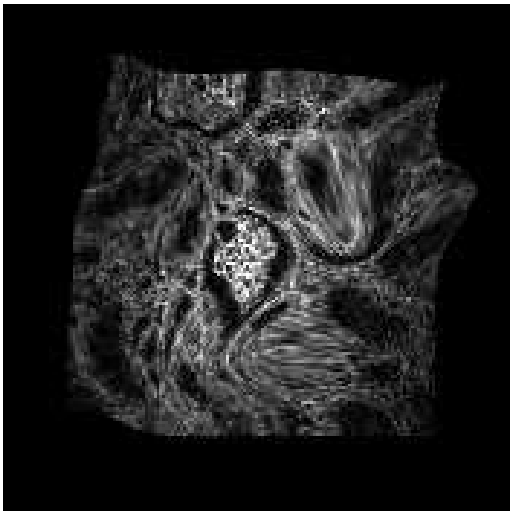

(b) Moving image

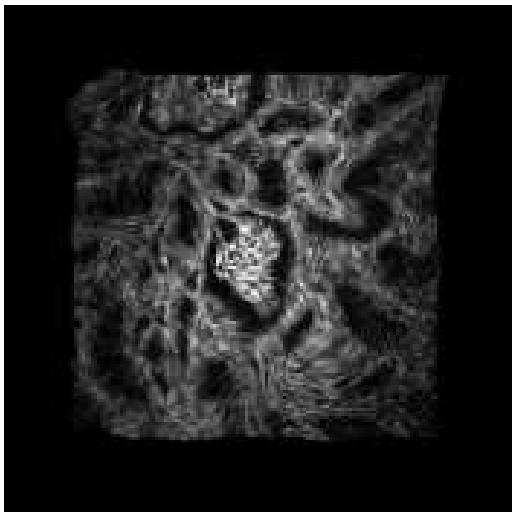

(c) Spectral Demons

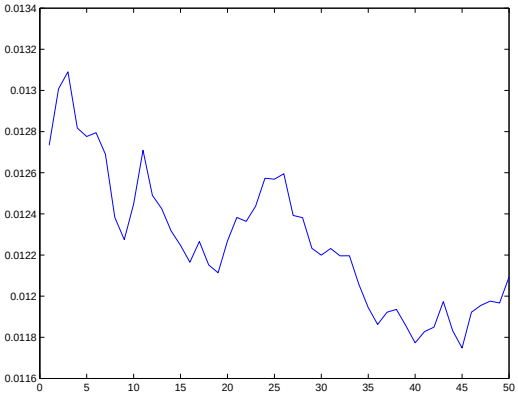

(d) MSE with respect to iteration

Figure 4.4 – Spectral Demons method on Microscopic images, ew = 1, sw = 4, iw = 20

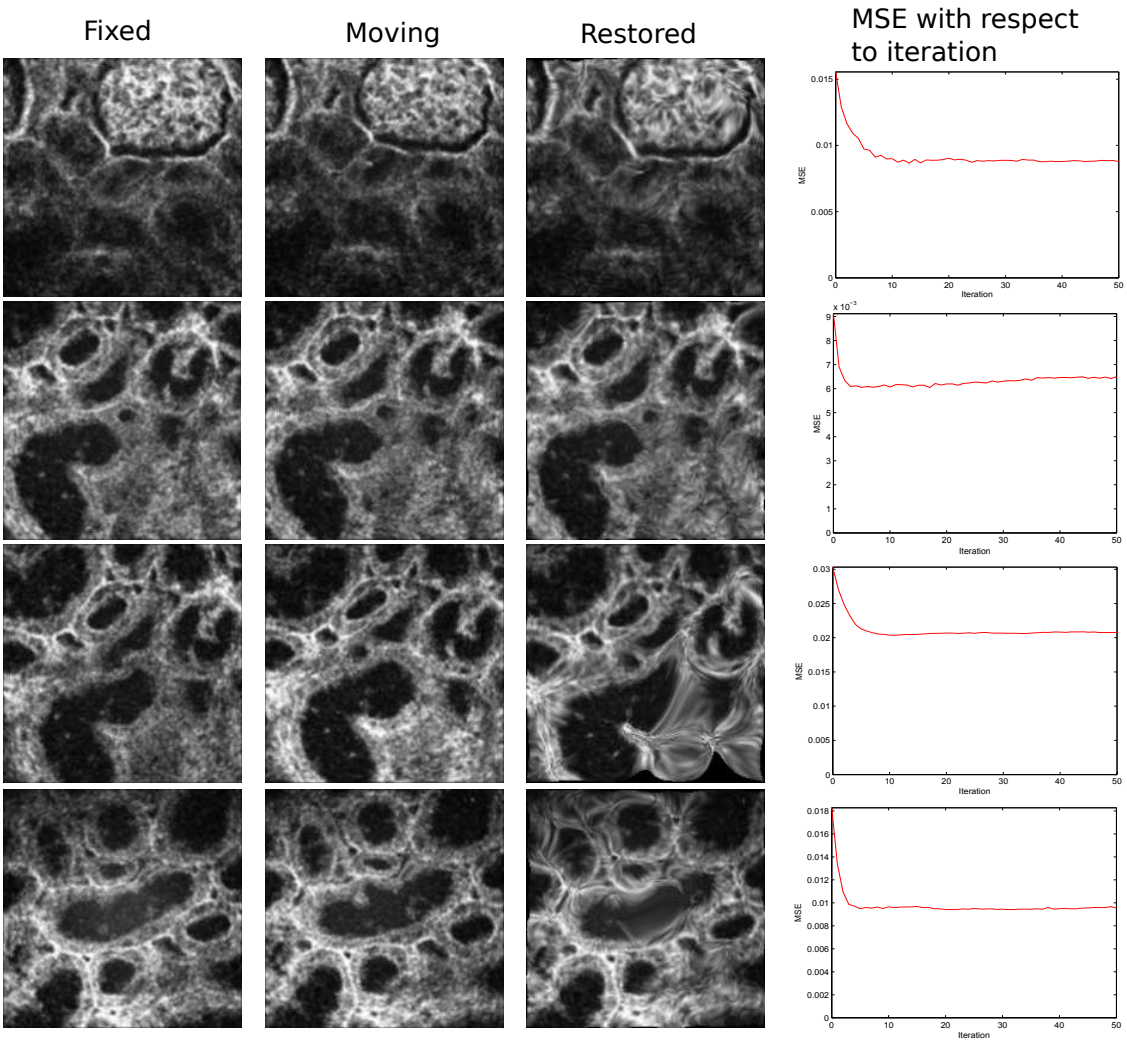

Figure 4.5 – Spectral Demons method on microendoscopic images

4.4 Spectral Bspline

Apart from the Demons approach, a very well known registration model in the medical imaging field is the B-spline approach. This model has advantages of producing smooth transformation and the transformation has better physical fidelity than the Demons model [59]. This section describes a registration based on the B-spline method introduced in [96] with an additional graph spectral constraint. The classical Bspline registration method is first described before the registration with spectral constraint is presented.

4.4.1 Bspline Registration

Bspline registration is inspired by Bspline warping techniques, in which an image is derived by a grid of control points and a predefined piecewise Bspline polynomial. To describe the Bspline algorithm, we denote: $\Omega = \{(x, y)|0 \leq x < m, 0 \leq y < n\}$ as the domain of an image of size $m \times n$. A set of control points is denoted on a mesh ϕ of size $n_x \times n_y$, overlaid on space Ω with uniform spacing. Let $\phi_{i,j}$ be the value of the ij^{th} control point. The transformation model function can be written as the tensor product between cubic Bsplines and the control points.

$$\mathcal{T}_\phi(x, y) = \sum_{l=0}^{3} \sum_{p=0}^{3} B_l(t_u) B_p(t_v) \phi_{i+l,j+p}, \tag{4.26}$$

where $i = \left\lfloor \frac{x}{n_x} \right\rfloor - 1$, $j = \left\lfloor \frac{y}{n_y} \right\rfloor - 1$, $t_u = \frac{x}{n_x} - \left\lfloor \frac{x}{n_x} \right\rfloor$, $t_v = \frac{y}{n_y} - \left\lfloor \frac{y}{n_y} \right\rfloor$, and B_l, B_p are uniform cubic Bspline functions defined as:

$$\begin{cases} B_0(t_u) = (1 - t_u)^3/6, & \text{(4.27a)} \\ B_1(t_u) = (3{t_u}^3 - 6{t_u}^2 + 4)/6, & \text{(4.27b)} \\ B_2(t_u) = (-3{t_u}^3 + 3{t_u}^2 + 3t_u + 1)/6, & \text{(4.27c)} \\ B_3(t_u) = {t_u}^3/6 & \text{(4.27d)} \end{cases}$$

with $0 \leq t_u < 1$.
The cubic Bspline function contributes to weighting each control point to the computation of transformation based on its distance to the center point (x, y). The registration problem becomes the problem of finding the best set of control points that minimizes the similarity between images. Bspline registration minimizes the similarity between two images by iteratively updating the grid of control points with subject to every point as a parameter, and deform the moving image M with it until the minimal similarity is reached. The similarity measurement is given as:

$$\text{Sim}(F, M, \phi) = [I_{M \circ \mathcal{T}_\phi(x)} - I_F]^2, \tag{4.28}$$

where F, M are respectively fixed and moving images. $\mathcal{T}_\phi(x)$ is the transformation function of control points.

4.4.1.1 Optimization

To optimize Equation 4.28 with respect to the grid of control points ϕ, ϕ is assumed to be known in the current estimation. It is then iteratively incremented by $\Delta\phi$ such that the value of the objective function at $\phi + \Delta\phi$ decreases. In other word, the optimization iteratively finds $\phi \leftarrow \phi + \Delta\phi$ such that this function is minimized:

$$|I_{M \circ \mathcal{T}_{\phi + \Delta\phi}(x))} - I_F|^2. \tag{4.29}$$

The optimization process is operated in several steps using a line search optimization i.e. to find a descent direction along which the objective function will reduce. The general optimization process to minimize a given function $f(\phi)$ with respect to ϕ is described in Algorithm 7.

Different methods were proposed to find the descent direction. The Quasi-Newton method is a non-linear optimization method triggered by a second order Taylor approximation , where the update of ϕ is given by:

$$\phi_{k+1} \leftarrow \phi_k - [H(\phi_k)]^{-1} \nabla f(\phi_k), \tag{4.30}$$

Input: $f(\phi)$
Output: ϕ
Initialize: $\phi \leftarrow \phi_0$, $k \leftarrow 0$
while $\Delta\phi < \tau$ **do**
  Compute $\Delta\phi | f(\phi_k + \Delta\phi) < f(\phi_k)$;
  $\phi_{k+1} \leftarrow \phi_k + \Delta\phi$;
  $k++$;
end

Algorithm 7: General optimization

where $H(\phi_k)$ represents the Hessian matrix of the objective function $f(\phi)$. When the number of variables is large, the computation of the Hessian matrix and its inverse becomes complicated and expensive. The computation of the Hessian matrix is replaced by the Quasi-Newton method by applying an approximation to the inverse of the Hessian: $B_k = [H(\phi_k)]^{-1}$ in combination with an inexact line search (such as Wolfe conditions [130]) to find the direction α_k in each iteration. The methods in the Quasi-Newton class differ in the way they approximate the Hessian matrix and its inverse. The general description of Quasi-Newton method is presented in Algorithm 8.

Input: $f(\phi)$
Output: ϕ
Initialize: $\phi \leftarrow \phi_0$, $k \leftarrow 0$
while $\Delta\phi < \tau$ **do**
  $\alpha_k \leftarrow \text{LineSearch}(\phi_k, f)$;
  $B_k \leftarrow [H(\phi_k)]^{-1}$ (diverges);
  $\phi_{k+1} \leftarrow \phi_k - \alpha_k B_k \nabla f(\phi_k)$;
  $k++$;
end

Algorithm 8: Quasi-Newton optimization

Among the class of Quasi-Newton methods, the Broyden–Fletcher–Goldfarb–Shanno (BFGS) is one of the most efficient and is thus one of the most popular methods [63]. It is indeed an iterative method that seeks stationary point of a function by ap-

proximating the Hessian matrix in each iteration, and the current Hessian update is propagated to the next approximation. When the number of variables becomes extensively large, such as in case of Bspline registration for 2D images, the control points are set on a 2D grid, the updating and storing of the Hessian matrix and its inverse become much more computationally expensive. The so-called Limited-memory BFGS (LBFGS) method [84] is a variant of the BFGS method that eliminates the need for storing the Hessian matrix and its inverse matrix in memory.

4.4.1.2 Registration

The Bspline image registration using Quasi-Newton optimizer is described as in Algorithm 9. It starts with the fixed and moving images, and an initialization of a grid of control points as the input. The registration problem walks toward the minimization of the objective function Equation 4.28. In each iteration, the transformation field $\mathcal{T}_\phi$ is updated as described previously in Equation 4.26. And then the moving image is updated according to the current transformation field. Once the moving image is updated, the new value of the objective function is therefore computed, and thus, the new variable is updated in the current iteration.

Input: $F, M, maxiter$
Output: ϕ
Initialize: $\phi \leftarrow \phi_0$, $k \leftarrow 0$
while $k < maxiter$ **do**
  $\mathcal{T}_\phi \leftarrow \sum_{l=0}^{3}\sum_{p=0}^{3} B_l(t_u)B_p(t_v)\phi_{i+l,j+p}$;
  $M \leftarrow M \circ \mathcal{T}_\phi$;
  $\alpha_k \leftarrow \text{LineSearch}(\phi_k, \text{Sim}(F, M, \phi))$;
  Approximate $B_k = [H(\phi_k)]^{-1}$;
  $\phi_{k+1} \leftarrow \phi_k - \alpha_k B_k \nabla f(\phi_k)$;
  $k \leftarrow k + 1$;
end

Algorithm 9: Bspline Registration

4.4.2 Spectral Bspline Image Registration

As in classical Bspline image registration formulated in Equation 4.28, the optimization lacks geometric constraint. Motivated by the idea that the graph spectrum can be used for registration, this work proposes to add an additional spectral constraint to the optimization, such that, the graph spectrum characterizes the geometric feature of the images. The registration that involves spectral constraint optimizes the following objective function:

$$\text{Sim}(F, M, \phi) = [I_{M \circ \mathcal{T}_\phi(x)} - I_F]^2 + \lambda_g [\chi_{M \circ \mathcal{T}_\phi(x)} - \chi_F]^2 \tag{4.31}$$

where λ_g isthe spectral weight, χ_F and $\chi_{M \circ \phi}$ are the graph spectral constraints of the fixed image and the moving image. Equation 4.31 can be minimized by using an optimization algorithm that iteratively updates the variables towards the minimum such as Gradient Descent, Quasi-Newton, or LBFGS method as described previously. For low cost, not having to compute the Hessian matrix of a large number of variables, and more stable optimization, this work uses LBFGS algorithm.

The optimization takes an initial grid of control points ϕ_{init}, the fixed and moving images as inputs. The output is the transformation $\mathcal{T}$ from F to M. In each iteration of registration, the transformation field $\mathcal{T}$ is updated with respect to the updated control points ϕ as in Equation 4.26. The moving image M is then updated according to the current transformation field. After that, the graph spectrum are computed for the moving image as described in section 4.2. Notice that, only the moving image is deformed at each iteration. Thus, we compute the spectra of the fixed image once at initial stage, while the spectrum of the moving image is updated as the moving image is deformed. The update step of control points $\Delta\phi$ is then found by performing LBFGS optimization algorithm to minimize Equation 4.31. The optimization is summarized in Algorithm 10.

Input: $F, M,$ maxiter
Output: ϕ
Initialize: $\phi \leftarrow \phi_0$, $k \leftarrow 0$
Laplacian L_F;
$\chi_F \leftarrow eigendecomposition(L_F)$;
while $i < maxiter$ **do**
  $\mathcal{T}_\phi(x, y) \leftarrow \sum_{l=0}^{3}\sum_{p=0}^{3} B_l(t_u)B_p(t_v)\phi_{i+l,j+p}$;
  $M \leftarrow M \circ \mathcal{T}_\phi(x, y)$;
  Compute Laplacian L_M;
  $\chi_M \leftarrow eigendecomposition(L_M)$;
  $\alpha_k \leftarrow \text{LineSearch}(\phi_k, \text{Sim}(F, M, \phi))$;
  $B_k \leftarrow [H(\phi_k)]^{-1}$;
  $\phi_{k+1} \leftarrow \phi_k - \alpha_k B_k \nabla f(\phi_k)$;
  $k \leftarrow k + 1$;
end

Algorithm 10: Spectral Bspline

4.4.3 Results

This section evaluates the performance of the Spectral Bspline registration method and compares it with the classical Bspline registration method on biomedical images with random deformations. Registration is performed on two pairs of images. The first pair is of the original, while Gaussian noise is added to the second pair, in order to observe how these methods operate with noise.

The graph representation of each image is constructed using eight neighbor connectivity over each point. The weight of the edge that connects vertex i and vertex j is denoted as:

$$w_{ij} = \begin{cases} \exp\left(-\frac{(I_i - I_j)^2}{||\mathbf{x}_i - \mathbf{x}_j||^2}\right) & \text{if}(i,j) \in \mathcal{E}, \\ 0 & \text{otherwise.} \end{cases} \tag{4.32}$$

Once the graph topology and graph weights are defined, the graph Laplacian can be computed according to section 4.2. And thus, the optimization is operated according to Algorithm 10. The experiment is tested on biomedical images of size 64 by 64

with a random deformation.

In order to observe the interaction of noise on the registration, a random Gaussian noise (standard deviation $\sigma_{noise} = 0.01$) was added to the original images. Table 4.1 depicts the MSE of the fixed image and the registered image after Bspline and Spectral Bspline registrations.

As shown in the table, in the non-noisy case, Spectral Bspline algorithm performs better than the Bspline algorithm when the spectral weight is $\lambda_g \leq 0.1$. The Spectral Bspline methods get the best registration at $\lambda_g = 0.05$, with $MSE = 1.935 \times 10^{-3}$.

In the noisy case, a more significant improvement between Spectral Bspline and Bspline algorithm is observed. In more details, Spectral Bspline algorithm gives better results when the value of spectral weight is $\lambda_s \leq 0.2$, and the best registration of Spectral Bspline method falls at $MSE = 17.09 \times 10^{-3}$ when $\lambda_g = 0.05$. When the value of λ_g is greater than 0.5, the performance of Spectral Bspline becomes worse than classical Bspline algorithm. This implies that the spectral weight should not be too large, and the intensity information plays a more important role than the spectral information.

	Original images						Images with Gaussian noise added					
λ_g	0.01	0.02	0.05	0.1	0.2	0.5	0.01	0.02	0.05	0.1	0.2	0.5
Spectral Bspline ($\times 10^{-3}$)	1.987	1.991	1.935	1.989	2.064	2.006	18.01	18.02	17.09	17.55	17.37	23.47
Bspline ($\times 10^{-3}$)	2.014						18.06					

Table 4.1 – Mean Square Error (MSE) between the fixed image and restored image of Bspline and Spectral Bspline methods.

Figure 4.6 graphically presents registration results of the two mentioned methods. Figure 4.6d and 4.6f respectively demonstrate the absolute difference between fixed image and restored image of Bspline and Spectral Bspline techniques. We can see that there is less error at the region covered by the green rectangle of the result obtained by Spectral Bspline algorithm (see Figure 4.6d, 4.6f). However, the improvement of the Spectral Bspline method is minor compared to the Bspline method. The convergences of the Bspline and Spectral Bspline registration depend on the number of control points initialization of the control points. It is observed that the L-BFGS

optimization method is faster and less memory cost that can perform well in the classical Bspline registration method. However, it is still memory limited and takes a long time to execute the Spectral Bspline method, but gain minor improvement. This is because the line search step has to compute the graph in each iteration and each Hessian approximation. In contrast, a Demons based approach with an intermediate gradient update is faster to execute than the Bspline approach, thus, more appropriate with a graph based application. We now introduce our contribution that is based on the Demons framework and outperforms the existing graph based Spectral Demons method in term of noise.

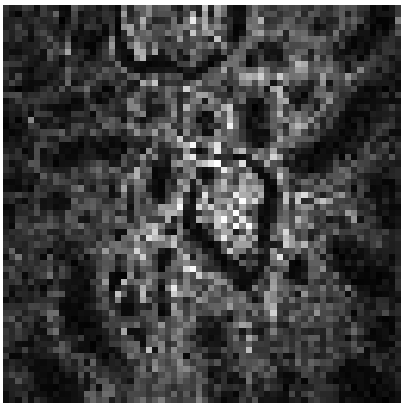

(a) Fixed image

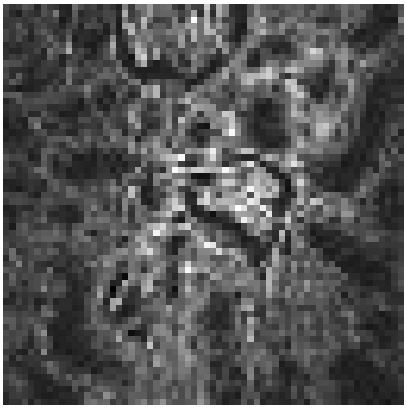

(b) Moving image

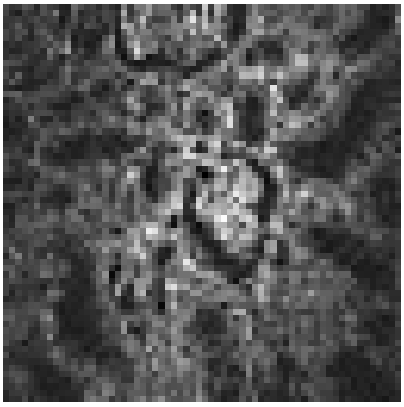

(c) Image restored by Bspline

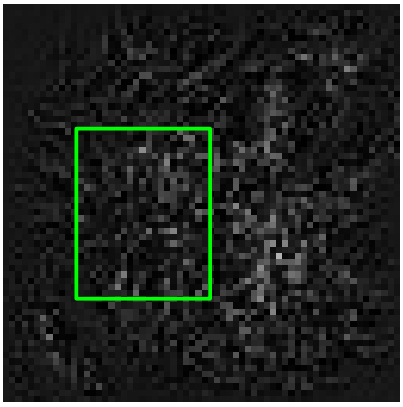

(d) Absolute Error by Bspline

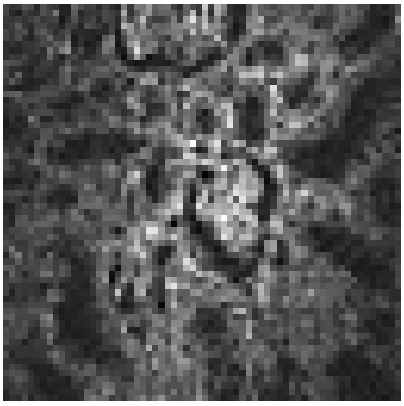

(e) Image restored by Spectral Bspline

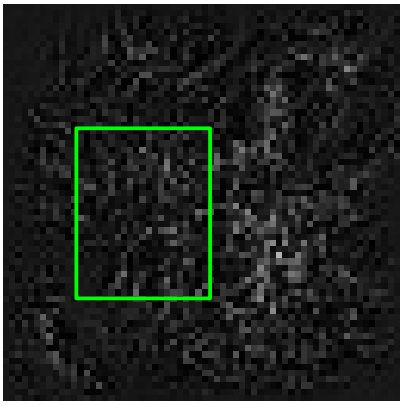

(f) Absolute Error by Spectral Bspline

Figure 4.6 – Comparison between Bspline registration and Spectral Bspline registration of microscopic images

4.5 Spectral Graph Wavelet (SGW) based Image Registration

So far in this chapter, the registrations on biomedical images with spectral constraint under two well-known registration frameworks: Demons and Bspline have been described. The spectral constraint is geometric invariant, however it is limited with noisy images. Next, a novel registration method that uses the Spectral Graph Wavelet decomposition to capture the shape feature of the images (Figure 4.7) is presented. The Spectral Graph Wavelets decomposition defined in the graph spectral domain was introduced by Hammond et al [48]. It allows us to utilize the benefits of the image representation on graphs and have the similar advantages to the classical wavelet domain. And the motion estimation is cast into a feature matching problem under the Log-Demons framework. This work was published in the conference **ICIP** *(International Conference on Image Processing)* held in Athens, Greece, in October 2018.

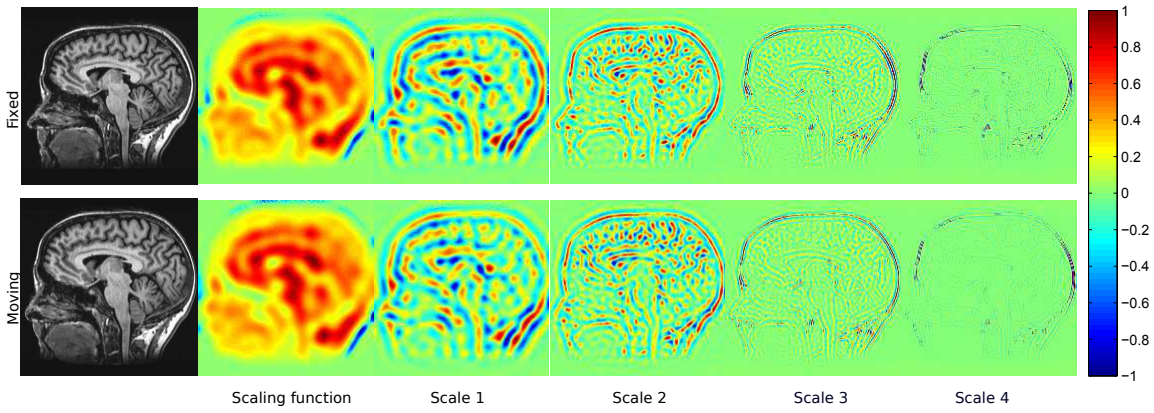

Figure 4.7 – The spectral graph wavelet coefficients at different scales of two brain images.

4.5.1 Objective function

At this stage, the graph representation and construction have been briefly introduced. In addition, the Spectral Graph Wavelet decomposition as well as the Bspline and Demons registration methods are described. However, the registration using Bspline is computationally expensive due to the gradient search. This is especially the case when graph computation is applied in each line search iteration, while the Demons method is more simple to execute. In addition, the convergence of the Bspline method also depends on the choice of the number of control points and the control point initialization that is sometimes difficult to predict. On the other hand, classical intensity based methods are limited to the local scope and lacks geometric invariance. A spectral approach that is geometric invariant is well known to adapt to non-local deformations. Such complementary approaches motivate a hybrid method that combines intensity and geometric information. Spectral Graph Wavelet approach is a multiscale graph based technique, that is defined in graph spectral Fourier domain. Therefore, Spectral Graph Wavelets are not only geometric invariant but also allow us to analyze graph data in different frequency bands. In this section, we provide our objective function that contains Spectral Graph Wavelet constraint for geometric invariance. Suppose we analyze Spectral Graph Wavelets of each image at t scales, the constructed Graph Wavelets are then composed of $t+1$ components, where the first component is the coarse approximation, and the rest are the Spectral Graph Wavelets coefficients at scales $1, \ldots, t$. The first k components at lower bands (with $k < t$) are chosen for use in registration and they are denoted as W_F and W_M for the fixed and moving images. The choices of t and k depend on the image characteristics and t defines the levels of details that we want to use. The specifications of the generating kernel function g and the scaling function h in [48] are exploited.

Once the Spectral Graph Wavelet coefficients are computed, they are embedded as the SGW coordinates of the feature sets built for each images: $F = (\alpha_i I_F, \alpha_s \mathbf{x}_F, \alpha_g W_F)$ and $M = (\alpha_i I_M, \alpha_s \mathbf{x}_M, \alpha_g W_M)$. The optimization is cast into a feature matching by applying a nearest neighbor search (e.g, k-d tree). The optimization walks towards the minimum of the following objective function:

$$E(F, M, s) = \alpha_i ||I_F - I_{M \circ s}||^2 + \alpha_s ||\mathbf{x}_F - \mathbf{x}_{M \circ s}||^2 + \alpha_w ||W_F - W_{M \circ s}||^2, \tag{4.33}$$

where $\alpha_i, \alpha_s,$ and α_w are respectively the intensity, regularization, and spectral wavelet weights.

The optimization is an iterative scheme that is a trade-off between the minimization correspondence search and a regularization of the motion field. In each iteration, the transformation field is achieved by performing optimization on Lie algebra through an exponential map of the stationary velocity v according to [119]. Spectral Graph Wavelets are computed for both updated images. The update fields u_{fw} and u_{bw} are found in both forward (F to $M \circ s$) and backward (M to $F \circ s^{-1}$) matching. To do that, the auxiliary variable c is introduced, it plays the role of the intermediate correspondence in the current iteration.

For instance, if c is the correspondence from F to M, c is found such that, for each point p in F in correspondence with point q in M, we have $F(p) = M(q)$, and thus $c(p) = q$.

$$c(p) = \text{argmin}_q(\alpha_i ||I_{F(p)} - I_{M(q)}||^2 + \alpha_s ||\mathbf{x}_{F(p)} - \mathbf{x}_{M(q)}||^2 + \alpha_w ||W_{F(p)} - W_{M(q)}||^2) \tag{4.34}$$

This correspondence mapping can efficiently done by a nearest neighbor search (e.g. k-d tree). Consequently, the value of update field u at p is denoted as:

$$u(p) = \mathrm{x}_{M(c(p))} - \mathrm{x}_{F(p)} \tag{4.35}$$

The symmetric update field u is the average of u_{fw} and $-u_{bw}$: $u = \frac{1}{2}(u_{fw} - u_{bw})$. The next step is to smooth the update field u with a Gaussian kernel K_{fluid} with standard deviation σ_{fluid}. The velocity field v is updated by the computed update field, and then smoothed with a Gaussian kernel K_{diff} with σ_{diff}. The registration process can be summarized in Algorithm 11.

Input: Fixed and moving images: F, M
Output: Transformation field $s = \exp(v)$
Initialize: Velocity field v
while $i < maxiter$ **do**
  $s = \exp(v)$;
  $W_{F \circ s^{-1}} \leftarrow computeSGW(F \circ s^{-1})$;
  $W_{M \circ s} \leftarrow computeSGW(M \circ s)$;
  $c_{F \to M \circ s}$;
  u_{fw};
  $c_{M \to F \circ s^{-1}}$;
  u_{bw};
  $u \leftarrow \frac{1}{2} K_{\text{fluid}} * (u_{fw} - u_{bw})$;
  $v \leftarrow \log(\exp(v) \circ \exp(u))$;
  $v \leftarrow K_{\text{diff}} * v$;
end

Algorithm 11: SGW Demons Registration

4.5.2 Results

Here, the proposed method is benchmarked against two existing algorithms (i.e. *Log-Demons* and *Spectral Log-Demons*) on classical images and medical images. An eight neighbor graph connectivity is utilized in all of the experiments. In the computation of the edge weights as described in Session 4.2, a large value of K ($K = 30$) is chosen to have an application that is less sensitive to noise. This in turn has less influence of intensity difference on the computation of edge weight (Equation 5.3).

4.5.2.1 Experiments on Lena images

In the experiments on Lena images, we evaluate the difference between the performance of our method and the existing methods *Log-Demons* and *Spectral Log-Demons*. The moving image is obtained by randomly deforming the fixed image as shown in Figure 4.8. Noticeably, the deformations are placed at most of the regions of the image but the highest level of deformations are seen at the front hat region and the neck. The algorithms use the same weighting parameters ($\alpha_i = 20, \alpha_s = 4, \alpha_g = 1$). In the Spectral Demons algorithm, two eigenmodes are used while in our algorithm,

we use three first components ($k = 3$) from four scales of Spectral Graph Wavelet decomposition ($t = 4$).

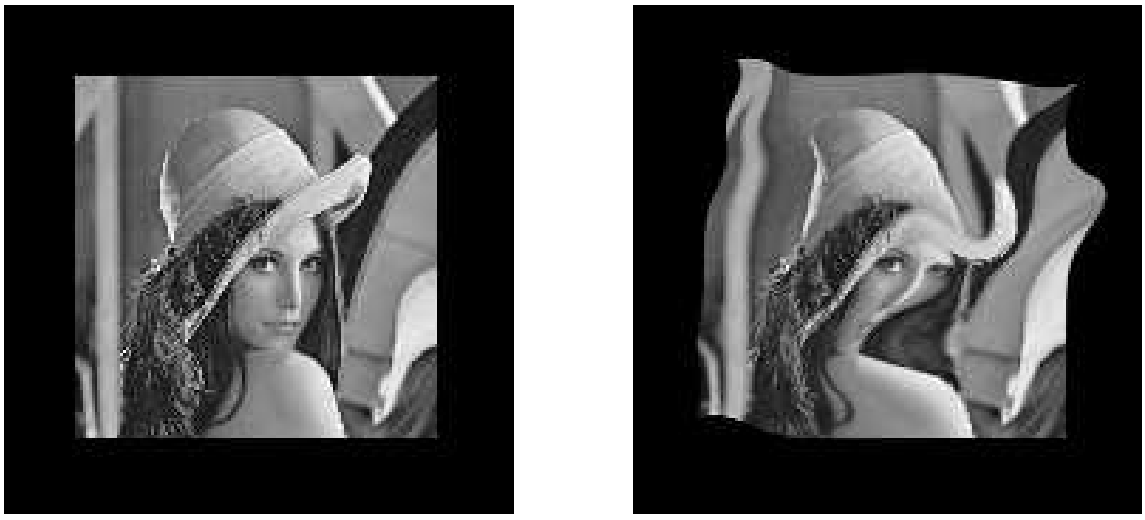

(a) Fixed image (b) Moving image

Figure 4.8 – Lena image with a random deformed image used in this experiment

σ_{noise}	Log-Demons	Spectral Log-Demons	SGW Demons
0	0.0143	0.0039	0.0029
0.01	0.0232	0.0175	0.0107
0.02	0.0291	0.0239	0.0170
0.05	0.0441	0.0406	0.0344
0.07	0.0510	0.0507	0.0445
0.1	0.0602	0.0654	0.0569

Table 4.2 – MSE between the restored image and the fixed image

The focus here is more on the robustness to noise of the algorithms rather than the robustness to the amount of deformations. To evaluate the performance of the methods when noise exists, Gaussian noise with different values of standard deviation ($\sigma_{\text{noise}} \in [0, 0.2]$) is added to the images. The registration of the images with increasing Gaussian noise are presented in Figure 4.10 after 50 iterations,

where each row presents the registration results of the three methods on images with Gaussian noise added, the standard deviation values of Gaussian noise are $\sigma_{\text{noise}} = 0, 0.01, 0.02, 0.05, 0.07$ respectively. The first three columns of Figure 4.10 present the restored images associated with the best iterations (smallest MSE) of the Log-Demons method, the Spectral-Log Demons method, and our method respectively.

To be more objective and statistical, the iterations of the three methods are shown numerically on the fourth column, where the MSE values between the registered image of each method and the fixed image with respect to the number of iteration are compared with each other. It shows that, when there is no noise, the performance of the Spectral Log-Demons method and our method are similar (our method has a slight improvement compared to the Spectral Log-Demons method). The neck and front hat regions are well registered. In contrast, the Log-Demons method does not capture the large deformations due to the slow convergence of the Gradient update. However, when noise exists, the performance of the Spectral Log-Demons method starts to fall while our method still keeps its advantages. For example, when $\sigma_{\text{noise}} = 0.01$, the larger and more complex deformed regions do not move closer to the exact positions although the MSE values still show its convergence.

To have a better view of how each method is robust to noise, the evolution of MSE of each method with respect to noise is demonstrated in Figure 4.9, In addition, Table 4.2 gives some examples of the exact MSE values between the restored and the fixed images. In all of the optimization, the registration chooses the best transformation corresponding to the minimum MSE. When the noise increases ($\sigma_{\text{noise}} > 0.075$), the MSE value of Spectral Log-Demons registration is larger than the Log-Demons method, while our method still keeps its advantages until σ_{noise} increases to 0.17. When $\sigma_{\text{noise}} > 0.17$, our method gains larger MSE value than the Log-Demons method. After all, our method is more robust than the Spectral Log-Demons method in all of the tested cases on Lena image.

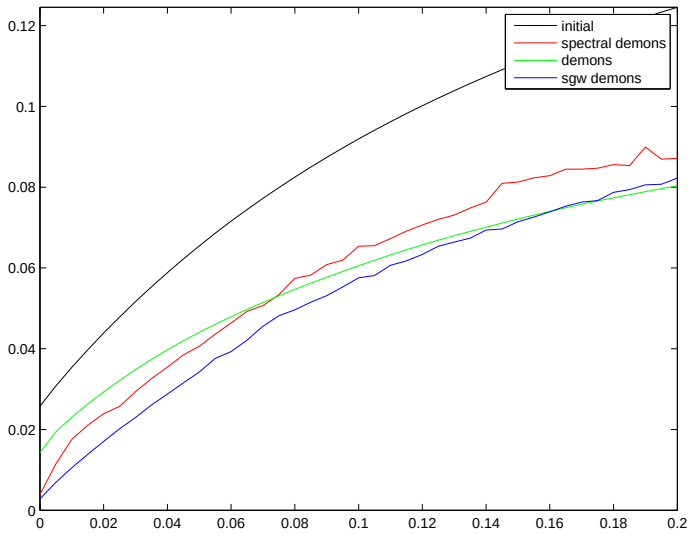

Figure 4.9 – Mean Square Error (MSE) with respect to Gaussian noise, registration of Lena image

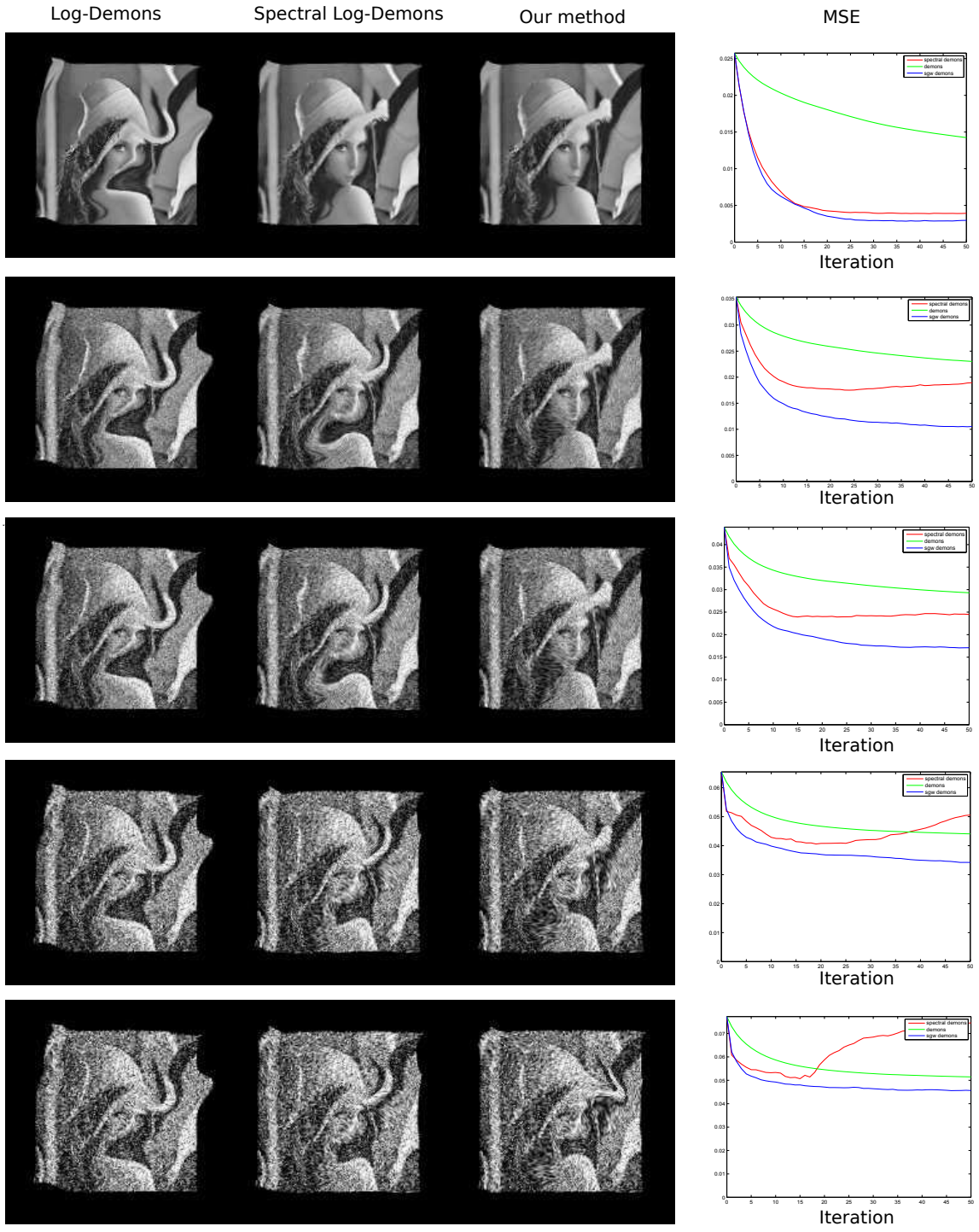

Figure 4.10 – Registration of Lena images with random deformations and increasing Gaussian noise added.

4.5.2.2 Experiments on medical images

We now evaluate the registration of T1 brain images and endomicroscopic images. The performance of our method and the benchmarks (Log-Demons and Spectral Log-Demons)is evaluated on medical images with the registration of a pair of the T1 brain images and a pair of randomly deformed microendoscopic images, shown in Figure 4.11. The first and second columns of images respectively present the fixed and moving images and the third column graphically shows the absolute error of the fixed and moving images. We use the same set of weighting parameters ($\alpha_i = 20, \alpha_s = 4, \alpha_g = 1$. α_g is the spectral weight of Spectral Log-Demons, and SGW weight in our method). We use $t = 4$ number of scales for SGW computation and choose $k = 3$ first components of SGW (including the scaling function component) for our method, and $k = 2$ eigenmodes for Spectral Log-Demons method.

Figure 4.12 shows the comparison between the output of the proposed algorithm and the outputs of the existing solutions. The first and second rows of Figure 4.12 show the registration results of two T1 brain images. In the first row from left to right are the registered images of the Log-Demons, Spectral Log-Demons and the proposed method respectively. The second row displays the corresponding graphical Absolute Difference of the methods. The top right figure in Figure 4.12 shows the comparison in terms of Mean Square Error (MSE) with respect to the number of iterations of all algorithms. Similarly, the third and fourth rows show the registration results of image microendoscope images. The fixed image is cropped from the center region of an microendoscope image. The moving image is generated by performing a random bspline transform on the fixed image. The bottom right figure shows the MSE curves of the methods with respect to the number of iterations of the registration of microendoscope images.

As can be seen in Figure 4.12, the methods with a geometric constraint (Spectral Log-Demons method and the proposed method) move faster to the convergence of the registration. However, in the registration of T1 images and at further iterations, the MSE of the Log-Demons method decreases and gets close to the MSE value of the Spectral Log-Demons method. The proposed method moves fast to the minimum

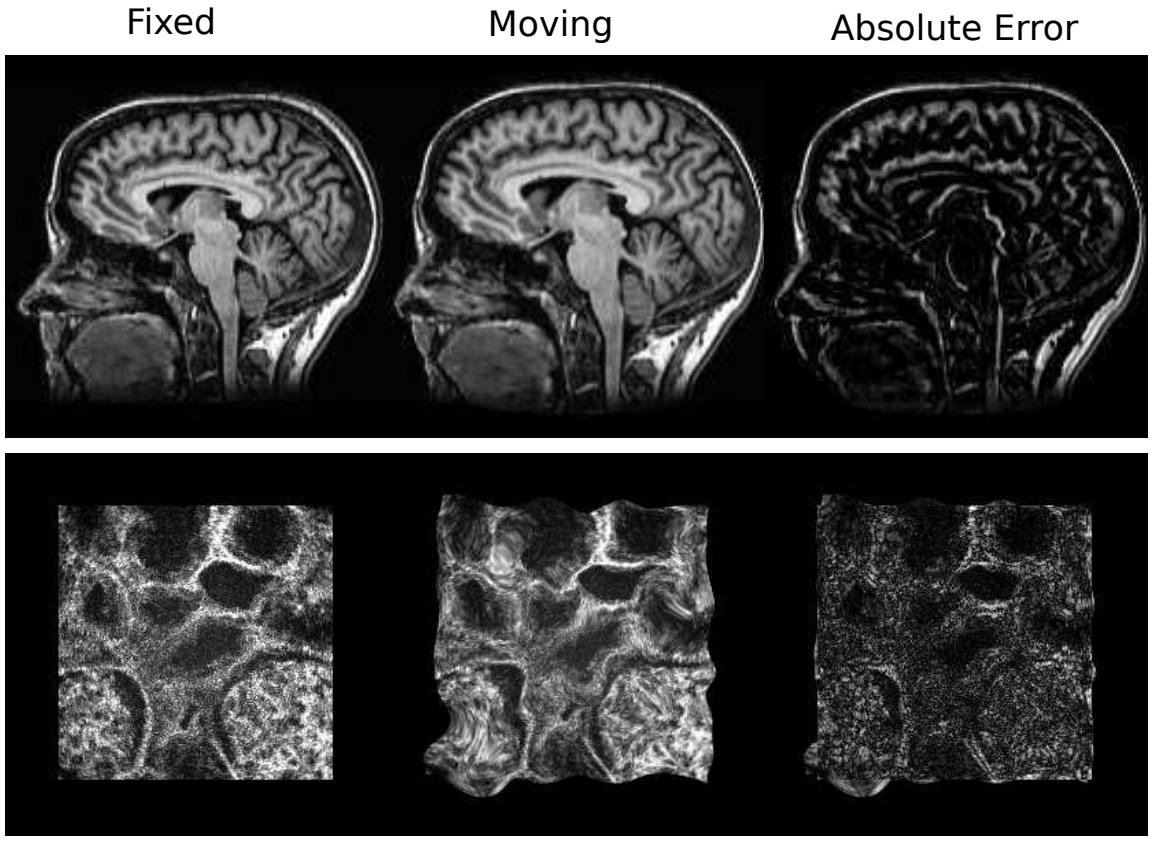

Figure 4.11 – Pairs of T1 brain images and endomicroscopic images are used in this experiment

energy (at the 5th iteration in the registration of T1 brain images and at the 17th in registration of microendoscope images) and remains unchanged at the later iterations. In both cases, the proposed method outperforms the benchmarking methods in term of both visualization and energy measurement.

In order to show the robustness to noise of the registration methods of medical images, a Gaussian noise is added to the fixed and moving images with standard deviation σ_{noise} ranging from 0 to 0.1 to the T1 brain images. The MSE value of the algorithms with respect to noise is shown in Figure 4.13. To see more clearly, the fixed (in red channel) and registered (in green channel) images of the algorithms are blended in a RGB image when $\sigma_{\text{noise}} = 0.014$. The significant misalignment

of Log-Demons and Spectral Log-Demons is shown in the cropped regions (in the blue rectangle at the forehead region, and in the yellow rectangle close to the back neck region). And the Log-Demons method shows more misalignment on the entire image. It is observed in the MSE graph that the performance of the Spectral Log-Demons method fluctuates unpredictably with respect to the amount of noise. In all of the tested cases, the proposed method provides the best results compared to other methods.

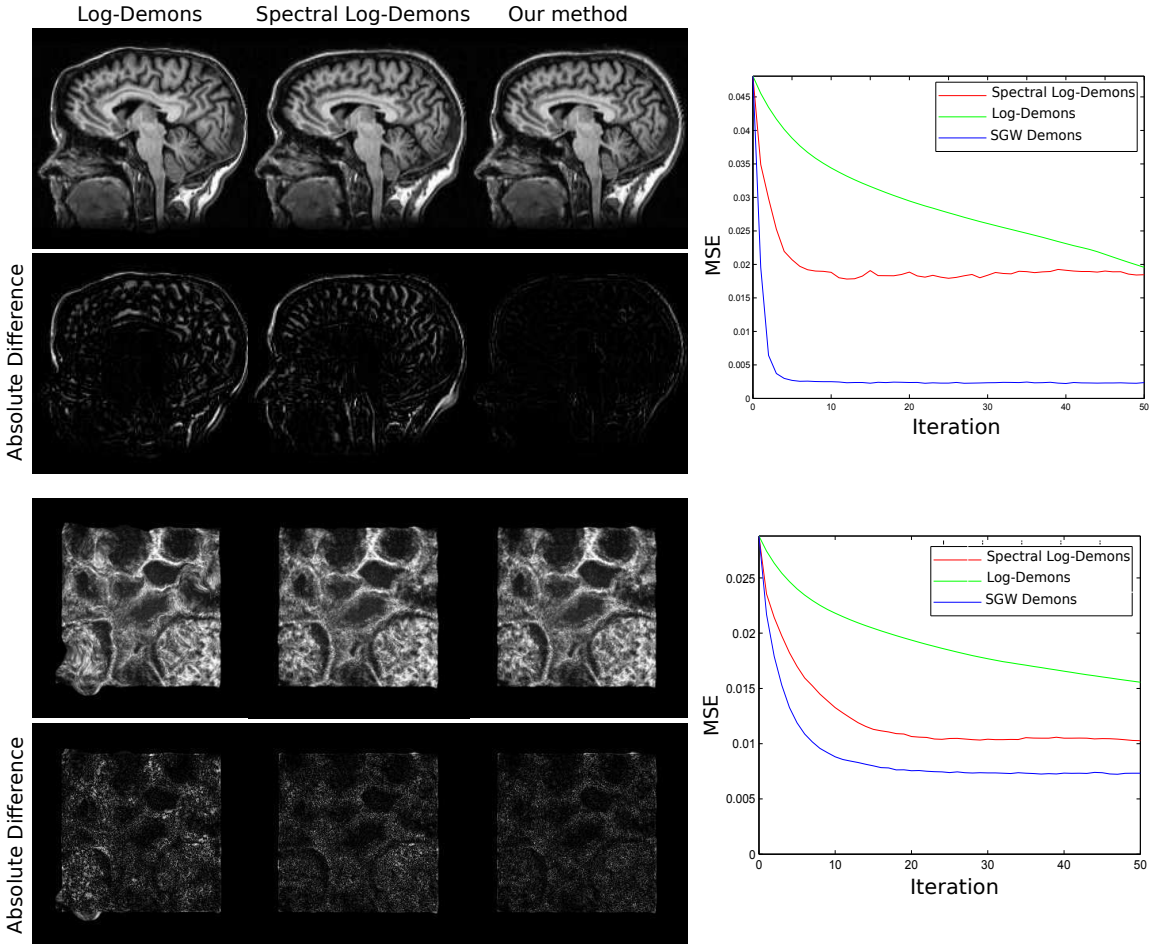

Figure 4.12 – Comparison between our proposal and the existing methods on T1 brain images and endomicroscopic images when no noise is added

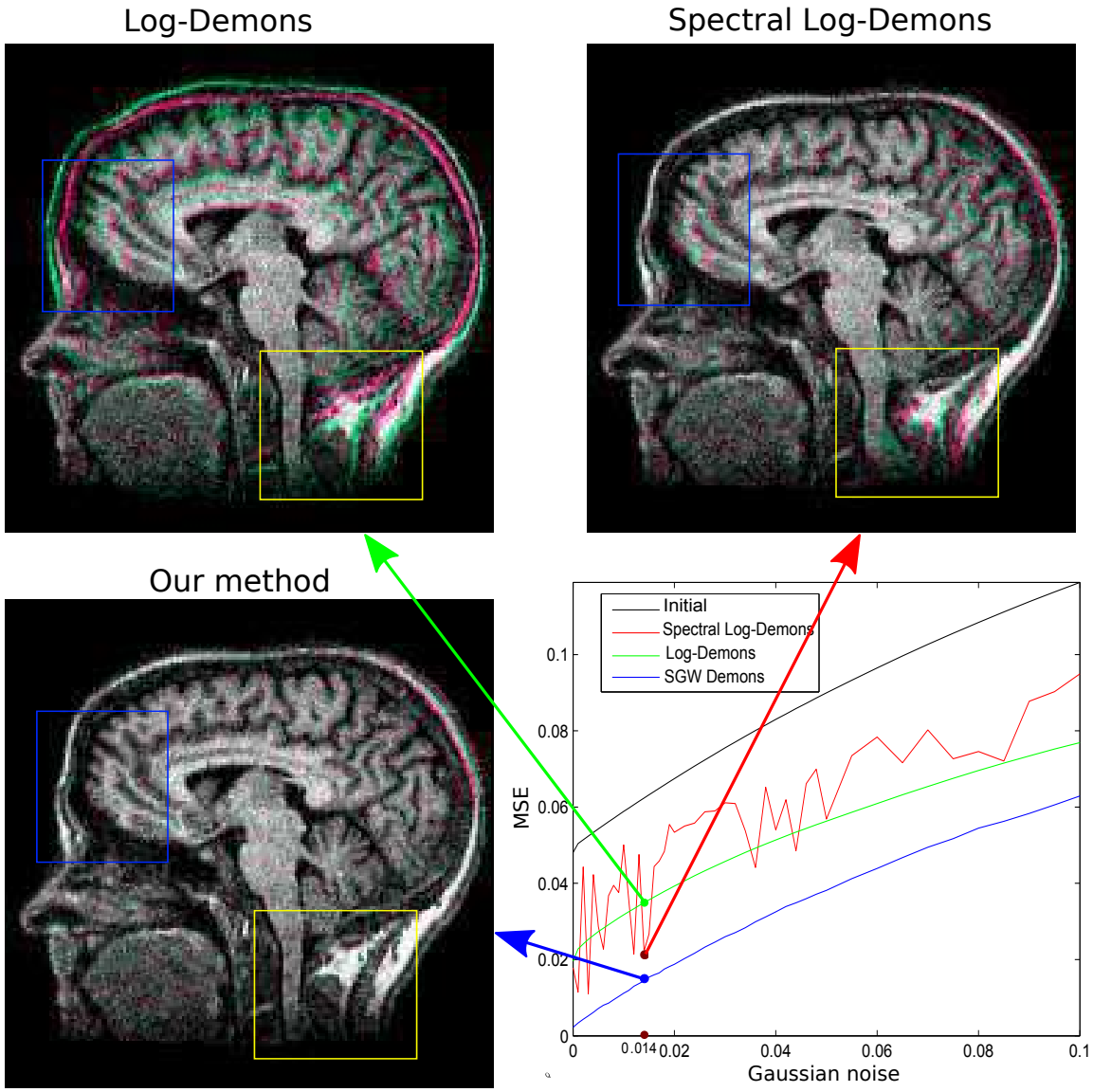

Figure 4.13 – MSE of Log-Demons, Spectral Log-Demons methods, and our method with respect to Gaussian noise (standard deviation σ_{noise})

4.6 Conclusion

In this chapter, different graph based non-rigid image registration methods on classical images on a regular grid were described. Firstly, the fundamental graph theory

was introduced, in order to have an overview of the use of the data representation on graphs as well as the spectral graph theory. The classical image registration methods such as Log-Demons and Bspline based on local iterative gradient easily fall into local minima. The Spectral-Demons method [70] utilizes the graph spectrum as a geometric constraint to capture large deformations. It was used to examine the registration of microendoscopic images, but failed to succeed due to the inability to operate on images with much noise. Otherwise, this work is motivated by the idea of using graph spectrum in registration. This work proposes a Spectral Bspline method and examines it on microendoscopic images. However, the improvement of the Spectral Bspline method is minor compared to the classical one, but is computationally expensive due to the graph computation in every line search step. Next, this work proposes a new strategy that is based on the Log-Demons framework and utilizes the Spectral Graph Wavelets decomposition as a geometric constraint instead of the graph spectrum. The proposal outperforms the existing methods that use the similar Demons framework. In general, the Spectral Log-Demons method and the proposal converge faster than the classical Log-Demons framework and capture the large deformation while the Log-Demons method converges slowly due to the gradient update. However, when much noise exists, the Spectral-Log Demons method fails to register the images. Conversely, the proposed method uses Spectral Graph Wavelets still keeps its advantages over the Log-Demons and Spectral-Demons methods when the amount of noise increases. The experiments on T1 brain images when increasing Gaussian noise is added shows that the Spectral Demons method is difficult to predict when it converges because the energy measurement with respect to noise fluctuates as the noise increases.

Although registration of microendoscopic images with irregularly sampled data is still a challenging problem to overcome, the idea of using the Spectral Graph Wavelet decomposition in image registration motivated our research on registration of images on irregular grids. This is because such methods have shown to provide improvements over the existing ones. The next chapter presents a method to register microendoscopic images on irregular grids and the solution to construct a panorama from a sequence of images on irregular grids.

Chapter 5

Image Registration and Mosaicing of Images on Irregular Grids

Contents

5.1 Introduction 79

5.2 Problem Formulation 80

5.3 Graph construction for image on irregular grid 84

5.4 Registration for Images on Irregular Grids 87

5.4.1 Experimental Results 90

5.5 Mosaics of images on irregular grids 94

5.5.1 The workflow of mosaics construction 95

5.5.2 Results 97

5.6 Conclusions 103

5.1 Introduction

As it was introduced in Chapter 2, in a microendoscopic acquisition, each image is taken by a multiphoton microendoscopic whose optical fiber scans along a spiral

path, starting from the center to the periphery of the area. Such scanning with a temporal sampling produces a list of raw pixels on an irregular grid with floating coordinates. Thus, each acquired image is a set of floating point coordinates with different point densities at different regions. In addition, the images also suffer from noise and distortions due to the movement of the probe and the soft tissue.

Our contribution that investigates the Spectral Graph Wavelet decomposition under the Log-Demons framework on a classical Cartesian grid specified two problems, *a)* to find an appropriate framework that is suitable to adapt with the expensive computation of graph, and *b)* to propose a method that overcomes the problem of the existing method when registering noisy images. This is a stepping stone in our goal to develop image registration of microendoscopic images on irregular grids.

This chapter, firstly, describes our contribution *"Image Registration for Biomedical Images on Irregular Grids"* [91], a registration method of images on irregular grids that is based on our previous contribution using Spectral Graph Wavelet decomposition under the Log-Demons framework. In our registration method, the fixed image F and moving image M respectively contain the intensity spaces I_F and I_M. I_F and I_M are set on the irregular floating coordinate spaces X_F, X_M acquired by the spiral scanning of the microendoscope.

Secondly, we propose a panorama construction from the images on irregular grids. The local misalignment of the images used to create a panorama is compensated by the registration of images on irregular grids. Note that the images on irregular grids are projected on a Cartesian grid only for visualization. The next section will begin with the graph construction of an image on an irregular grid.

5.2 Problem Formulation

So far in the literature, rigid transformation is efficient for many panorama construction applications as it globally aligns an image sequence into a right position of the panorama. However, the local transformations due to structural changes of objects and distortions caused by the camera sensor also need to be compensated (Figure 5.1).

Our aim is to process on raw data on irregular grids. Unfortunately, the microendoscope system crashed during the time of this research. The physicians were able to conserve the images in classical image format on regular grid but not the raw data on irregular grids. Thus, the image acquisition was simulated by taking an outgoing spiral sampling of 125 round turns (with increasing radius), 500 samples each turn, starting from the center of each image on regular grid to obtain an image on irregular grid, giving $n = 125 \times 500 = 62500$ samples in total. A sampling frequency $f = 1416$ is used. Such that, the spatial coordinates of samples are defined by:

$$\begin{cases} V_x = r\cos(\omega t) \\ V_y = r\sin(\omega t), \end{cases} \tag{5.1}$$

where $\omega = 2\pi f$, $r = 0 : \frac{1}{f} : \frac{n-1}{f}$ and $t = 0 : \frac{1}{500f} : \frac{n-1}{500f}$.

Note that, this simulation does not give exact spatial coordinates of points as in the real case, but give a similar spiral acquisition form. To avoid confusion and differentiate between the image in the image sequence and the one used for registration, let us call an image in the image sequence a "frame", and the one used for registration an "image". Once we obtain the images with spiral acquisition, the problem is formulated as follows:

Suppose the frames in sequence are globally pairwise aligned. Each two frames of the same scene have an overlapping part with non-rigid deformations. We need to nonrigidly register two images cropped from the overlapping region between the two frames in the sequence.

As an example, Figure 5.2 shows two frames of the microendoscopic sequence of frames. The first objective of this chapter is to find the transformation between fixed and moving images F and M cropped from the overlapping part of the two input frames. In particular, the fixed image F is cropped from the region covered by the red rectangle of the first frame presented on Figure 5.2, and the moving image M is cropped from the region covered by the blue rectangle of the second frame on Figure 5.2.

As mentioned earlier, F and M are actually two sets of points, each point contains

the information of the intensity value and the spatial coordinates. The intensity space I_F of F and I_M of M are respectively set on the irregular coordinate spaces $X_F, X_M \in \mathbb{R}^2$. Subsequently, the two images have different point densities and the graph topologies as shown in Figure 5.3.

From these images, we propose a panorama construction from the image sequence on irregular grids. In this panorama construction, the motion distortions are compensated by the non-rigid registration.

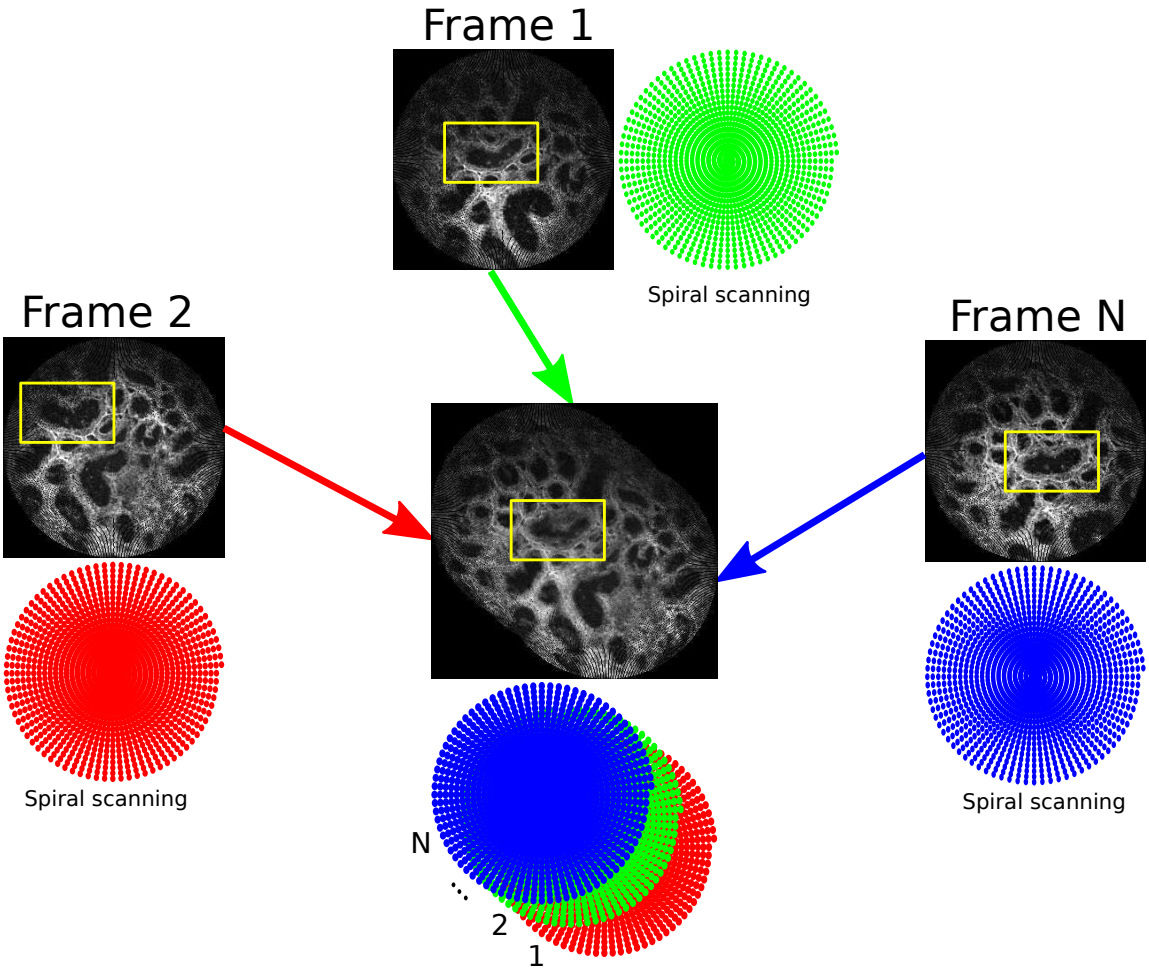

Figure 5.1 – Panorama construction from a sequence of frames on irregular grids without nonrigid deformation correction.

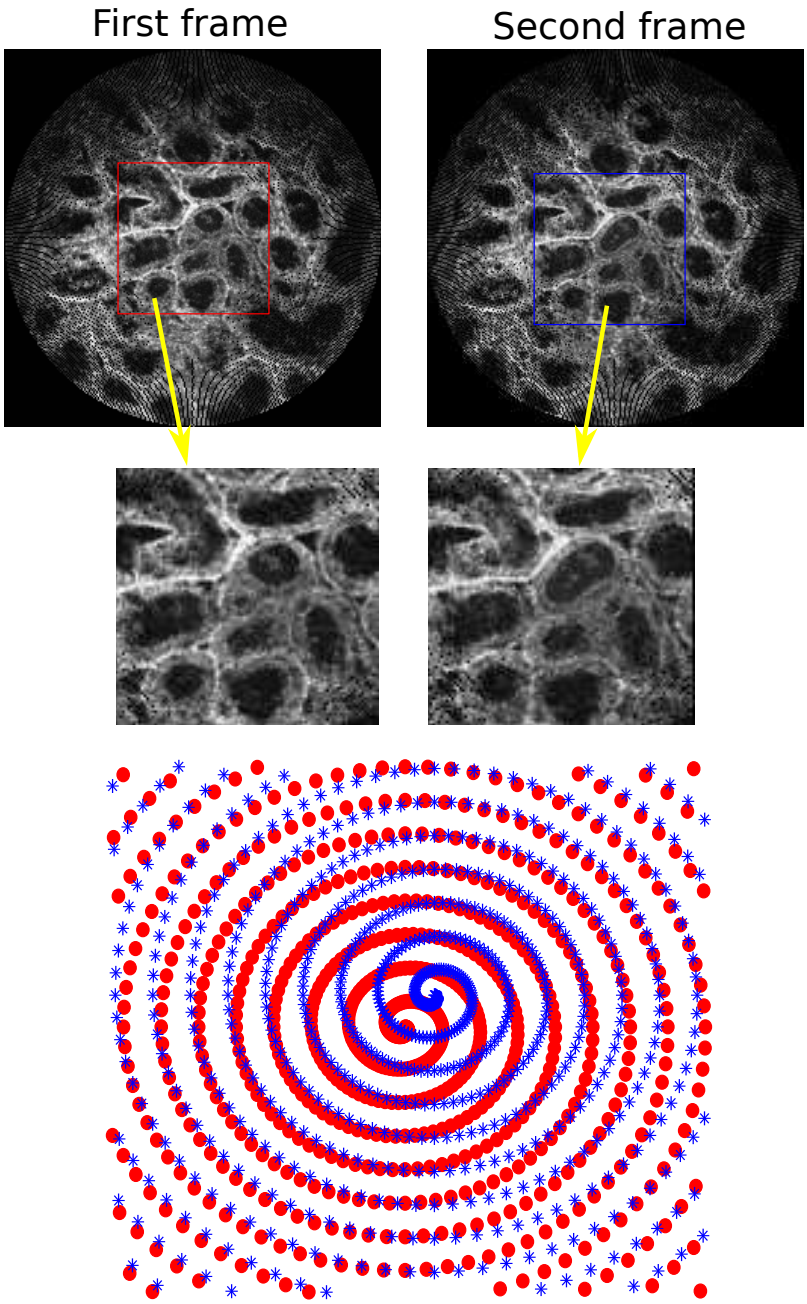

Figure 5.2 – Two images cropped from an overlapping region of two frames, and the representation of points on spiral acquisition of 20 turns, 80 points/turn (the red points belong to the first image and the blue points belong to the second image

5.3 Graph construction for image on irregular grid

In this section, we discuss how a graph is constructed on images on irregular grids including the graph topology and the edge weight computation. As mentioned earlier, each image on an irregular grid is a set of points with floating coordinates.

If in the case of graph representation of images on a regular grid, it is simple to construct the neighboring connectivity of each point, it is much more complicated to construct the graph connectivity of image on an irregular grid. This happens because in the regular case, the point coordinates are in analogy with the point ordering, one can easily define the neighbors of each point. In contrast, the ordering of points on an irregular grid is not relevant to the point coordinates.

In our research, each point of the irregular image is considered as a vertex and the k-nearest neighbor scheme is applied to find adjacent points. Each vertex is connected with k vertices with the shortest Euclidean distance.

Figure 5.3 presents the graph topologies with respectivelly 1, 2, 4, 8 neighbor connectivities of two images cropped from different regions of a frame with acquisition of 20 turns and 80 points each turn. The graph representation of the image cropped at the center region is in blue, while the graph representation of the image cropped at the upper left region is in red. In the case of 1 neighboring graph connectivity, the connections between is similar to the scanning path of the system. The higher the value of graph connectivity is, the more points at different turns of the spiral are connected.

Once the graph neighborhood is defined, we now discuss the edge weight computation. Suppose d_{ij} is the distance between two vertices v_i and v_j. The distance, as stated in the previous chapter, it can be the combination of the intensity difference and the Euclidean distance. In common, d_{ij} is established by the difference between intensity values of vertex v_i and vertex v_j. The edge weight between these two vertices v_i and v_j is denoted as:

$$w_{ij} = \begin{cases} \exp\left(-\frac{d_{ij}^2}{K^2}\right) & \text{if } (i,j) \in \mathcal{E} \ , \\ 0 & \text{otherwise,} \end{cases} \tag{5.2}$$

The value of K, similar to the case of regular grid, affects the influence of the distance between adjacent points to the graph weights. However, the level of redundancy at the center is high while missing points exist at the border, the graph weight computation that depends on the distance between points is expensive, complicated to keep tract on and sensitive to noise. For simplicity, in our registration on irregular grids, we use the binary graph where 1 is given to an edge that connects two neighboring points and 0 is given to adjacency value of points with no connection, such that:

$$w_{ij} = \begin{cases} 1 & \text{if } (i,j) \in \mathcal{E} \ , \\ 0 & \text{otherwise,} \end{cases} \tag{5.3}$$

Once the graph construction as well as the computation of weights are defined, the Spectral Graph Wavelet decomposition is obtained as it was described in the previous chapter. In the next section, the proposed strategy to register images on irregular grid with the Spectral Graph Wavelet constraint is described.

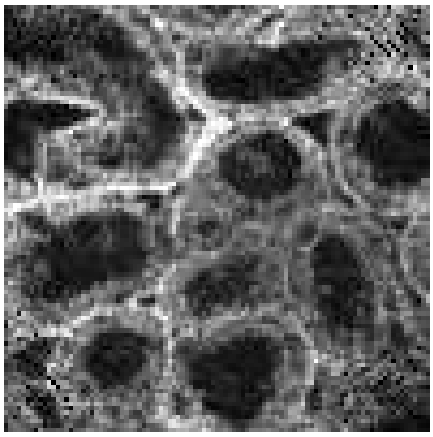

(a) Fixed image

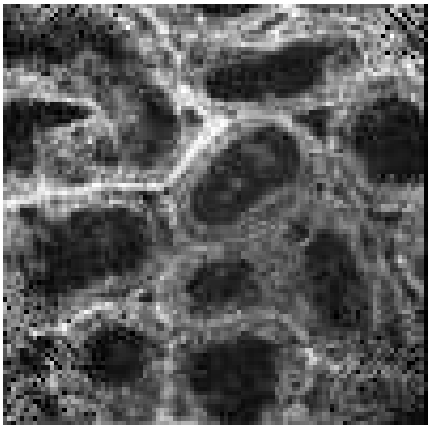

(b) Moving image

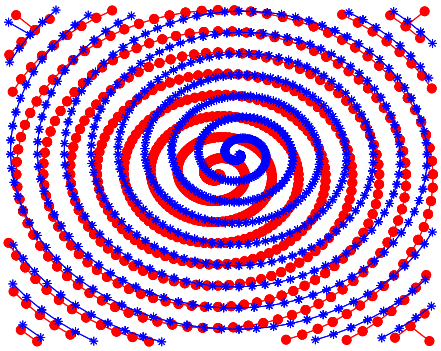

(c) 1 neighborhood graph connectivity of fixed and moving images

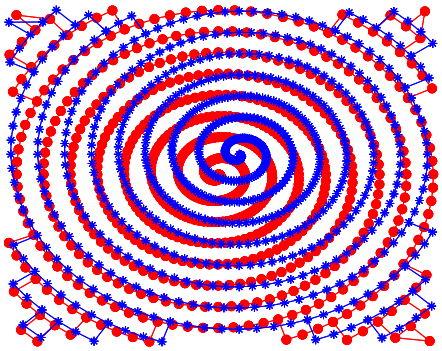

(d) 2 neighborhood graph connectivity of fixed and moving images

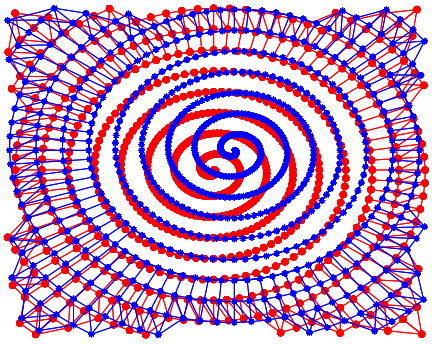

(e) 4 neighborhood graph connectivity of fixed and moving images

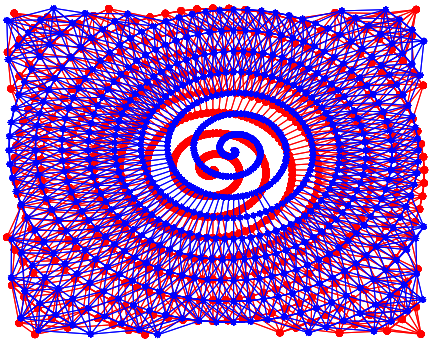

(f) 8 neighborhood graph connectivity of fixed and moving images

Figure 5.3 – Graph topology of images cropped at different regions of a frame with spiral acquisition of 20 turns, 80 points/turn

5.4 Registration for Images on Irregular Grids

In this section, the objective function that contains the SGW components for registration of images on irregular grids is proposed. Recall that each image on an irregular grid is a set of points with floating coordinates. The SGWs of an image on an irregular grid are computed at t scales. For each image we obtain $t+1$ column vectors, the first component is the coarse approximation, and the rest are the SGW coefficients at scales $1, \ldots, t$ (Figure 5.4). Each component has the same size as the image. The first k components at lower bands are used for registration, given by $W_F \in \mathbb{R}^{m \times k}$ and $W_M \in \mathbb{R}^{n \times k}$ for the fixed and moving images, where m, n are the numbers of points of the images.

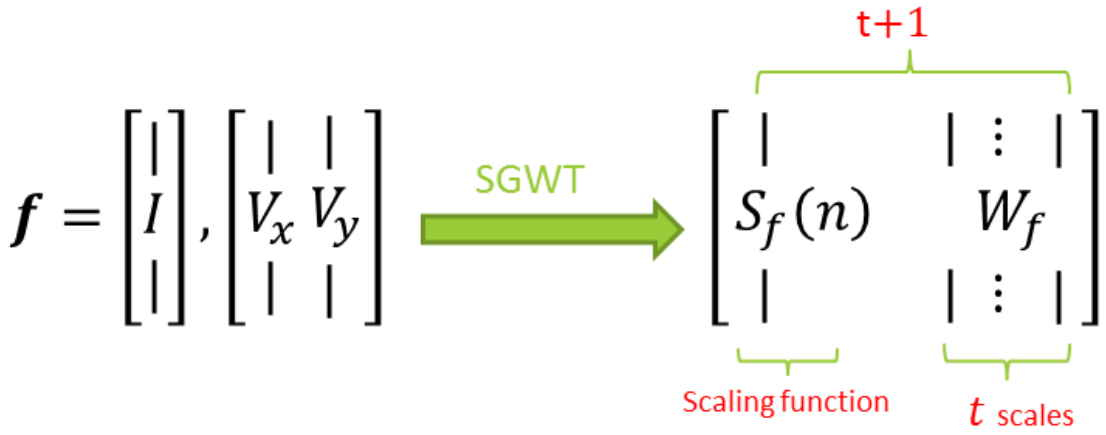

Figure 5.4 – Spectral Graph Wavelet Transform of image on irregular grid

Figure 5.5 shows the SGW decomposition of an image on an irregular grid with different graph neighboring connectivities (1, 2, 4, 8, 16 neighboring connectivities respectively from the top to the bottom) at 4 scales. Each scale is projected on a Cartesian grid for visualization. The first column of Figure 5.5 presents the SGW coefficients of the low-pass approximation and the following columns present the SGW coefficients at 4 scales.

Once W_F and W_M are computed, each fixed and moving images on irregular grids can be cast into the feature vectors that consist of intensity, spatial and SGW infor-

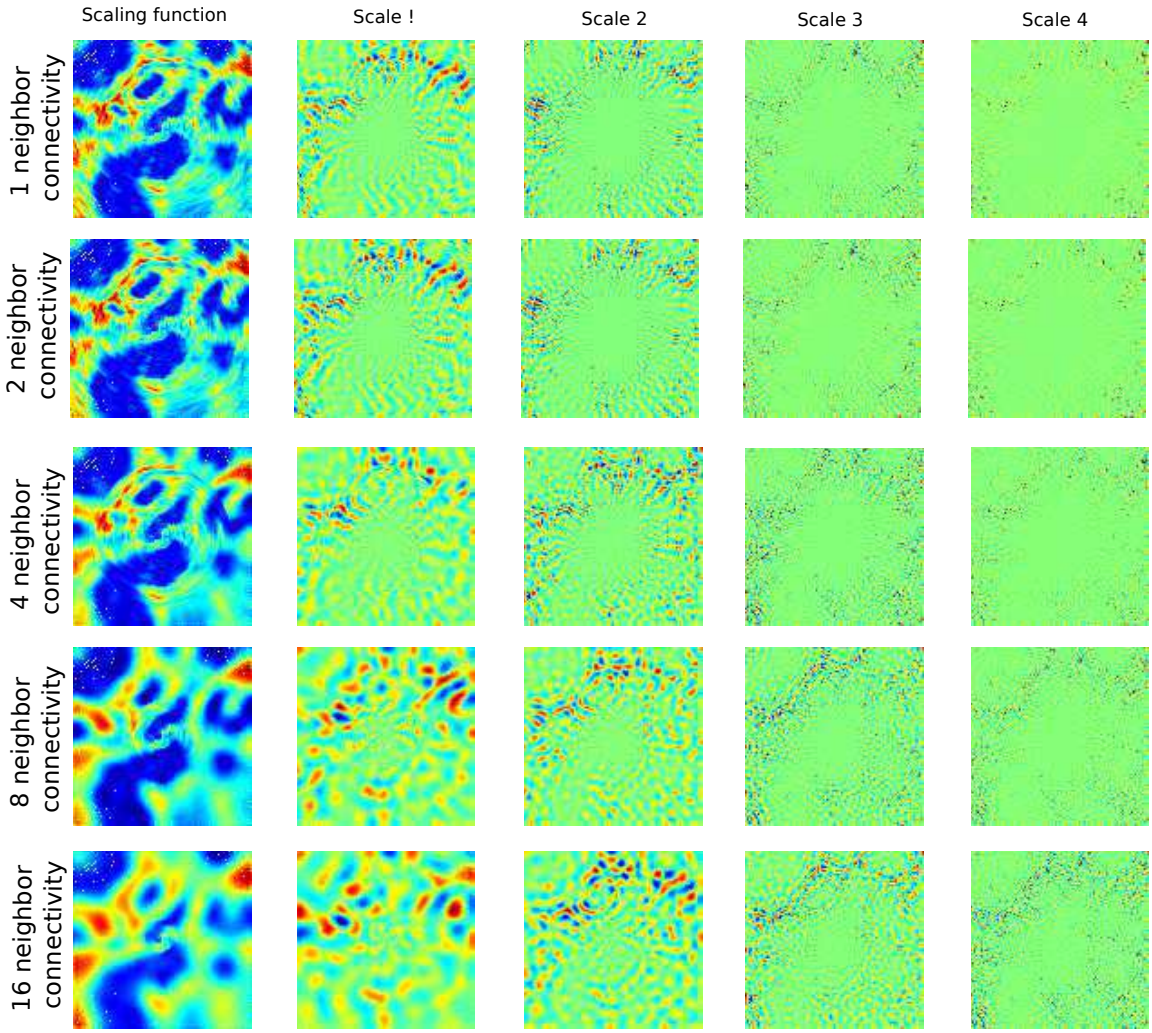

Figure 5.5 – Spectral Graph Wavelets decomposition of a microendoscopic image on an irregular grid , at 4 scales with respectively 1, 2, 4, 8, 16 of graph connectivities from the top to the bottom.

mation: $F = (\alpha_i I_F, \alpha_r X_F, \alpha_g W_F)$ and $M = (\alpha_i I_M, \alpha_r X_M, \alpha_g W_M)$. $X_F = (V_{xf}, V_{yf})$ and $X_M = (V_{xm}, V_{ym})$ are floating coordinates of points in fixed and moving images. In practice, the SGWs can be replaced by any mean of geometric representation (such as the Graph Spectra).

To overcome the problem of the gradient update scheme (mentioned in the pre-

vious chapter) that usually falls into local minima, the registration becomes a direct feature matching problem. The objective function with SGW constraint is defined as:

$$E(F, M, s) = \alpha_i ||I_F - I_{M \circ s}||^2 + \alpha_s ||\mathbf{x}_F - \mathbf{x}_{M \circ s}||^2 + \alpha_g ||W_F - W_{M \circ s}||^2, \qquad (5.4)$$

where α_s is the spatial weight. The spatial term is added to prevent the motion vector from going too far.

Note that, the two images have different point distributions. The moving image is thus pre-interpolated to the grid of the fixed image using the scatter interpolation technique [1] that interpolates from the irregularly sampled data.

The optimization is an iterative method under the Log-Demons framework. The Log-Demons framework allows a diffeomorphic registration. That means the images, as for the precedent method, are registered in both forward (F to $M \circ s$) and backward (M to $F \circ s^{-1}$) matching. In each iteration, SGW are computed for both updated images $M \circ s$ and $F \circ s^{-1}$. The intermediate update field δv is the average of the update fields in forward and backward mapping δv_{fw} and $-\delta v_{\text{bw}}$, where the δv_{fw} and δv_{bw} are respectively given by a nearest neighbor search to minimize Equation 5.4 from F to $M \circ s$ and from M to $F \circ s^{-1}$. δv is then smoothed by a Gaussian kernel K_{fluid} with standard deviation σ_{fluid}. The velocity field v is updated by the computed update field and then smoothed by a Gaussian kernel K_{diff} with σ_{diff}. The registration is summarized in Algorithm 12.

Input: $F = (I_F, V_{xf}, V_{yf})$, $M = (I_M, V_{xm}, V_{ym})$
Output: Transformation field $s = \exp(v)$
Initialize: $S \leftarrow$ interpolate (M, V_{xf}, V_{yf});
while $i < maxiter$ **do**
  $W_{F \circ s^{-1}} \leftarrow computeSGW(F \circ s^{-1})$;
  $W_{M \circ s} \leftarrow computeSGW(M \circ s)$;
  $\delta v_{\text{fw}} \leftarrow \text{argmin}(E(F, M \circ s, \delta v))$;
  $\delta v_{\text{bw}} \leftarrow \text{argmin}(E(M, F \circ s^{-1}, \delta v))$;
  $\delta v \leftarrow K_{\text{fluid}} \star (\delta v_{\text{fw}} - \delta v_{\text{bw}})$;
  $v \leftarrow K_{\text{diff}} \star \log(\exp(v) \circ \exp(\delta v))$;
end

Algorithm 12: *registerOnIrregularGrid*()

5.4.1 Experimental Results

Having briefly described the graph construction and registration of images on irregular grids, this subsection firstly compares our experimental results with the existing registration methods on a regular grid. Then, different tests of different values of graph connectivity using the proposed registration technique on irregular grids are provided.

5.4.1.1 Benchmarking with existing methods

Here, the proposed method is benchmarked against the Spectral Demons algorithm on irregular grids and the two existing methods on the regular grid (i.e. Spectral Demons and SGW Demons). The experiments use two random pairs of the frames. For each two consecutive frames of the sequence, global shift is obtained by a block matching algorithm. With the known cumulative global shift between each two frames, the target and source images are cropped from the overlapping region of two different frames. The images are projected on 100 by 100 Cartesian grid for the visualization and for the registration on regular grid.

The registration results are shown on Figure 5.6 with the same values of $\alpha_g = 2, \alpha_s = 1$ and $\alpha_i = 6$ for registrations on irregular grids. Each row represent each pair of the images to be registered and their registration results. It can be clearly seen

that the registration on a regular grid suffers from the smoothing effect and thus, the registration fails. The Signal to Noise Ratio values with respect to the number of iterations are presented on Figure 5.7. In both cases, the registrations on regular grid are inconsistent. Especially, in the registration of the second pair of images, the Spectral Demons method strongly diverges as the number of iterations increases. In the registration on irregular grids, the SGW Demons improves approximately 3% for the registration of the first pair of images and 1.7% for the second pair. And in both registrations on the regular and irregular grid, the SGW gives more consistent registration than the Graph Spectra.

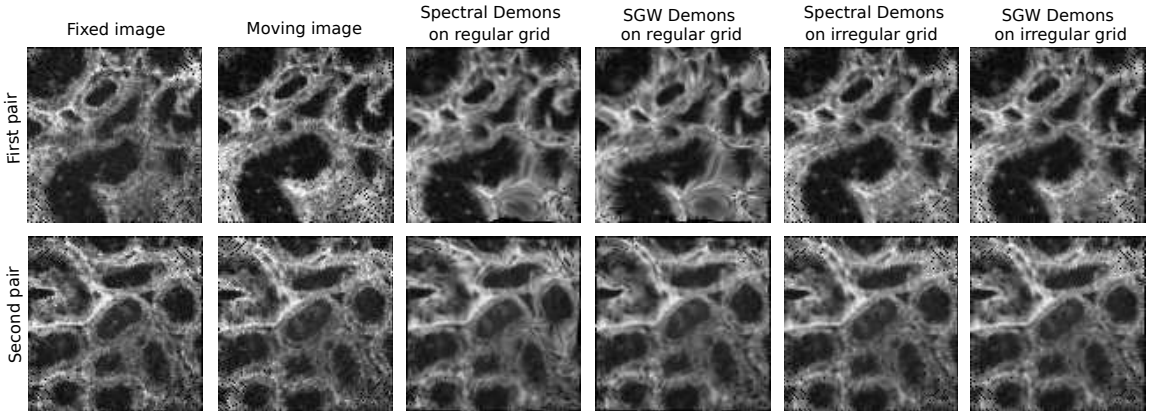

Figure 5.6 – Comparison between the registered images of our method and the existing methods for two pairs of images($\alpha_g = 2, \alpha_s = 1, \alpha_i = 6$ for registration on irregular grid)

Figure 5.8 shows the comparison between Spectral Demons and SGW Demons on irregular grids for the first pair of images with higher geometric weight ($\alpha_g = 10$). It is more visible that the Graph Spectra is inconsistent and the motion field is more affected by the point density while the SGW remains consistent. However, with higher weight of the geometric constraint, the SNR value tends to slightly decrease.

Figure 5.9 allows us to see more clearly the result of our method applied to the first pair of images on irregular grids. In the representation of the difference, the target image is in the red channel, the source and registered images are in the green channel. The region covered by the red line shows that the differences between the

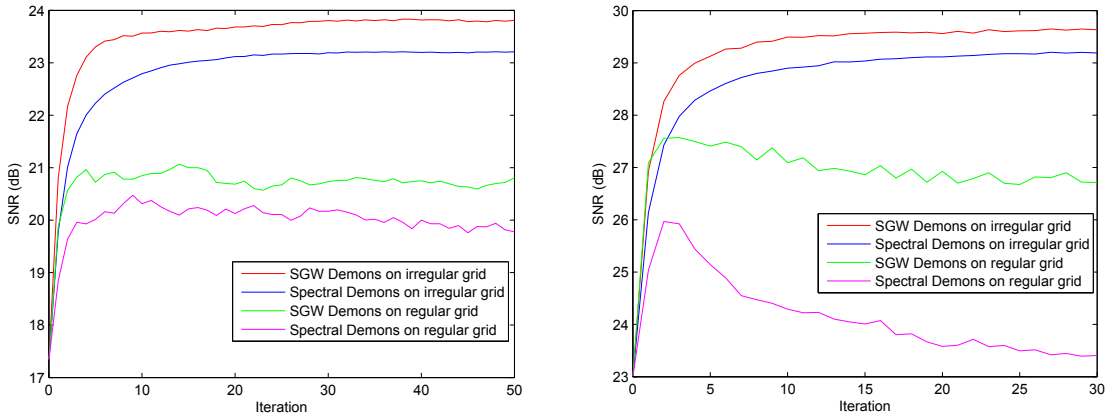

(a) First pair (b) Second pair

Figure 5.7 – SNR with respect to the number of iterations

registered image and the target image have an improvement compared to the initial difference.

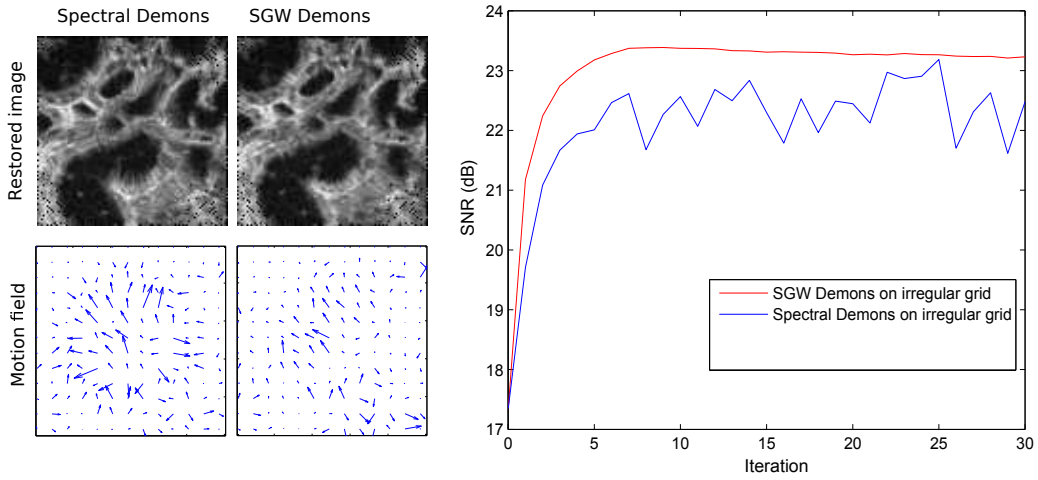

Figure 5.8 – Registration with $\alpha_g = 10, \alpha_s = 5, \alpha_i = 20$

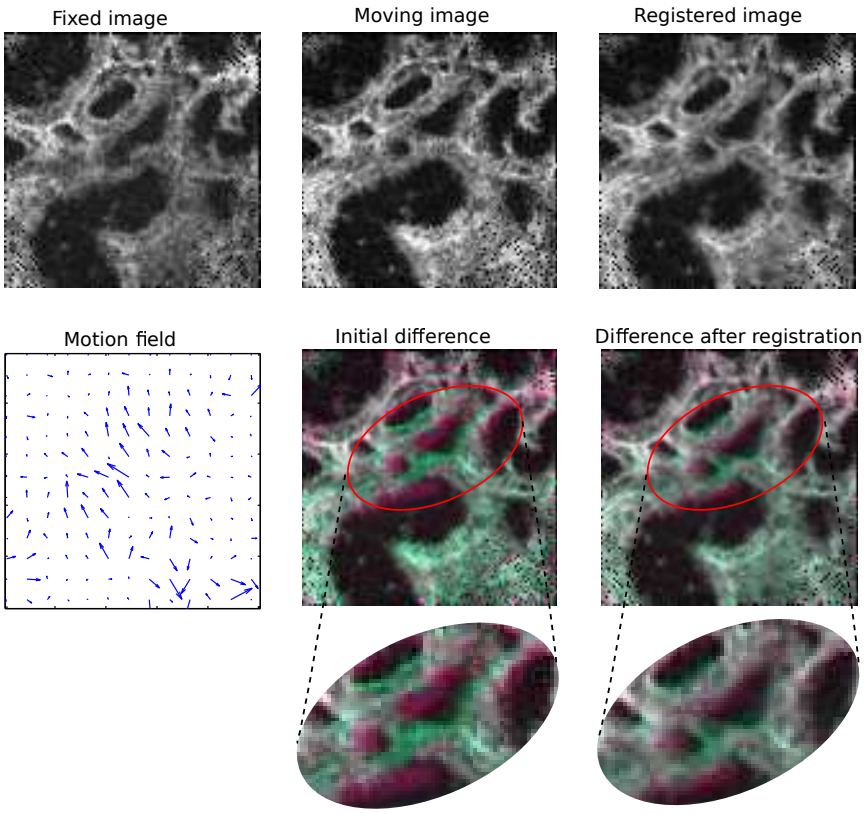

Figure 5.9 – Registration result of the first pair of microendoscopic images on irregular grids

5.4.1.2 Impact of graph connectivity to the registration

In this section, we examine different values of graph connectivity to the registration. We test on the first pair of microendoscopic images used in the previous subsection with two sets of weighting parameters ($\alpha_g = 1, \alpha_s = 5, \alpha_i = 20$) and ($\alpha_g = 1, \alpha_s = 1, \alpha_i = 4$). In this case, in the manner of the overall weighting parameters, the SGW weight increases (from $\alpha_g = 1/26$ to $\alpha_g = 1/6$) while the spatial and intensity weights decrease. Figure 5.10 depicts the energy measurements of the registrations on irregular grids with respect to the values of graph connectivity ranging from 1 to 16. With the first set of weighting parameters ($\alpha_g = 1, \alpha_s = 5, \alpha_i = 20$), the overall MSE value is slightly higher than in the case of registration with the second set of

parameters ($\alpha_g = 1, \alpha_s = 1, \alpha_i = 4$). However, there is no clue to conclude on the impact of the value of graph connectivity to the effectiveness of the registration. In particular, the MSE values fluctuate when the value of graph connectivity increases. With the first set of parameters, the best registration according to the energy value falls into the case of 8 neighbor graph connectivity while with the second set of the weighting parameters, the best registration falls into the case of 7 neighbor graph connectivity.

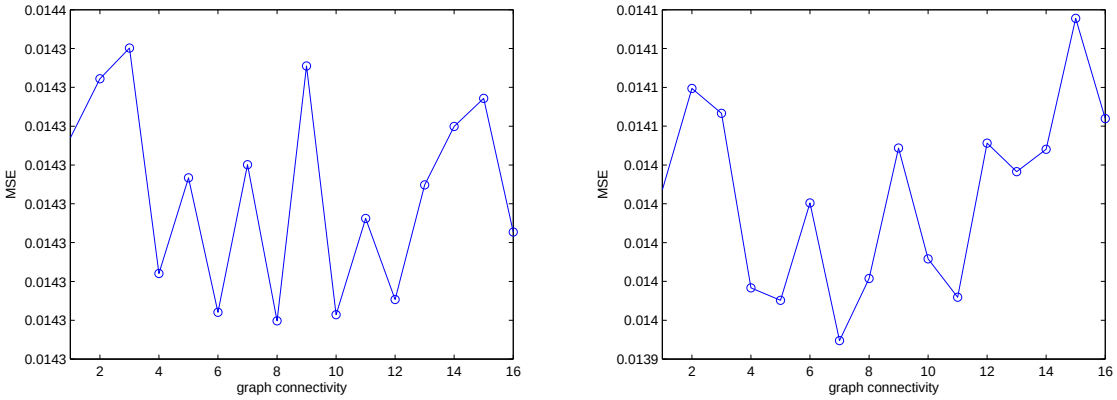

(a) MSE value with respect to graph connectivity ($\alpha_g = 1, \alpha_s = 5, \alpha_i = 20$)

(b) MSE value with respect to graph connectivity ($\alpha_g = 1, \alpha_s = 1, \alpha_i = 4$)

Figure 5.10 – MSE values after registrations of the first pair of microendoscopic images with respect to the values of graph connectivity with two sets of weighting parameters ($\alpha_g = 1, \alpha_s = 5, \alpha_i = 20$ and $\alpha_g = 1, \alpha_s = 1, \alpha_i = 4$)

5.5 Mosaics of images on irregular grids

The multiphoton microscopy using optical fibers is a promising and potent tool for biologists and physicians to examine *in vivo* the information of cell and tissue biology. Although it has gained popularity in the research field of medical imaging devices because of its ability to obtain high resolution, high contrast and minimal phototoxicity, there are still unavoidable limitations such as noise and small field of

view (FOV). The narrow FOV limits experts' assessments of cells to evaluate dangers (such as cancers, ulcers). Therefore, there is a need for providing an accurate and complete representation of the entire region that has been captured from a continuous sequence of time.

The goal of this section is to provide a supportive mosaics construction from an image sequence to enhance the FOV. Such images captured by microendoscope have a spiral sampling, thus, have irregular grids of points. The rigid motion of the optical fiber across the tissue while scanning gives rise to motion artifacts. The movement of soft tissue due to breathing and heart rate also create local non-rigid distortions. Therefore, the mosaics construction needs to be adapted with the non-rigid deformations and the images on irregular grids.

5.5.1 The workflow of mosaics construction

A non-rigid registration technique of images on irregular grid has been previously provided. This is used to compensate for the non rigid deformations during the mosaics construction.

For the mosaic construction, firstly, the pairwise rigid motions between each two consecutive frames are obtained by any of the block matching techniques using cross correlation [116, 43]. Once the pairwise rigid transformation is determined for each two successive frames, the dynamic coordinate system model is then used for the mosaic construction. Thus, for each input frame, the current mosaics is aligned to the coordinate system of the current input frame [60]. This model is more appropriate with our problem because it is more adaptable with our data on irregular grids. Existing models take one specific frame as reference frame and keep the coordinate system of the mosaic fixed at all the iterations, where each input frame is cumulatively aligned to the coordinate system of the reference frame. Conversely, the proposed model aligns between coordinate systems of each two consecutive frames. This has the advantages in the implementation of images on irregular grids where the data structure is complex. The workflow to construct mosaics from a sequence of frames is simply depicted as on Figure 5.11.

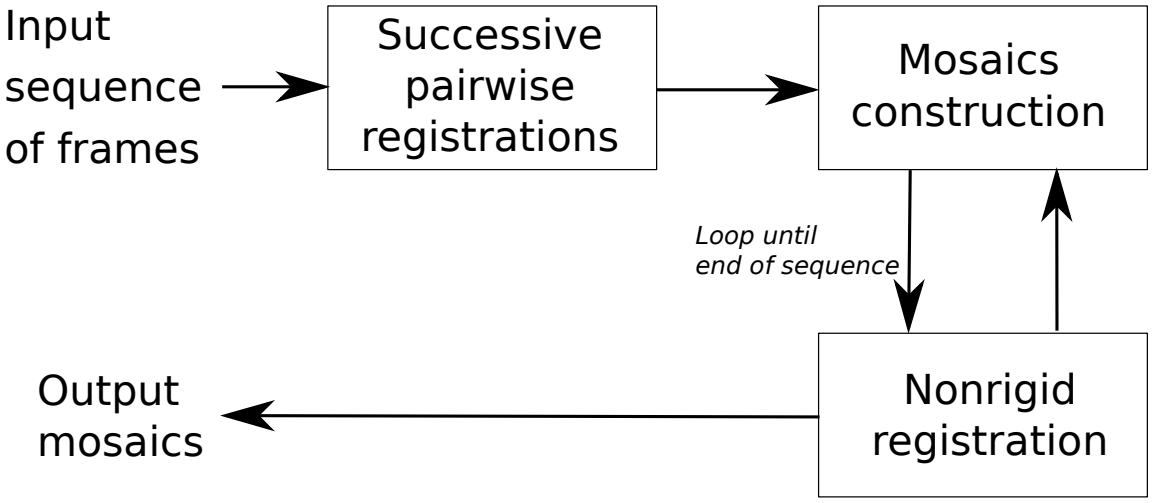

Figure 5.11 – The pipeline to construct mosaic.

Our panorama construction takes the sequence of frames on irregular grids $\mathbf{F} = \{\mathbf{f}_1, \mathbf{f}_1, \ldots, \mathbf{f}_N\}$ as input in a loop that alternates between several steps. In each iteration, a successive input frame $\mathbf{f_{cur}}$ is taken as the input. It is then considered as the fixed image while the current mosaic is considered as the moving image of the nonrigid registration on irregular grids. The current mosaic $\mathbf{M}$ is then recentered to the coordinate system of the current input frame $\mathbf{f_{cur}}$ before it is updated by merging the input frame and the registered mosaic. The mosacing steps are summarized in Algorithm 13.

Input: Sequence of frames $\mathbf{F} = \{\mathbf{f}_1, \mathbf{f}_1, \ldots, \mathbf{f}_N\}$
Output: Mosaic $\mathbf{M}$
$pairwiseRigidRegistration()$;
Initialize: $\mathbf{M} \leftarrow \mathbf{f}_1$;
for $\boldsymbol{f_{cur}}$ *in* $\boldsymbol{F}$ **do**
  $s \leftarrow registerOnIrregularGrid(\mathbf{f_{cur}}, \mathbf{M})$;
  $\mathbf{M} \leftarrow merge(\mathbf{f_{cur}}, \mathbf{M} \circ s)$;
end

Algorithm 13: Mosaic construction

5.5.2 Results

At this last stage, the proposed mosaic construction algorithm is applied to the microendoscopic images on irregular grids. The mosaic construction from a small number of images (two and three frames) is first presented, then the results obtained from a sequence of images is proposed.

As a foundation of our panorama construction, the mosaic constructed from two frames give us a better view of the effectiveness of the nonrigid deformation compensation. As shown in Figure 5.12, each of the two pairs of the examined frames have rigid motions and nonrigid deformations. The first pair of frames are randomly selected in the sequence of 9 temporal frame difference and the second pair of frames are two consecutive frames.

The mosaic constructed from the first pair is shown in Figure 5.13. For a better view, the two frames are positioned in different color channels, one frame in the red channel and the other is placed in the green channel. It can be seen that, without nonrigid registration, the mosaic created with only rigid transformations suffers from shearing of the object in the image. In contrast, the mosaic constructed with nonrigid correction reduces the level of shearing at the overlapping region of the frames. The similar outcome appears in the mosaic constructed from two temporally neighboring frames as shown on Figure 5.14, even though it is less clear how the nonrigid registration improves the mosaic construction than we can see in the first case.

Once the mosaic is constructed from two frames, theoretically, there is no doubt we can construct the mosaic from a sequence of input frames. Figure 5.15 depicts the mosaic constructed from three frames. The left picture of this figure is the mosaic with only rigid alignment and without a nonrigid deformation correction, while the right picture shows the mosaic with nonrigid deformation correction. The noticeable changes between the two mosaics are marked by the yellow and blue rectangles. Similarly, Figure 5.16 illustrates the gain obtained from mosaic construction of twelve frames. Figure 5.16a illustrates the proposed mosaic construction with only rigid motions and Fig 5.16b shows the improvement obtained when the nonrigid registration

is applied to the mosaic construction. The white arrows (a, b, c, d, e, f) point to the zones where changes between the two mosaics with and without nonrigid correction are visually appealing.

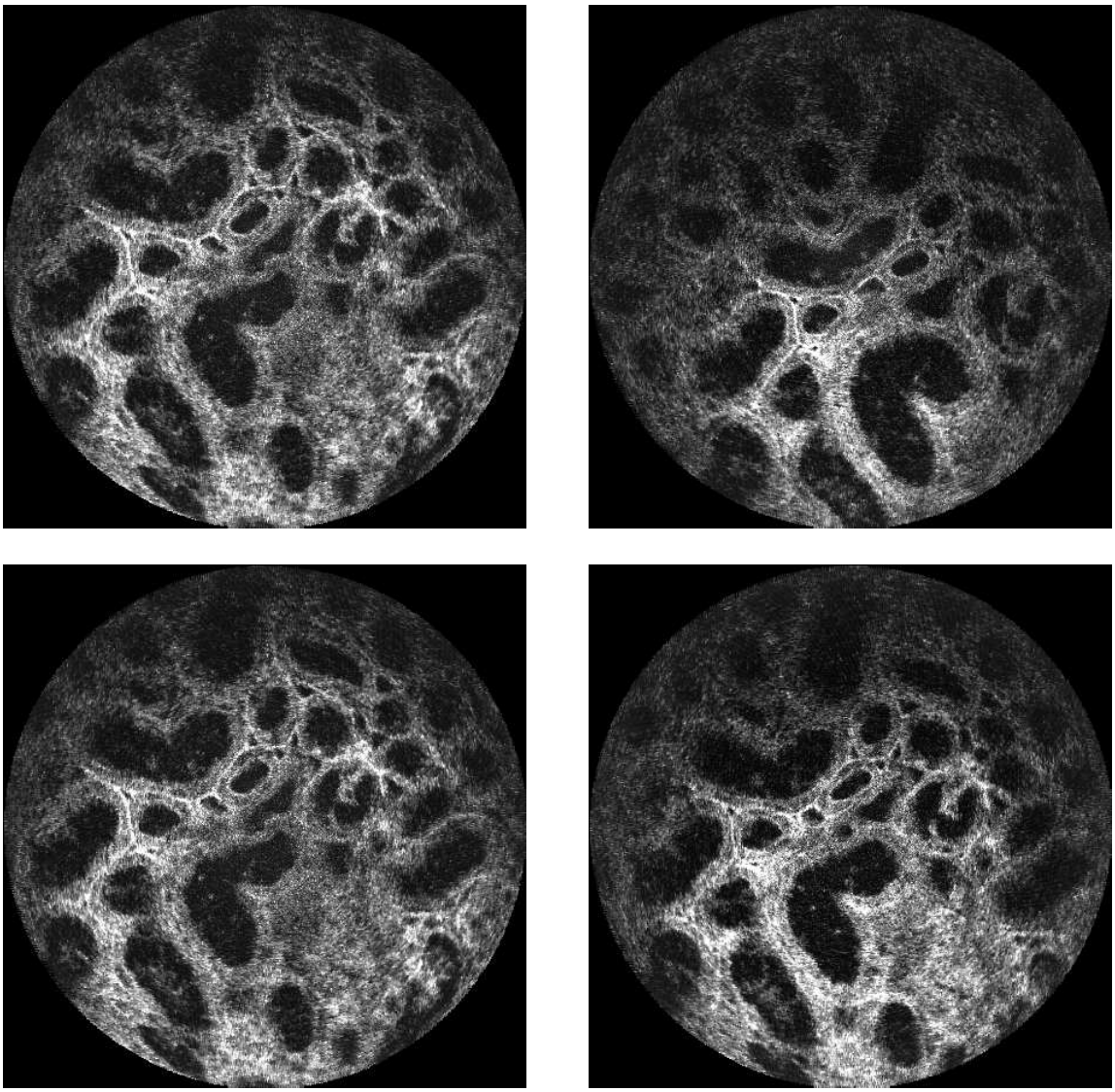

Figure 5.12 – Two pair of random frames from the image sequence (First row: 9 frame difference, Second row: two consecutive frames)

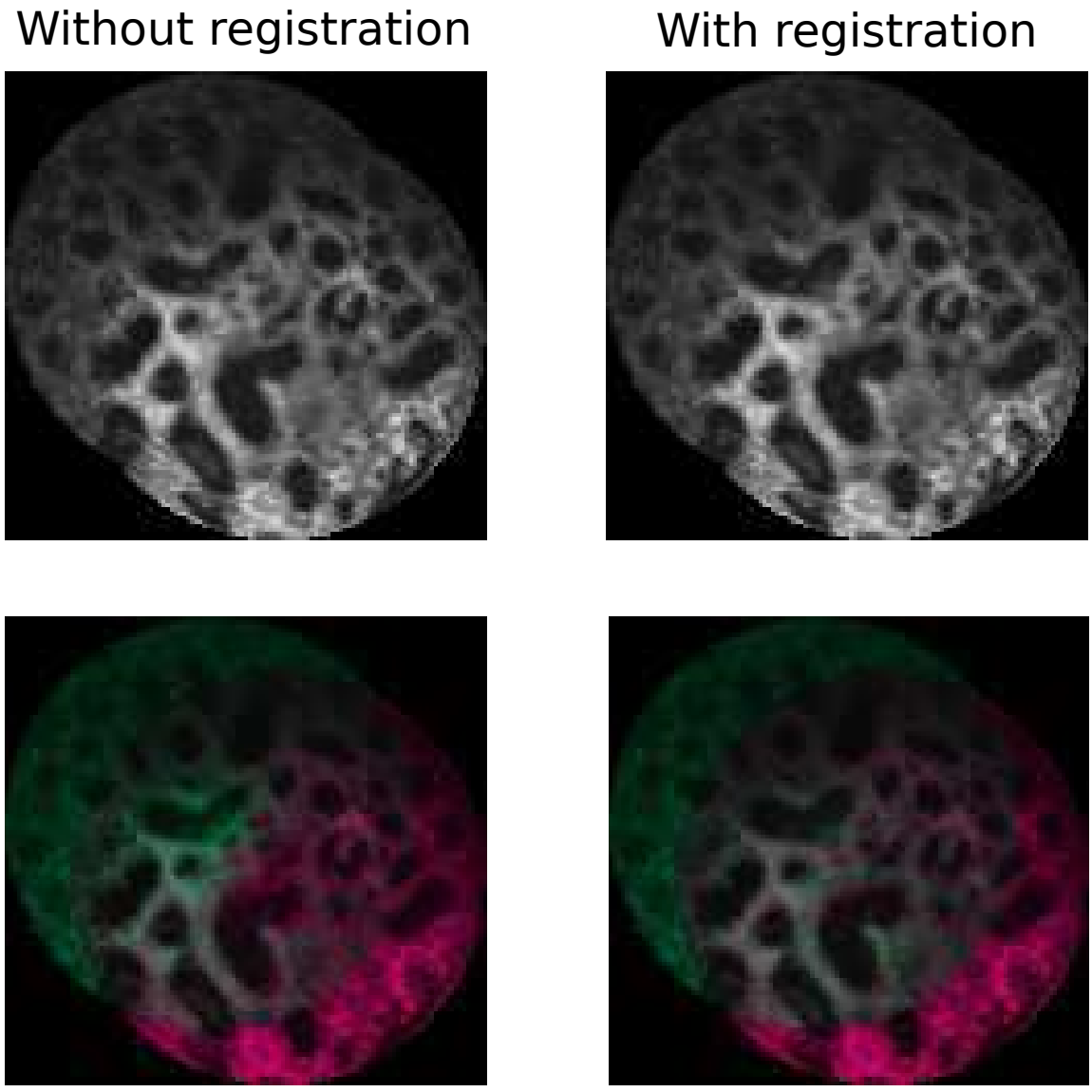

Figure 5.13 – Panorama created from two frames from the image sequence (9 frame difference). (Red channel: First image, Green channel: Second image)

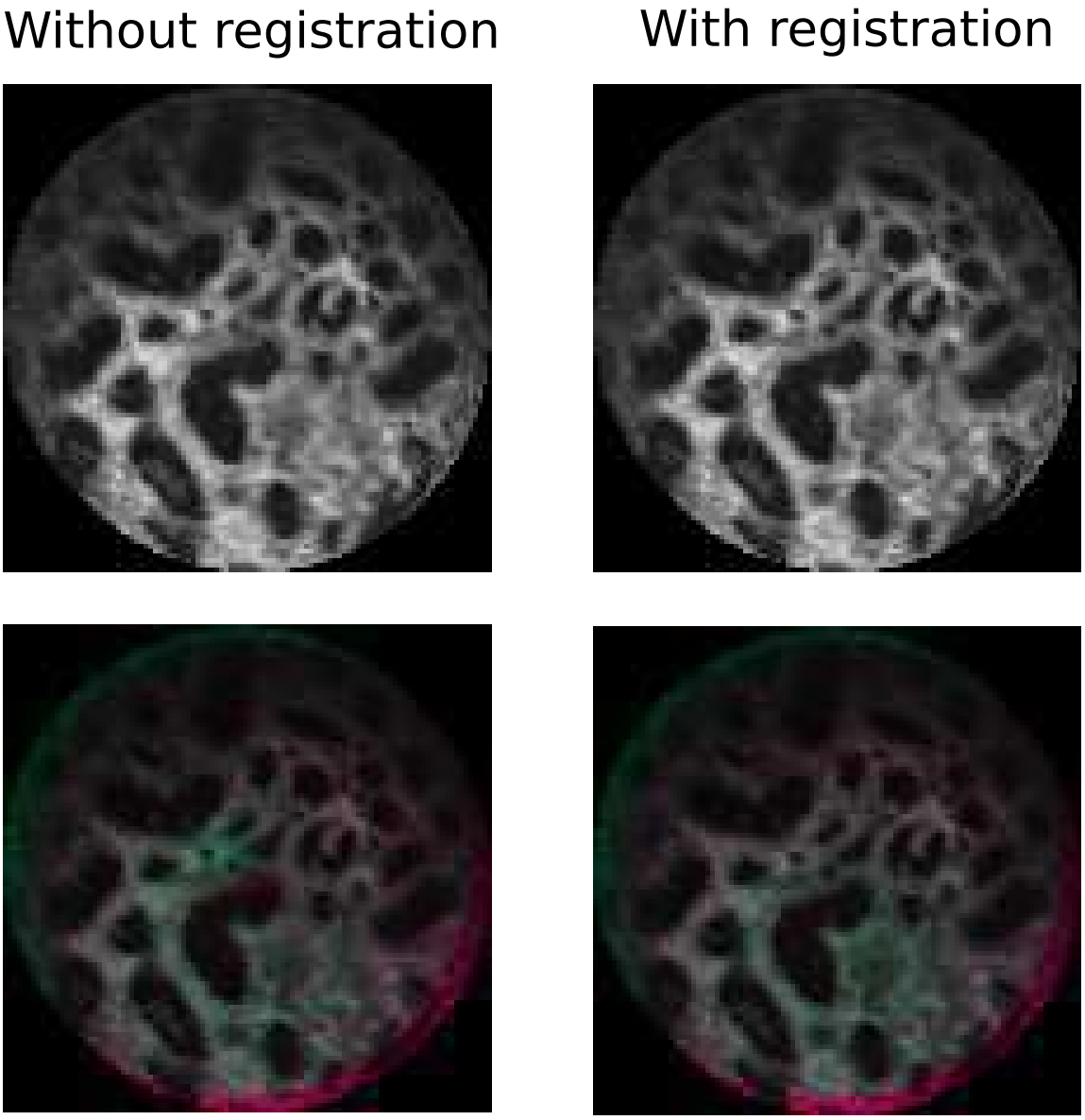

Figure 5.14 – Panorama created from two frames from the image sequence (consecutive frames). (Red channel: First image, Green channel: Second image)

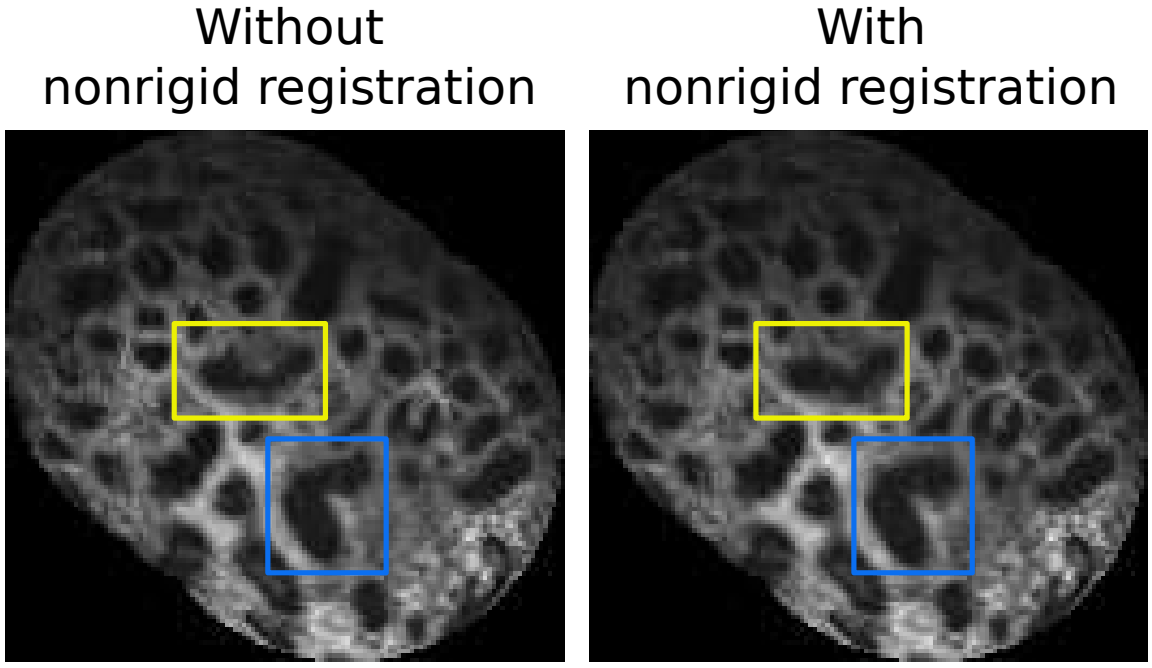

Figure 5.15 – Panorama created from three frames from the image sequence.

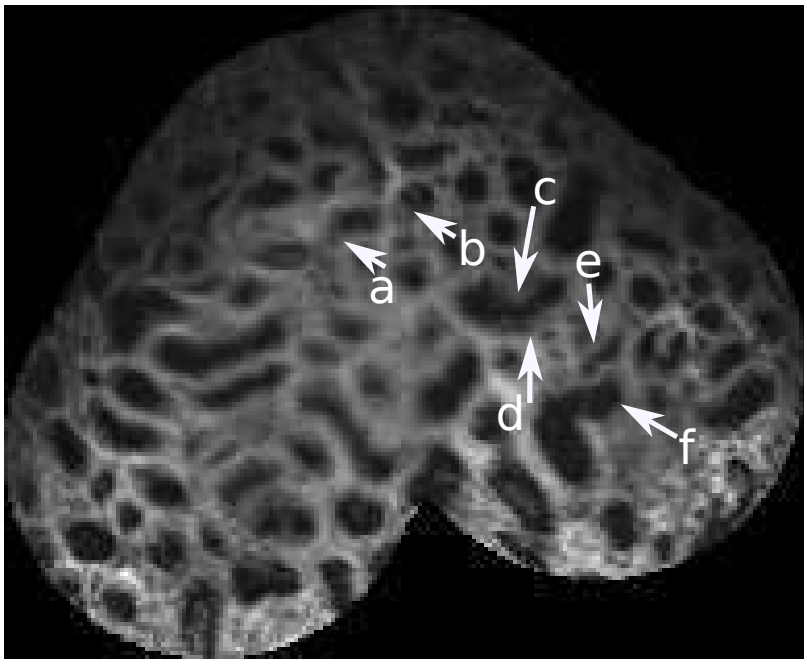

(a) Without nonrigid registration

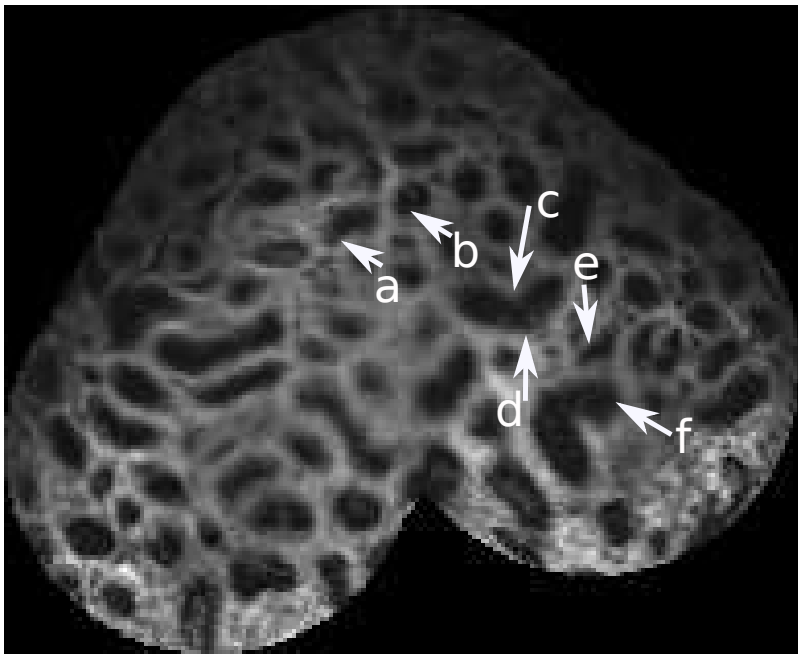

(b) With non-rigid registration

Figure 5.16 – Panorama constructed from a sequence of 12 frames

5.6 Conclusions

In this chapter, we firstly show that the Log-Demons framework can be adapted to the registration of images with floating point coordinates, on irregular grids. In addition, the proposed registration that uses Spectral Graph Wavelet decomposition was extended to the registration on irregular grids. The experimental results show that our application on the raw data without any projection on Cartesian coordinate system performs better than the classical one on a regular grid. In all of the tested cases, the registration based on Graph Wavelet decomposition is more robust than the Graph Spectral based method.

Secondly, the problem of mosaic construction from a sequence of frames on irregular grids has been exposed in this chapter. The experimental results that compare the mosaic constructions with and without nonrigid deformation correction show that the mosaic with nonrigid deformation correction has improvements over the one that uses only rigid motions with less level of shearing. This shows that the nonrigid correction is needed in mosaic construction in medical imaging.

Related to the panorama construction, future work should focus on providing a robust mosaic with global rigid motion correction, that aims to correct the cumulative errors when the frame sequence gets loops back to the start. In addition, the method should be adapted to images on irregular grids.

Chapter 6

Conclusion and Perspectives

We have seen in Chapter 2 a brief description of the two photon microendoscope, as well as the scanning trajectory of the probe. This technology has strong ability to acquire high-resolution images of *in vivo* cells and tissues, high contrast and minimal level of phototoxicity. The optical fiber of the microendoscope, as mentioned earlier, has spiral scanning that centralizes important information. Such kind of scanning produces images on irregular grids with points that are set on a floating coordinate space. Despite the numerous benefits of this technology, processing on such kind of images suffers from several challenges such as illumination changes, noise, soft deformations and distortions, and the uneveness in point distributions.

It was also precised that the demand for an application to enhance the FOV of experts (such as physicians and biologists) has ushered the research on image mosaics. This thesis was set out with the goal of providing wide field images acquisition from the image sequences to the experts, that is to construct a mosaic from the image sequence. The need of an accurate mosaic construction leads to demands of an appropriate nonrigid image registration technique to compensate for the local deformations.

A survey in Chapter 3 revealed that there are several innovative approaches to image processing in general, and to nonrigid image registration in particular in the past decades. The approaches were classified in different groups according to the choices of transformation model, similarity criterion and optimization method. The

Demons approach, among the transformation model category, is known as a powerful approach because it is fast to execute and simple to implement. In addition, the graph based method was found to be attractive as it provides a flexible data representation regardless of the type of data (regular or irregular). The graph spectrum has the strong property to be invariant to isometry. It was combined with the Demons method in the recent research of Lombaert *et al* [70] in order to capture large and complex deformations. However, the robustness to noise is still an open problem.

In Chapter 4, two graph based registration methods on a regular grid were introduced. The first one utilizes the graph spectrum combined with the Bspline model but gain minor improvement compared to the classical Bspline method. In addition, graph computations in each gradient search makes it computationally expensive. The second one alternates the role of graph spectrum with the Spectral Graph Wavelets under the Log-Demons framework. The Log-Demons framework is known to be faster and simpler to implement. It is cast into a fast direct feature matching without any gradient search in order to avoid extensive computations. Thus, it is suitable to adapt with graph based method. Furthermore, the Spectral Graph Wavelet decomposition at low frequency bands can capture the geometric feature of the image and noise is eliminated. Consequently, our contribution outperforms the existing methods on similar framework, and outperforms the Spectral Log-Demons method in term of robustness to noise. This handles two problems in this research, *a)* to propose a framework that is adaptable with irregularly sampled data, consequently suitable with the expensive computation of graphs, and *b)* to adapt with noisy data.

The contributions in the study of images on irregular grids were revealed in Chapter 5. The Log-Demons framework was proven to be adaptable to the registration of images on irregular grids. While the registration of microendoscopic images on regular grid fails, the registration of the raw data without any projection on regular grid gains success. And in any of the tested cases, the application using Spectral Graph Wavelets is more robust than the application using graph spectrum. Once the nonrigid registration is done, the local distortions can be compensated in the mosaic construction. It produces a full view panorama with less level of shearing and misalignment than using only rigid alignment.

This research introduces several advantages as mentioned previously. The Spectral Graph Wavelet decomposition has been used in many application such as denoising, sampling and shape retrieval. To the best of my knowledge, this research is the first to apply Spectral Graph Wavelet decomposition in image registration, similarly to the application of images on irregular grids. I believe that our research will motivate other researches on images on irregular grids, as well as the utilization of Spectral Graph Wavelet decomposition in image registration. However, the application based on graph theory is effective and adaptable to different types of data (regular and irregular). However, it suffers from problems of computation complexity and is time consuming, especially when we need to create a mosaic from a large amount of input frames. This is still one of the most challenging problems in graph based applications.

6.1 Future works

Our research described in this work opens new perspectives and directions for long-term research. To point out a few of the important keys, the following open issues can be addressed:

- **Global adjustment for robust mosaicing.** One of the most appealing challenges in panorama construction is that the cumulative error occurred when the image sequence loops back to where it starts. For this reason, it is important to correct the misalignment between the first and the last, in order to have a seamless panorama. In the context of regular grids, one can use any of the existing bundle adjustment methods. However, to the best of our knowledge, there is no justification of these methods of images on irregular grids. Therefore, future work should include finding a robust global rigid alignment of the image sequence on regular as well as irregular grids.

- **From raw data to image view.** In the registration and mosaics of image on irregular grids, from theoretical point of view, all the information we have is

from the raw data. However, the clinicians need to visualize the data. Consequently, it is necessary to reconstruct a discrete image on a regular grid from the raw data on irregular grids. In this thesis, the images are only projected on a regular grid for visualization with the help of a simple nearest neighbor interpolation and an average of intensity values is taken when redundancies are found at one position. However, this does not give the best quality of image. Future work can give attention to providing a more efficient reconstruction method by applying different interpolation methods.

- **Construct 3D mosaic.** One of the advantages of the multiphoton microendoscope is that it produces images in depth of thick samples. In the context that the depth information is provided, constructing a 3D panorama from the images is useful to the clinician to see the image in depth. To that end, it broadens the research to register and mosaic images on irregular in 3D concept.

- **Metric to evaluate constructed mosaic.** In the local scope of this thesis, constructed mosaic is only objectively evaluated without a statistical evaluation by an appropriate metric. One can manually create a synthesized sequence of images with prior knowledge of the displacements and a reference mosaic and then evaluate the similarity between the estimated mosaic and the reference mosaic. Therefore, considering the metric used in evaluating the estimated mosaic is still an open topic. Future works may include providing an efficient metric to evaluate mosaic construction.

- **Applying deep learning.** As stated previously, the graph based technique is normally computationally expensive and time consuming. A good way to reduce computation cost is to apply deep learning networks to either estimate similarity measure of two images in a iterative optimization strategy or predict transformation. Further work may extend the registration with the Spectral Graph Wavelet constraint to optimize the similarity metric using deep learning.

- **Further evaluation.** With modifications of the weighting parameters and different computation of the graphs, additional practical experiments of the

registration method on regular and irregular grids can be performed on different types of medical images to further evaluate our strategy.

List of publications

This thesis is mainly based on the following publications:

1. **Nhung Pham**, David Helbert, Pascal Bourdon, Philippe Carré. "Spectral Graph Wavelet based Nonrigid Image Registration". *In: 2018 25th IEEE International Conference on Image Processing (ICIP)*. IEEE. 2018, pp. 3348-3352.

2. **Hong Nhung Pham** , David Helbert, Pascal Bourdon, Philippe Carré. "Image Registration for Biomedical Images on Irregular Grids". *In: CORESA 2018 (COmpression et REprésentation des Signaux Audiovisuels)*. Poitiers, France, Nov. 2018.

Bibliography

[1] Isaac Amidror. "Scattered data interpolation methods for electronic imaging systems: a survey". In: *Journal of electronic imaging* 11.2 (2002), pp. 157–177.

[2] A. Anis, A. Gadde, and A. Ortega. "Towards a sampling theorem for signals on arbitrary graphs". In: *2014 IEEE International Conference on Acoustics, Speech and Signal Processing (ICASSP)*. 2014, pp. 3864–3868. DOI: 10.1109/ICASSP.2014.6854325.

[3] John Ashburner. "A fast diffeomorphic image registration algorithm". In: *Neuroimage* 38.1 (2007), pp. 95–113.

[4] John Ashburner and Karl J Friston. "Nonlinear spatial normalization using basis functions". In: *Human brain mapping* 7.4 (1999), pp. 254–266.

[5] Brian B Avants et al. "A reproducible evaluation of ANTs similarity metric performance in brain image registration". In: *Neuroimage* 54.3 (2011), pp. 2033–2044.

[6] Brian B Avants et al. "Symmetric diffeomorphic image registration with cross-correlation: evaluating automated labeling of elderly and neurodegenerative brain". In: *Medical image analysis* 12.1 (2008), pp. 26–41.

[7] Brian B Avants et al. "The Insight ToolKit image registration framework". In: *Frontiers in neuroinformatics* 8 (2014), p. 44.

[8] Antoine Azar et al. "An interactive hybrid non-rigid registration framework for 3D medical images". In: *Biomedical Imaging: Nano to Macro, 2006. 3rd IEEE International Symposium on*. IEEE. 2006, pp. 824–827.

[9] Ruzena Bajcsy and Stane Kovačič. "Multiresolution elastic matching". In: *Computer vision, graphics, and image processing* 46.1 (1989), pp. 1–21.

[10] Herbert Bay et al. "Speeded-up robust features (SURF)". In: *Computer vision and image understanding* 110.3 (2008), pp. 346–359.

[11] Rikard Berthilsson. "Affine correlation". In: *Pattern Recognition, 1998. Proceedings. Fourteenth International Conference on*. Vol. 2. IEEE. 1998, pp. 1458–1460.

[12] Fred L. Bookstein. "Principal warps: Thin-plate splines and the decomposition of deformations". In: *IEEE Transactions on pattern analysis and machine intelligence* 11.6 (1989), pp. 567–585.

[13] Jean-Yves Bouguet. "Pyramidal implementation of the affine lucas kanade feature tracker description of the algorithm". In: *Intel Corporation* 5.1-10 (2001), p. 4.

[14] Pascal Cachier et al. "Iconic feature based nonrigid registration: the PASHA algorithm". In: *Computer vision and image understanding* 89.2-3 (2003), pp. 272–298.

[15] Nathan D Cahill, J Alison Noble, and David J Hawkes. "A demons algorithm for image registration with locally adaptive regularization". In: *International Conference on Medical Image Computing and Computer-Assisted Intervention*. Springer. 2009, pp. 574–581.

[16] Oscar Camara et al. "Explicit incorporation of prior anatomical information into a nonrigid registration of thoracic and abdominal CT and 18-FDG whole-body emission PET images". In: *IEEE transactions on medical imaging* 26.2 (2007), pp. 164–178.

[17] Siheng Chen et al. "Discrete Signal Processing on Graphs: Sampling Theory". In: *CoRR* abs/1503.05432 (2015). URL: `http://arxiv.org/abs/1503.05432`.

[18] Siheng Chen et al. "Signal denoising on graphs via graph filtering". In: *Signal and Information Processing (GlobalSIP), 2014 IEEE Global Conference on*. IEEE. 2014, pp. 872–876.

[19] Siheng Chen et al. "Signal Recovery on Graphs: Random versus Experimentally Designed Sampling". In: *CoRR* abs/1504.05427 (2015). URL: `http://arxiv.org/abs/1504.05427`.

[20] Ming-Chang Chiang et al. "Fluid registration of diffusion tensor images using information theory". In: *IEEE transactions on medical imaging* 27.4 (2008), pp. 442–456.

[21] Se Young Chun and Jeffrey A Fessler. "A simple regularizer for B-spline non-rigid image registration that encourages local invertibility". In: *IEEE Journal of selected topics in Signal Processing* 3.1 (2009), pp. 159–169.

[22] Fan RK Chung. *Spectral graph theory*. 92. American Mathematical Soc., 1997.

[23] Amalia Cifor et al. "Hybrid feature-based diffeomorphic registration for tumor tracking in 2-d liver ultrasound images". In: *IEEE Trans. Med. Imaging* 32.9 (2013), pp. 1647–1656.

[24] André Collignon et al. "3D multi-modality medical image registration using feature space clustering". In: *Computer Vision, Virtual Reality and Robotics in Medicine*. Springer. 1995, pp. 195–204.

[25] André Collignon et al. "Automated multi-modality image registration based on information theory". In: *Information processing in medical imaging*. Vol. 3. 6. 1995, pp. 263–274.

[26] Mark Crovella and Eric Kolaczyk. "Graph wavelets for spatial traffic analysis". In: *INFOCOM 2003. Twenty-Second Annual Joint Conference of the IEEE Computer and Communications. IEEE Societies*. Vol. 3. IEEE. 2003, pp. 1848–1857.

[27] WR Crum, C Tanner, and DJ Hawkes. "Anisotropic multi-scale fluid registration: evaluation in magnetic resonance breast imaging". In: *Physics in Medicine & Biology* 50.21 (2005), p. 5153.

[28] Emiliano D'agostino et al. "A viscous fluid model for multimodal non-rigid image registration using mutual information". In: *Medical image analysis* 7.4 (2003), pp. 565–575.

[29] Radhakrishna Dasari and Chang Wen Chen. "A joint visual-inertial image registration for mobile HDR imaging". In: *Visual Communications and Image Processing (VCIP), 2016*. IEEE. 2016, pp. 1–4.

[30] Guillaume Ducourthial. "Développement d'un endomicroscope multiphotonique compact et flexible pour l'imagerie in vivo haute résolution de tissus biologiques non marqués". PhD thesis. Limoges, 2014.

[31] Guillaume Ducourthial et al. "Development of a real-time flexible multiphoton microendoscope for label-free imaging in a live animal". In: *Scientific reports* 5 (2015), p. 18303.

[32] Petra A van den Elsen. "Retrospective fusion of CT and MR brain images using mathematical operators". In: *AAAI symposium on medical applications of computer vision*. 1994, pp. 30–33.

[33] Koen AJ Eppenhof et al. "Deformable image registration using convolutional neural networks". In: *Medical Imaging 2018: Image Processing*. Vol. 10574. International Society for Optics and Photonics. 2018, 105740S.

[34] Khuram Faraz. "Skin image mosaicing with topological inference and global adjustment". PhD thesis. Université de Lorraine, 2017.

[35] Pedro F Felzenszwalb and Daniel P Huttenlocher. "Efficient graph-based image segmentation". In: *International journal of computer vision* 59.2 (2004), pp. 167–181.

[36] Bernd Fischer and Jan Modersitzki. "Fast diffusion registration". In: *Contemporary Mathematics* 313 (2002), pp. 117–128.

[37] Pasquale Foggia, Gennaro Percannella, and Mario Vento. "Graph matching and learning in pattern recognition in the last 10 years". In: *International Journal of Pattern Recognition and Artificial Intelligence* 28.01 (2014), p. 1450001.

[38] Leila MG Fonseca and Max HM Costa. "Automatic registration of satellite images". In: *Computer Graphics and Image Processing, 1997. Proceedings., X Brazilian Symposium on*. IEEE. 1997, pp. 219–226.

[39] Leila MG Fonseca and BS Manjunath. "Registration techniques for multisensor remotely sensed imagery". In: *PE & RS- Photogrammetric Engineering & Remote Sensing* 62.9 (1996), pp. 1049–1056.

[40] Mohamed M Fouad, Richard M Dansereau, and Anthony D Whitehead. "Image Registration Under Illumination Variations Using Region-Based Confidence Weighted M-Estimators". In: *IEEE transactions on image processing* 21.3 (2012), pp. 1046–1060.

[41] Karl J Friston et al. "Spatial registration and normalization of images". In: *Human brain mapping* 3.3 (1995), pp. 165–189.

[42] Smadar Gefen, Oleh Tretiak, and Jonathan Nissanov. "Elastic 3-D alignment of rat brain histological images". In: *IEEE transactions on medical imaging* 22.11 (2003), pp. 1480–1489.

[43] M Ghanbari. "The cross-search algorithm for motion estimation (image coding)". In: *IEEE Transactions on Communications* 38.7 (1990), pp. 950–953.

[44] R Gilmore. "Baker-Campbell-Hausdorff formulas". In: *Journal of Mathematical Physics* 15.12 (1974), pp. 2090–2092.

[45] B. Girault, P. Gonçalves, and É Fleury. "Translation on Graphs: An Isometric Shift Operator". In: *IEEE Signal Processing Letters* 22.12 (2015), pp. 2416–2420. ISSN: 1070-9908. DOI: 10.1109/LSP.2015.2488279.

[46] Ardeshir Goshtasby, George C Stockman, and Carl V Page. "A region-based approach to digital image registration with subpixel accuracy". In: *IEEE Transactions on Geoscience and Remote Sensing* 3 (1986), pp. 390–399.

[47] Mehdi Hadj-Hamou et al. "Longitudinal analysis of image time series with diffeomorphic deformations: a computational framework based on stationary velocity fields". In: *Frontiers in neuroscience* 10 (2016), p. 236.

[48] David K Hammond, Pierre Vandergheynst, and Rémi Gribonval. "Wavelets on graphs via spectral graph theory". In: *Applied and Computational Harmonic Analysis* 30.2 (2011), pp. 129–150.

[49] Chris Harris and Mike Stephens. "A combined corner and edge detector." In: *Alvey vision conference*. Vol. 15. 50. Citeseer. 1988, pp. 10–5244.

[50] M Helm. "Towards automatic rectification of satellite images using feature based matching". In: *Geoscience and Remote Sensing Symposium, 1991. IGARSS'91. Remote Sensing: Global Monitoring for Earth Management., International*. Vol. 4. IEEE. 1991, pp. 2439–2442.

[51] Fritjof Helmchen and Winfried Denk. "Deep tissue two-photon microscopy". In: *Nature methods* 2.12 (2005), p. 932.

[52] Nicholas J Higham. "The scaling and squaring method for the matrix exponential revisited". In: *SIAM review* 51.4 (2009), pp. 747–764.

[53] Gang Hong and Yun Zhang. "Wavelet-based image registration technique for high-resolution remote sensing images". In: *Computers & Geosciences* 34.12 (2008), pp. 1708–1720.

[54] Nicolas Honnorat, Régis Vaillant, and Nikos Paragios. "Graph-based geometric-iconic guide-wire tracking". In: *International Conference on Medical Image Computing and Computer-Assisted Intervention*. Springer. 2011, pp. 9–16.

[55] Nicolas Honnorat et al. "GraSP: geodesic graph-based segmentation with shape priors for the functional parcellation of the cortex". In: *Neuroimage* 106 (2015), pp. 207–221.

[56] Berthold KP Horn and Brian G Schunck. "Determining optical flow". In: *Artificial intelligence* 17.1-3 (1981), pp. 185–203.

[57] Yuan C Hsieh, David M McKeown Jr, and Frederic P Perlant. "Performance evaluation of scene registration and stereo matching for artographic feature extraction". In: *IEEE Transactions on Pattern Analysis and Machine Intelligence* 14.2 (1992), pp. 214–238.

[58] Wei-Yen Hsu. "A hybrid approach for brain image registration with local constraints". In: *Integrated Computer-Aided Engineering* 24.1 (2017), pp. 73–85.

[59] M Hub, ML Kessler, and CP Karger. "B-spline registration versus demons algorithm-a quantitative comparison of accuracy and invertibility based on artificially created test cases for the lung". In: *World Congress on Medical Physics and Biomedical Engineering, September 7-12, 2009, Munich, Germany*. Springer. 2009, pp. 790–792.

[60] Michal Irani, P Anandan, and Steve Hsu. "Mosaic based representations of video sequences and their applications". In: *Computer Vision, 1995. Proceedings., Fifth International Conference on*. IEEE. 1995, pp. 605–611.

[61] H Martin Kjer et al. "Free-form image registration of human cochlear μCT data using skeleton similarity as anatomical prior". In: *Pattern Recognition Letters* 76 (2016), pp. 76–82.

[62] Yanir Kleiman and Maks Ovsjanikov. "Robust Structure-Based Shape Correspondence". In: *Computer Graphics Forum*. Wiley Online Library. 2018.

[63] Stefan Klein, Marius Staring, and Josien PW Pluim. "Evaluation of optimization methods for nonrigid medical image registration using mutual information and B-splines". In: *IEEE transactions on image processing* 16.12 (2007), pp. 2879–2890.

[64] Jan Kybic and Michael Unser. "Fast parametric elastic image registration". In: (2003).

[65] Olivier Lézoray and Leo Grady. *Image processing and analysis with graphs: theory and practice*. CRC Press, 2012.

[66] Hui Li, BS Manjunath, and Sanjit K Mitra. "A contour-based approach to multisensor image registration". In: *IEEE transactions on image processing* 4.3 (1995), pp. 320–334.

[67] Jing Li, Xuan Yang, and Jianping Yu. "Compact support thin plate spline algorithm". In: *Journal of Electronics (China)* 24.4 (2007), pp. 515–522.

[68] Stan Z Li, Josef Kittler, and Maria Petrou. "Matching and recognition of road networks from aerial images". In: *European Conference on Computer Vision*. Springer. 1992, pp. 857–861.

[69] Xiangbo Lin et al. "A topology preserving non-rigid registration algorithm with integration shape knowledge to segment brain subcortical structures from MRI images". In: *Pattern Recognition* 43.7 (2010), pp. 2418–2427.

[70] Herve Lombaert et al. "Spectral Demons–image registration via global spectral correspondence". In: *Computer Vision–ECCV 2012*. Springer, 2012, pp. 30–44.

[71] Herve Lombaert et al. "Spectral log-demons: diffeomorphic image registration with very large deformations". In: *International journal of computer vision* 107.3 (2014), pp. 254–271.

[72] Nick Lord. "Lie groups and Lie algebras (chapters 1-3), by N. Bourbaki. Pp 450. DM 98. 1989. ISBN 3-540-50218-1 (Springer)". In: *The Mathematical Gazette* 74.468 (1990), pp. 199–201.

[73] Marco Lorenzi et al. "LCC-Demons: a robust and accurate symmetric diffeomorphic registration algorithm". In: *NeuroImage* 81 (2013), pp. 470–483.

[74] David G Lowe. "Distinctive image features from scale-invariant keypoints". In: *International journal of computer vision* 60.2 (2004), pp. 91–110.

[75] Huanxiang Lu, Philippe C Cattin, and Mauricio Reyes. "A hybrid multimodal non-rigid registration of MR images based on diffeomorphic demons". In: *Engineering in medicine and biology society (EMBC), 2010 annual international conference of the IEEE*. IEEE. 2010, pp. 5951–5954.

[76] Huanxiang Lu et al. "Multi-modal diffeomorphic demons registration based on point-wise mutual information". In: *Biomedical Imaging: From Nano to Macro, 2010 IEEE International Symposium on*. IEEE. 2010, pp. 372–375.

[77] Bruce D Lucas, Takeo Kanade, et al. "An iterative image registration technique with an application to stereo vision." In: *IJCAI*. Vol. 81. 1. 1981, pp. 674–679.

[78] Inês Machado et al. "Non-rigid registration of 3D ultrasound for neurosurgery using automatic feature detection and matching". In: *International journal of computer assisted radiology and surgery* (2018), pp. 1–14.

[79] Frederik Maes et al. "Multimodality image registration by maximization of mutual information". In: *IEEE transactions on Medical Imaging* 16.2 (1997), pp. 187–198.

[80] Mohamed Malek, David Helbert, and Philippe Carré. "Color graph based wavelet transform with perceptual information". In: *Journal of Electronic Imaging* 24.5 (2015), p. 053004.

[81] Tommaso Mansi et al. "iLogDemons: A demons-based registration algorithm for tracking incompressible elastic biological tissues". In: *International journal of computer vision* 92.1 (2011), pp. 92–111.

[82] Waleed Mohamed and A Ben Hamza. "Deformable 3d shape retrieval using a spectral geometric descriptor". In: *Applied Intelligence* 45.2 (2016), pp. 213–229.

[83] S. K. Narang, G. Shen, and A. Ortega. "Unidirectional graph-based wavelet transforms for efficient data gathering in sensor networks". In: *2010 IEEE International Conference on Acoustics, Speech and Signal Processing*. 2010, pp. 2902–2905. DOI: 10.1109/ICASSP.2010.5496172.

[84] Jorge Nocedal. "Updating quasi-Newton matrices with limited storage". In: *Mathematics of computation* 35.151 (1980), pp. 773–782.

[85] Francisco PM Oliveira and Joao Manuel RS Tavares. "Medical image registration: a review". In: *Computer methods in biomechanics and biomedical engineering* 17.2 (2014), pp. 73–93.

[86] Danielle F Pace, Stephen R Aylward, and Marc Niethammer. "A locally adaptive regularization based on anisotropic diffusion for deformable image registration of sliding organs". In: *IEEE transactions on medical imaging* 32.11 (2013), pp. 2114–2126.

[87] Dana Paquin, Doron Levy, and Lei Xing. *Hybrid multiscale landmark and deformable image registration*. Tech. rep. STANFORD UNIV CA DEPT OF MATHEMATICS, 2007.

[88] Christopher Paulson, Soundararajan Ezekiel, and Dapeng Wu. "Wavelet-based image registration". In: *Evolutionary and Bio-Inspired Computation: Theory and Applications IV*. Vol. 7704. International Society for Optics and Photonics. 2010, p. 77040M.

[89] Xavier Pennec, Pascal Cachier, and Nicholas Ayache. "Understanding the "demon's algorithm": 3D non-rigid registration by gradient descent". In: *International Conference on Medical Image Computing and Computer-Assisted Intervention*. Springer. 1999, pp. 597–605.

[90] I. Pesenson. "Sampling in paley-wiener spaces on combinatorial graphs". In: *ArXiv e-prints* (Nov. 2011). arXiv: `1111.5896 [math.SP]`.

[91] Hong Nhung Pham et al. "Image Registration for Biomedical Images on Irregular Grids". In: *CORESA 2018 (COmpression et REprésentation des Signaux Audiovisuels*. Poitiers, France, Nov. 2018. URL: `https://hal.archives-ouvertes.fr/hal-01897326`.

[92] Nhung Pham et al. "Spectral Graph Wavelet based Nonrigid Image Registration". In: *2018 25th IEEE International Conference on Image Processing (ICIP)*. IEEE. 2018, pp. 3348–3352.

[93] Karl Rohr et al. "Landmark-based elastic registration using approximating thin-plate splines". In: *IEEE Transactions on medical imaging* 20.6 (2001), pp. 526–534.

[94] Karl Rohr et al. "Point-based elastic registration of medical image data using approximating thin-plate splines". In: *Visualization in Biomedical Computing*. Springer. 1996, pp. 297–306.

[95] Daniel Rueckert and P Aljabar. "Non-rigid registration using free-form deformations". In: *Handbook of Biomedical Imaging*. Springer, 2015, pp. 277–294.

[96] Daniel Rueckert et al. "Nonrigid registration using free-form deformations: application to breast MR images". In: *IEEE transactions on medical imaging* 18.8 (1999), pp. 712–721.

[97] Akie Sakiyama and Yuichi Tanaka. "Oversampled Graph Laplacian Matrix for Graph Filter Banks". In: *IEEE Trans. Signal Processing* 62.24 (2014), pp. 6425–6437. DOI: 10.1109/TSP.2014.2365761. URL: http://dx.doi.org/10.1109/TSP.2014.2365761.

[98] Aliaksei Sandryhaila and José M. F. Moura. "Discrete Signal Processing on Graphs". In: *CoRR* abs/1210.4752 (2012). URL: http://arxiv.org/abs/1210.4752.

[99] Aliaksei Sandryhaila and José M. F. Moura. "Discrete Signal Processing on Graphs: Frequency Analysis". In: *CoRR* abs/1307.0468 (2013). URL: http://arxiv.org/abs/1307.0468.

[100] Guy L Scott and Hugh Christopher Longuet-Higgins. "An algorithm for associating the features of two images". In: *Proc. R. Soc. Lond. B* 244.1309 (1991), pp. 21–26.

[101] Thomas W Sederberg and Scott R Parry. "Free-form deformation of solid geometric models". In: *ACM SIGGRAPH computer graphics* 20.4 (1986), pp. 151–160.

[102] Monika Sester, Heiner Hild, and Dieter Fritsch. "Definition of ground-control features for image registration using GIS data". In: *International Archives of Photogrammetry and Remote Sensing* 32 (1998), pp. 538–543.

[103] Dinggang Shen and Christos Davatzikos. "HAMMER: hierarchical attribute matching mechanism for elastic registration". In: *IEEE transactions on medical imaging* 21.11 (2002), pp. 1421–1439.

[104] Dinggang Shen and Christos Davatzikos. "Very high-resolution morphometry using mass-preserving deformations and HAMMER elastic registration". In: *NeuroImage* 18.1 (2003), pp. 28–41.

[105] David I. Shuman et al. "Signal Processing on Graphs: Extending High-Dimensional Data Analysis to Networks and Other Irregular Data Domains". In: *CoRR* abs/1211.0053 (2012). URL: http://arxiv.org/abs/1211.0053.

[106] Viviana Siless et al. "Joint T1 and brain fiber log-demons registration using currents to model geometry". In: *International Conference on Medical Image Computing and Computer-Assisted Intervention*. Springer. 2012, pp. 57–65.

[107] Andrew Simper. "Correcting general band-to-band misregistrations". In: *Image Processing, 1996. Proceedings., International Conference on*. Vol. 2. IEEE. 1996, pp. 597–600.

[108] Aristeidis Sotiras. "Discrete image registration: a hybrid paradigm". PhD thesis. Ecole Centrale Paris, 2011.

[109] Aristeidis Sotiras et al. "Graph-based deformable image registration". In: *Handbook of Biomedical Imaging*. Springer, 2015, pp. 331–359.

[110] Colin Studholme, Derek LG Hill, and David J Hawkes. "Multiresolution voxel similarity measures for MR-PET registration". In: *Information processing in medical imaging*. Vol. 3. Dordrecht, The Netherlands: Kluwer. 1995, pp. 287–298.

[111] Richard Szeliski and James Coughlan. "Spline-based image registration". In: *International Journal of Computer Vision* 22.3 (1997), pp. 199–218.

[112] Demetri Terzopoulos, Andrew P Witkin, and Michael Kass. "Energy Constraints on Deformable Models: Recovering Shape and Non-Rigid Motion." In: *AAAI*. 1987, pp. 755–760.

[113] Philippe Thévenaz and Michael Unser. "Optimization of mutual information for multiresolution image registration". In: *IEEE transactions on image processing* 9.12 (2000), pp. 2083–2099.

[114] J-P Thirion. "Image matching as a diffusion process: an analogy with Maxwell's demons". In: *Medical image analysis* 2.3 (1998), pp. 243–260.

[115] Carlo Tomasi and Takeo Kanade. "Detection and tracking of point features". In: (1991).

[116] Jyi-Chang Tsai et al. "Block-matching motion estimation using correlation search algorithm". In: *Signal Processing: Image Communication* 13.2 (1998), pp. 119–133.

[117] Shinji Umeyama. "An eigendecomposition approach to weighted graph matching problems". In: *IEEE transactions on pattern analysis and machine intelligence* 10.5 (1988), pp. 695–703.

[118] Petra A Van Den Elsen et al. "Grey value correlation techniques used for automatic matching of CT and MR brain and spine images". In: *Visualization in Biomedical Computing 1994*. Vol. 2359. International Society for Optics and Photonics. 1994, pp. 227–238.

[119] Tom Vercauteren et al. "Diffeomorphic demons: Efficient non-parametric image registration". In: *NeuroImage* 45.1 (2009), S61–S72.

[120] Tom Vercauteren et al. "Insight into efficient image registration techniques and the demons algorithm". In: *Biennial International Conference on Information Processing in Medical Imaging*. Springer. 2007, pp. 495–506.

[121] Tom Vercauteren et al. "Non-parametric diffeomorphic image registration with the demons algorithm". In: *International Conference on Medical Image Computing and Computer-Assisted Intervention*. Springer. 2007, pp. 319–326.

[122] Tom Vercauteren et al. "Symmetric log-domain diffeomorphic registration: A demons-based approach". In: *Medical Image Computing and Computer-Assisted Intervention–MICCAI 2008* (2008), pp. 754–761.

[123] Paul Viola and William M Wells III. "Alignment by maximization of mutual information". In: *International journal of computer vision* 24.2 (1997), pp. 137–154.

[124] Nenad Vujovic and Dragana Brzakovic. "Establishing the correspondence between control points in pairs of mammographic images". In: *IEEE Transactions on Image Processing* 6.10 (1997), pp. 1388–1399.

[125] He Wang et al. "Validation of an accelerated 'demons' algorithm for deformable image registration in radiation therapy". In: *Physics in Medicine & Biology* 50.12 (2005), p. 2887.

[126] Jianzhe Wang and Tianzi Jiang. "Nonrigid registration of brain MRI using NURBS". In: *Pattern Recognition Letters* 28.2 (2007), pp. 214–223.

[127] MA Warren et al. "Estimation of ocean surface currents from maximum cross correlation applied to GOCI geostationary satellite remote sensing data over the Tsushima (Korea) Straits". In: *Journal of Geophysical Research: Oceans* 121.9 (2016), pp. 6993–7009.

[128] George Wolberg and Siavash Zokai. "Image registration for perspective deformation recovery". In: *Automatic Target Recognition X*. Vol. 4050. International Society for Optics and Photonics. 2000, pp. 259–271.

[129] George Wolberg and Siavash Zokai. "Robust image registration using log-polar transform". In: *Image Processing, 2000. Proceedings. 2000 International Conference on*. Vol. 1. IEEE. 2000, pp. 493–496.

[130] Philip Wolfe. "Convergence conditions for ascent methods". In: *SIAM review* 11.2 (1969), pp. 226–235.

[131] Roger P Woods et al. "Automated image registration: I. General methods and intrasubject, intramodality validation". In: *Journal of computer assisted tomography* 22.1 (1998), pp. 139–152.

[132] Medha V Wyawahare, Pradeep M Patil, Hemant K Abhyankar, et al. "Image registration techniques: an overview". In: *International Journal of Signal Processing, Image Processing and Pattern Recognition* 2.3 (2009), pp. 11–28.

[133] Zhen Xiong and Yun Zhang. "A critical review of image registration methods". In: *International Journal of Image and Data Fusion* 1.2 (2010), pp. 137–158.

[134] Huang Xishan and Chen Zhe. "A wavelet-based multisensor image registration algorithm". In: *Signal Processing, 2002 6th International Conference on*. Vol. 1. Ieee. 2002, pp. 773–776.

[135] BT Thomas Yeo et al. "Spherical demons: fast diffeomorphic landmark-free surface registration". In: *IEEE transactions on medical imaging* 29.3 (2010), pp. 650–668.

[136] Youbing Yin et al. "A cubic B-spline-based hybrid registration of lung CT images for a dynamic airway geometric model with large deformation". In: *Physics in Medicine & Biology* 56.1 (2010), p. 203.

[137] C. T. Zahn. "Graph-Theoretical Methods for Detecting and Describing Gestalt Clusters". In: *IEEE Transactions on Computers* C-20.1 (1971), pp. 68–86. ISSN: 0018-9340. DOI: 10.1109/T-C.1971.223083.

[138] Jianping Zhang and Ke Chen. "Variational image registration by a total fractional-order variation model". In: *Journal of Computational Physics* 293 (2015), pp. 442–461.

[139] Barbara Zitova and Jan Flusser. "Image registration methods: a survey". In: *Image and vision computing* 21.11 (2003), pp. 977–1000.